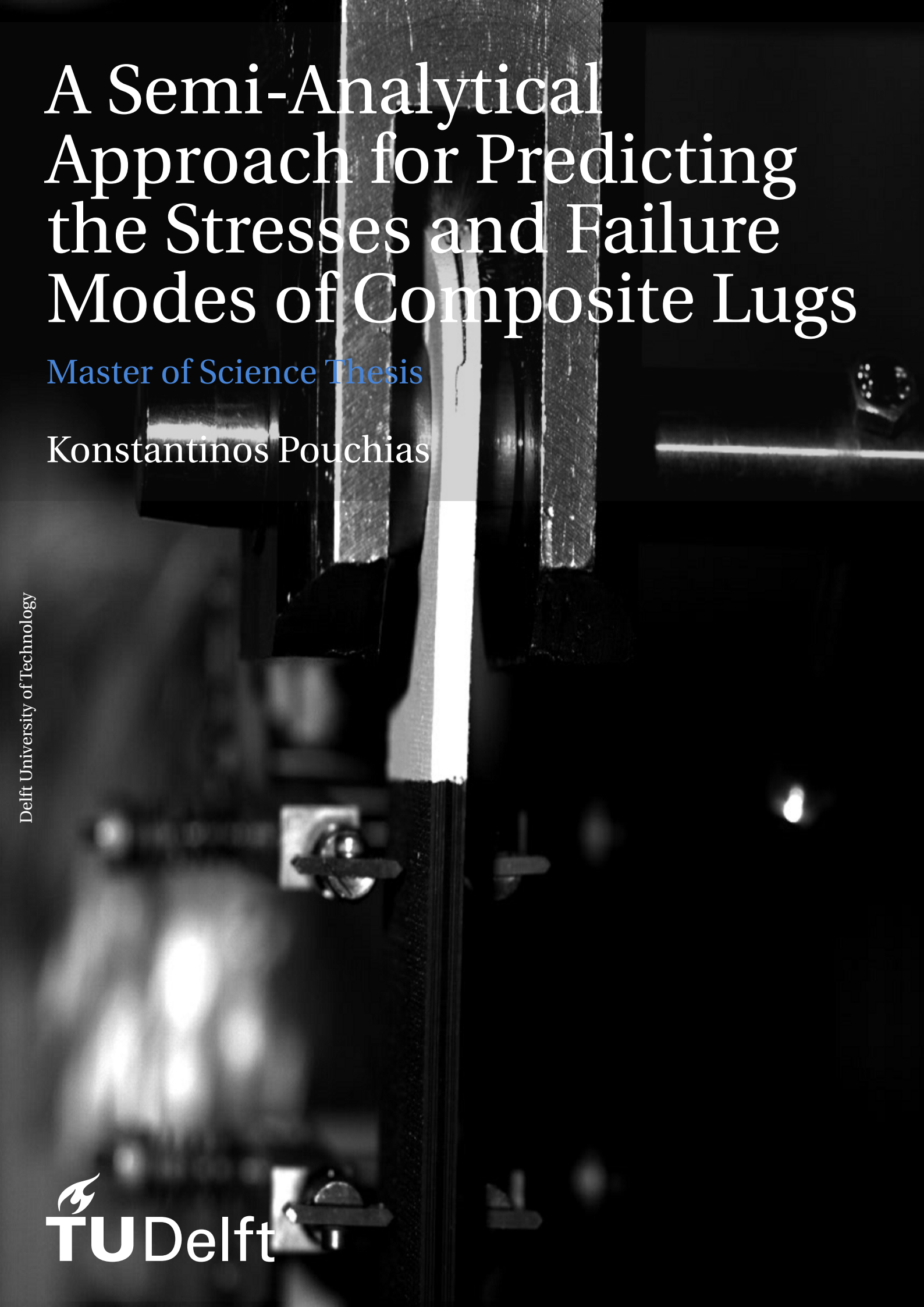

A Semi-Analytical Approach for Predicting the Stresses and Failure Modes of Composite Lugs

Master of Science Thesis

Konstantinos Pouchias

Delft University of Technology

TU Delft

A Semi-Analytical Approach for Predicting the Stresses and Failure Modes of Composite Lugs

Master of Science Thesis

by

Konstantinos Pouchias

to obtain the degree of Master of Science
at the Delft University of Technology,
to be defended publicly on Friday October 13, 2023 at 9:30 AM.

Student number:	5594812	
Project duration:	January 1, 2023 – October 13, 2023	
Thesis committee:	Prof. dr. ir. C. Kassapoglou,	TU Delft, Supervisor
	Dr. ing. S. G. P. Castro ,	TU Delft
	Dr. ir. J. A. Pascoe,	TU Delft

An electronic version of this thesis is available at http://repository.tudelft.nl/.

TU Delft

"In the middle of difficulty lies opportunity."
Albert Einstein

Preface

The completion of this thesis would not have been possible without the cooperation, help, and guidance of certain people, whose support has been invaluable. To begin with, I would like to express my gratitude to the professor in charge of the thesis, Dr.ir. Christos Kassapoglou for his trust in me and his persistence in pushing me beyond my boundaries to achieve the best result. I am grateful for the collaboration we had and all the knowledge and information he passed on to me.

Moreover, I would like to thank all the technicians and research personnel who provided me with assistance and information throughout the experimental and modeling phase of the thesis. Their support and willingness were invaluable. In addition, I would like to express my gratitude to all the individuals who have played a role, however small, in the completion of this thesis. Each interaction, conversation, and exchange of ideas has contributed to my personal growth and aided me in overcoming obstacles in my research topic.

Finally, the last and biggest thank you, I owe it to my family and friends for their support, encouragement, and understanding throughout my academic journey. Their love and patience were the pillars of my strength.

Abstract

Lugs are a specific type of joint with a semi-circular geometry around the pinhole utilized in the aerospace field. Its distinct geometry and ability to carry loads in its plane make it a very common choice for design engineers. Although this type of joint is widely used, there are no analytical equations that can predict the stresses around the hole. This research topic presents a semi-analytical approach to predict the in-plane stresses and failure modes of a composite lug under tensile pin loading. The methodology developed is based on stress functions for anisotropic beams implemented in stress equations for solid bodies in a polar coordinate system. The results of this approach are validated with the use of numerical simulation models, whose trustworthiness is verified by tensile tests. The outcome of this thesis is in-plane stress distribution graphs for every layer of the laminate around the hole and the in-plane failure mode of the lug. The results show a good accordance between the stresses predicted from the semi-analytical approach and the numerical simulations. Moreover, two lug designs with different geometric characteristics were tested in order to observe the influence of the geometry on the failure load. It was concluded that the geometry affects the maximum failure load but not the stress distribution, which is concurrent with the literature. Overall, the methodology presented in this research topic provided promising results. The findings of this thesis can have a great impact and aid engineers in estimating the stresses in a composite lug from the preliminary phase of a project.

Contents

List of Figures

List of Tables

CHAPTER 1

Introduction

An aircraft is an intricate structure comprised of numerous components and subsystems. Every part of the assembly is designed with meticulous precision in order to guarantee optimal performance, structural integrity, and safety of the passengers. While every aircraft component is carefully designed, equal attention is placed on the methods and techniques applied for connecting these parts. As an aircraft operates under demanding operational and environmental conditions, the reliability and trustworthiness of the joining methods play a crucial role in ensuring the aircraft's durability and overall performance.

The connection of different components of an aircraft is achieved with the use of joints. Joints are a very crucial part of the aircraft and they play a significant role in connecting structural components while withstanding primary and secondary loads. There are four types of joints, namely: mechanically fastened, adhesively bonded, welded, and a combination of these categories. While adhesively bonded and welded joints are recognized for their ability to effectively distribute applied loads, they are not versatile because the joined parts cannot get separated after bonding (exceptions apply e.g., in thermoplastic welded joints which can be re-welded after applying the appropriate heating treatment). However, mechanically fastened joints (Figure 1.1) are widely adopted due to the freedom and flexibility they offer in assembling parts [1].

(a) Geometry of a generic joint.

(b) Geometry of a lug.

Figure 1.1: Typical geometries of mechanically fastened joints.

One of the most commonly used joint in the aerospace field is lugs. A lug (Figure 1.1b) is a mechanically fastened joint with a distinct geometry that can withstand significant loads within its plane.

The ability of this joint to bear high loads is the reason why it can be found on the primary and secondary structures of the aircraft. In the last few years, the aerospace field, driven by the need to develop lighter and more sustainable aircrafts, shifted its focus to utilizing composite materials in many components. The characteristic advantages over metals, including their resistance to corrosion and high strength-to-weight ratios, provided designers with more options with greater flexibility for the optimization of the aircraft structure [2]. Consequently, composite materials started substituting metal alloys in the manufacturing of joints (including lugs) in the aerospace industry. The distinct semi-circular geometry of the lug, along with the non-linearity of the material, made the analytical prediction of the stresses in a composite lug extremely challenging.

1.1 Purpose of the thesis

The main research objective of this thesis project is to develop analytical equations that can predict the stresses in a lug made of composite materials under tensile loads. The results of this method will be validated with the Finite Element Method (FEM). Moreover, an attempt will be made to predict the failure mode of the lug. The outcome will be verified with experimental data obtained from tensile tests that will be conducted. The results of this master thesis project will aid engineers in having a rough estimate of the optimal design and lay-up of a composite lug even from the preliminary designing phase.

1.2 Structure of the report

This report is structured in eight main chapters including the introduction. Chapter 2 will elaborate on the literature review conducted to gather information on the research about composite joints. The method for obtaining the analytical expressions for calculating the stresses in the lug will be presented in Chapter 3, while Chapter 4 will include all the information about the numerical simulations. Additionally, Chapter 5 will explain the experimental set-up and Chapter 6 will discuss the in-plane failure modes of the lug. Finally, the report will conclude with future recommendations and conclusions.

CHAPTER 2

Literature Review

This chapter aims to describe the relevant research articles, academic papers, and other credible sources that contribute to understanding the research topic of this thesis. The main research areas that have received primary emphasis in this project are the strength calculation in metal joints, failure modes in mechanically fastened composite joints, and stress prediction around holes in composite plates. In addition, a detailed overview of the current methods for analytical stress prediction around holes in composite joints is going to be described, along with methods that predict the stresses with the use of numerical models.

2.1 Strength calculation in metal joints

The prediction of stresses in a body was always considered a challenge in the engineering field. Timoshenko and Goodier [3] described accurately the theory of elasticity, which proved to be very useful in understanding and tackling various engineering tasks. In the book "Theory of Elasticity", the authors provide information and explanations on how to calculate the stresses and strains in solid bodies and in various coordinate systems. This book is considered the foundation of stress prediction and was later used by many authors to calculate the stresses in metal or composite joints.

One of the first that tried to predict the failure of metal joints and especially lugs was Cozzone et al. [4]. In the paper “Analysis of Lugs And Shear Pins Made of Aluminum Or Steel Alloys”, the authors described that the main failure modes of lug under tension are: net tension, shear out, and bearing failure. They concluded that lugs should be designed conservatively due to the fact that their importance is very high compared to their total weight. For this reason, an extra safety factor of 1.2 should be applied to the calculations. Moreover, they conducted numerous tensile tests to acquire stress concentration factors for many aluminum and steel alloys.

Regarding the mechanically fastened joints, Maddux [5] pointed out that the lug is the most commonly used joint with a pin connection. He concurred with the notion put forth by the preceding authors regarding the over-design of lugs, and with his research he tried to predict more accurately the failure strength of lugs. In his work, he described in detail how to perform a static strength analysis of a lug under tensile, shear, and oblique loads. Finally, he concluded with fatigue analysis on aluminum lugs under tension.

Based on the research conducted by the previously mentioned authors, Bruhn et al. [6] tried to specify the failure modes of the lugs with more accurate safety factors. In the book “Analysis and Design of Flight Vehicle Structures” in Chapter D1, the authors tried to point out the immense sig-

nificance of the joints in an aircraft structure. In an ideal scenario an aircraft would be made as a single structure, but the need for maintenance, and joining different geometries and materials made this idea impossible to achieve. Hence, the designing of a joint has crucial importance in the structural integrity and weight of the whole structure.

For determining the failure load, Bruhn et al. [6] utilized the equations already used by Cozzone et al. [4] and Maddux [5], but this time the authors applied more optimized safety factors, different for every mode of failure. In particular, for net tension failure, the failure load P_u is given by the following equation.

$$P_{u(tension)} = F_{tu} \cdot A_t$$

$$F_{tu} : \text{ultimate tensile material strength}$$
$$A_t : \text{net tension area} \tag{2.1.1}$$

In this case, a safety factor of 20% should be applied in order to account for the fact that in equation 2.1.1, the stress in the net tension area (Figure 2.1) is assumed uniform.

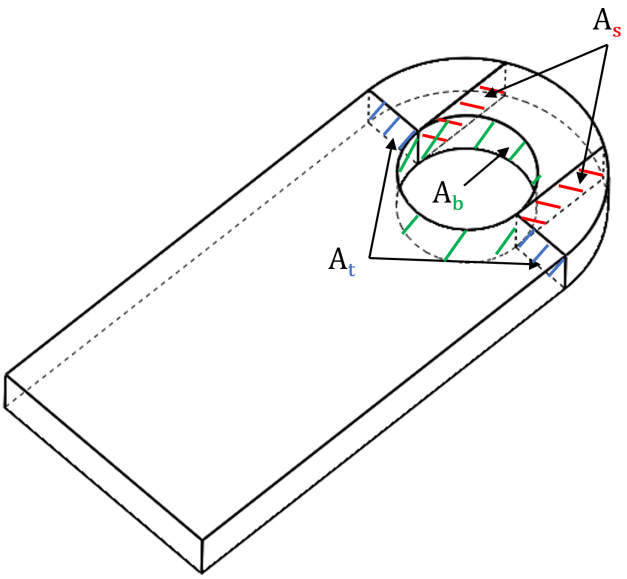

Figure 2.1: Areas of the failure modes in a lug.

Moreover, for shear-out failure, the failure load is given by the next equation.

$$P_{u(shear-out)} = F_{su} \cdot A_s$$

$$F_{su} : \text{ultimate shear material strength}$$
$$A_s : \text{shear out area} \tag{2.1.2}$$

Since the shear-out area (Figure 2.1) is larger than the area utilized in this equation, no safety factor is needed. Finally, the bearing failure load is specified by the following equation.

$$P_{u(bearing)} = F_{br} \cdot A_b$$

$$F_{br} : \text{allowable bearing stress}$$
$$A_b : \text{bearing area} \tag{2.1.3}$$

In this case, it is recommended to use a safety factor of 50%. In addition, the authors multiplied the derived failure loads with the stress concentration factors for net tension and shear-out acquired

by Cozzone et al. [4] to account for the hole in the geometry of the lug. Lastly, for the case of bearing they used the stress concentration factors of shear-out and calculated a shear-out/bearing failure load.

2.2 Failure modes in mechanically fastened composite joints

In recent years, the superior characteristics of composite materials such as corrosion resistance, and high stiffness-to-weight ratio, have contributed to the widespread substitution of metal components in aircrafts. Hence, the selection of composite materials for the designing and manufacturing of joints was inevitable. However, as pointed out by Waszczak and Cruse [7], composite joints started substituting metal joints at a low pace, due to the fact that composite joints have many types of failure that do not exist in metals and are difficult to predict. This statement is also substantiated by Camanho and Matthews [8] in the article "A Progressive Damage Model for Mechanically Fastened Joints in Composite Laminates", which described that the vast combination of matrices and fiber, lay-up stacking and orientations, complicates the stress and failure mode prediction in composite joints.

The failure modes of composite joints were described thoroughly by Chang [9], who identified three main failure modes, namely: shear-out, net tension, and bearing. The first two failure modes are associated with in-plane failure mechanisms such as fiber-breaking, shearing between matrix and fiber, and matrix cracking. In addition, the bearing failure mode is associated with three-dimensional failure mechanisms such as fiber buckling and matrix-fiber crushing.

Camanho and Matthews [10] managed to establish a relation between the modes of failure and the geometry of a composite joint. Specifically, they identified that bearing failure occurs in joints where the ratio between the hole diameter and the width of the joint (D/w) is small. The result of this mode of failure is the elongation of the hole. Furthermore, the shear-out failure mode is categorized as a special category of bearing failure and occurs in joints where the edge of the joint is at a large distance from the hole. In addition, net tension failure happens when the ratio between the hole diameter and the width of the joint is large. It is important to mention, that the authors identified two more failure modes, namely pull-through and cleavage as can be observed in Figure 2.2. They concluded that, regardless of the geometry of a joint, the lay-up orientation and the material properties have a significant role in the strength of the joint and the type of failure.

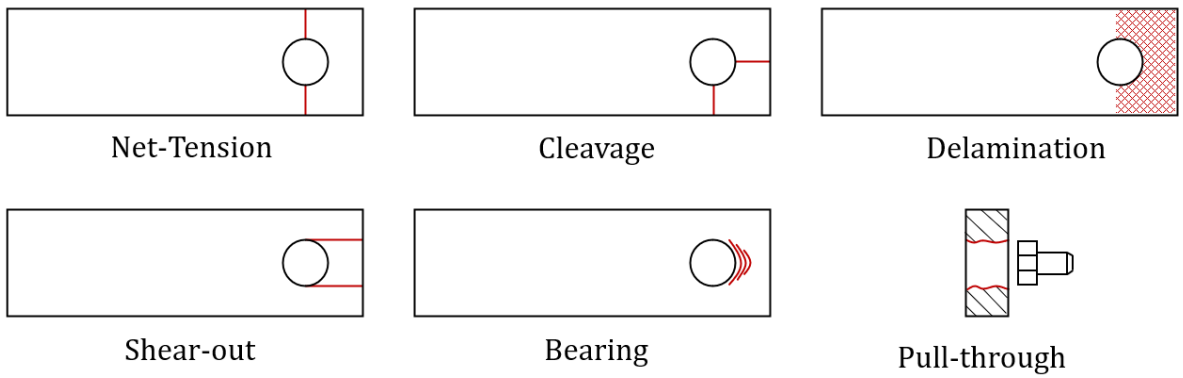

Figure 2.2: Failure modes in composite joints.

Another failure mode that plays a significant role in the strength of composite joints, is delaminations. This failure mode initiates between dissimilar adjacent layers due to differences in the elastic material properties [11]. Pipes and Pagano [12] developed a solution to describe the elastic

behavior of a symmetric-angle ply laminate. They concluded that interlaminar shear (τ_{xz}, τ_{yz}) and normal (σ_z) stresses are the main cause for delaminations. These stresses are developed near the edges (free-edge effect) of the laminate and eventually decay at a fast pace as the distance from the free-edge increases.

The free edge effect was also described by Noor and Burton [13] who specified that delaminations can be also found in areas with high-stress concentrations such as geometrical discontinuities (e.g., cut-outs, corners, holes) or near laminate edges between layers with different engineering properties. The laminate's strength in the out-of-plane direction relies on its matrix properties. Given the relatively lower strength of the laminate in this direction, interlaminar stresses aid in the initiation of delaminations, resulting in premature failure of the laminate.

It is evident, that delaminations may lead to hazardous consequences in the case of joints. Except for out-of-plane loading of a joint, delaminations can occur during in-plane loading conditions. Lucking et al. [14] studied the effect of geometry on interlaminar stresses in a cross-ply [0/90] laminate under tension. The research concluded that, as the ratio between the hole radius over the thickness of the laminate (R/t) increases, the interlaminar shear stresses at the edge of the hole increase between the different layers. Moreover, the authors noticed that while the term R/t increases, the normal shear stress on the middle plane near the hole also increases and shifts its position towards the edge where other stresses have also a high value.

Since delaminations is a significant mode that can cause premature failure of a structure, it is of utmost importance to predict when it is going to start. For this reason, Brewer and Lagace [15] developed an onset of delamination criterion appropriate for interlaminar stresses developed at the free edges of a laminate. There are also criteria to predict the out-of-plane failure load of a laminate such as the one proposed by Chang and Springer [16]:

$$\left(\frac{\sigma_r}{Z_r}\right)^2 + \left(\frac{\tau_{r\theta}}{Z_{r\theta}}\right)^2 = d^2 \tag{2.2.1}$$

$$d^2 < 1: \text{ no failure}, \; d^2 \geq 1: \text{ failure}$$
$$Z_r : \text{out-of-plane strength in r direction}$$
$$Z_{r\theta} : \text{transverse shear strength in plane } r\theta$$

In conclusion, every mode of failure (either in-plane or out-of-plane) should be accounted for when designing a composite joint. In an optimal joint, the failure loads of every failure mode should be in close proximity. Delaminations should also be carefully studied not only to predict their onset but also their effect on the laminate's strength after the first ply failure. This is very crucial because delaminations can be initiated as a result of another failure mode preceding them (e.g., net tension or shear-out failure can create free edges where interlaminar stresses can be developed) and affect the strength of the joint.

2.3 Stress around holes in composite plates

As pointed out by Whitney and Nuismer [17],[18] after acquiring a lot of experimental data on composite laminates with holes, the prediction of stresses in composite plates is not a simple process. Unlike metals where the maximum stress around a hole is predicted by utilizing a stress concentration factor, in composite laminates the stress distribution is a function of the material properties, the orientations and stacking sequence of the layers, and the size of the hole. Moreover, a pin inside a hole in a composite laminate introduces a bearing stress distribution, which raises the level of difficulty in analytically predicting the stresses around the hole.

The first authors that tried to analytically predict the stresses in an orthotropic plate were Lekhnitskii et al. [19]. In the book "Anisotropic Plates", the authors established the basic equations of the theory of elasticity in anisotropic bodies. Moreover, the book provides detailed steps for the calculation of strains and stresses in infinite orthotropic plates with circular or elliptic openings. Specifically, the authors implemented the method of complex variables and stress functions to predict the analytical expression of the stresses. Firstly, a stress function (Φ) is assumed based on the loading of the given problem. Later this stress function is implemented in the compatibility equation of anisotropic plates and the integration constants are obtained. Based on the integration constants the analytical equation of stresses can be derived. The main assumptions of the methods described in the book are continuous and homogeneous material, small deformations, and plane stress. Although Lekhnitskii et al. [19] provided a comprehensive and thorough analysis of the problem of an infinite orthotropic plate with a hole, they did not provide information for a finite-width composite joint.

Based on the theory of elasticity in anisotropic plates of Lekhnitskii et al. [19], De Jong [20] tried to establish a more accurate approach to calculate the stresses around a hole in pin-loaded orthotropic plates. The author assumed a sine series for the normal load applied by the pin inside the hole and determined the coefficients of the stress function series from the boundary conditions on the edge of the hole. Moreover, he continued his approach by assuming a rigid pin and a frictionless contact between the pin and the hole. In order to test his assumption of a sine distribution for the normal load, he compared it with two series distributions and observed that the difference between them is insignificant. Although the sine distribution has a small influence on the tangential stress distribution, De Jong concluded that the stress distribution is highly related to the material properties.

In his later work, De Jong [21] presented an approach where he could analytically predict the stresses in arbitrary-loading directions with friction assumed in the interface. He divided, the contact region into three areas, namely: slip, non-slip, and no-contact area, in order to apply a smoother mathematical approach and implement Coulomb's frictional law. Finally, the outcome of his research indicated that the application of friction on the interface significantly affects the stress distribution around the hole.

Following a different approach from De Jong [20], Zhang, and Ueng [22] developed a new analytical method to predict the stresses around a hole in a pin-loaded semi-infinite plate. Adhering to the formalism of Lekhnitskii et al. [19] and using his stress functions, the authors applied displacement expressions that satisfy the boundary conditions at the edge of the hole. In this way, the normal and shear stresses along the edge are calculated, without assuming the distribution of the pin load. The basic assumption of this method is that the pin is rigid and the friction between the hole and the pin is evident. Although friction is involved in the formulation, it can be ignored by setting the coefficient of friction to zero.

The stresses obtained with the method of De Jong [20] approach the results obtained with the method of Zhang, and Ueng [22]. Nevertheless, the latter method is less complex and simple to implement. The equations for the normal and shear stresses without friction, in a polar coordinate system, for a semi-infinite plate loaded with a pin, are the following.

$$\begin{aligned}\sigma_r = \frac{(c+1)}{cgr}u_o \cdot n(1-k)\cos 5\theta + \frac{u_o}{cgr}\left[(c+1)\,(3v_1 - 3k - kn) + \frac{c-1}{2}n(1-k)\right]\cos 3\theta \\ -\left[\frac{P}{\pi r} + \frac{(c-1)u_o}{2cgr}\,(2k - 2v_1 + nk + n) + \frac{(c+1)u_o}{cgr}\,(k - v_1 + n)\right]\cos\theta\end{aligned} \tag{2.3.1}$$

$$\tau_{r\theta} = -\frac{(c+1)u_o}{cgr} n(1-k)\sin 5\theta - \frac{u_o}{cgr}\left[(c+1)\left(k - v_1 + nk + 2n\right) + \frac{c-1}{2} n(1-k)\right]\sin\theta$$
$$+\left[\frac{P}{\pi r} - \frac{(c-1)u_o}{2cgr}\left(2k - 2v_1 + nk + n\right) - \frac{(c+1)u_o}{cgr}\left(k - v_1 + n\right)\right]\sin\theta \tag{2.3.2}$$

Where P is a point load in the edge of the pin, r is the radius of the hole and,

$$c = -\frac{10\left(k - v_1 + nk + 2n\right) - 11(1-k)}{10\left(k - v_1 + nk + 2n\right) - n(1-k)}$$
$$u_o = \frac{gP}{4\pi}\frac{10\left(k - v_1 + nk + 2n\right) - 11n(1-k)}{5n^2k(1-k) + \left[5\left(k - v_1 + nk + 2n\right) - 3n(1-k)\right]\left(k - v_1 + nk\right)} \tag{2.3.3}$$

$$k = \sqrt{\frac{E_1}{E_2}}$$
$$n = \sqrt{2(k - v_1) + \frac{E_1}{G}} \tag{2.3.4}$$
$$g = \frac{(1 - v_1 v_2)}{E_2} + \frac{k}{G}$$

E_1, E_2, G, v_1, v_2 are the in-plane engineering constants of the laminate in the global coordinate system. The normal stress in the tangential direction is algebraically more complex and its equation is given in a form of a summation.

$$\sigma_\theta = \sigma_{\theta 1} + \sigma_{\theta 2} + \sigma_{\theta 3} + \sigma_{\theta 4} + \sigma_{\theta 5} \tag{2.3.5}$$

The expression of each term is described thoroughly in the paper of Zhang, and Ueng [22]. Finally, the authors reached the same conclusion as De Jong, that the stress distribution around the hole is strongly affected by the material properties, stacking sequence, and the presence of friction between the pin and the hole.

2.4 Stress around holes in composite joints

As pointed out by Waszczak and Cruse [23], the catastrophic consequences of a joint failure, led engineers to implement severe penalty factors for mechanically fastened composite joints, making it very difficult to achieve lower weight in the design of a joint made of composite materials. For this reason, the authors presented an optimization algorithm that could estimate the strength of a joint from a preliminary design phase. Their algorithm was based on the theory of elasticity of anisotropic infinite plates, corrected by factors in order to account for the finite width of the joint. The principle of superposition was applied to the case of an infinite plate with a hole under tension and an infinite plate with a loaded hole. The stresses are calculated on a ply-by-ply base with the Classical Laminate Theory (CLT) and the maximum stress criterion was applied to detect failure.

The assumptions made by Waszczak and Cruse, are consistent with the assumptions made by authors that preceded them. In particular, the interaction is considered frictionless, the pin is rigid, it is a plane stress problem, and the distribution of load inside the hole is represented by a cosine series. The anisotropic correction factors are obtained by applying the boundary-integral equations

proposed by Cruse [24]. The optimization algorithm was implemented in a quasi-isotropic laminate [0/±45/90] in order to produce the optimal laminate for the specific geometry and applied load. The algorithm immediately removed all the 90 plies due to the fact that matrix failures in this type of ply outweigh the advantages it provides. Eventually, the authors concluded that in a composite joint, a laminate with $0/\pm45$ is more efficient than any laminate with $0/\pm\theta/90$ layer sequence. Finally, the algorithm predicted a failure load 20% higher than the experiments.

In the following years, Garbo and Ogonowski [25] developed a program to evaluate the structural integrity of composite joints. Their model called the "Bolted Joint Stress Field Model" (BJSFM), was based on the principle of elastic superposition, the elastic theory of anisotropic plates, CLT, and ply failure criteria. The principle of superposition was used to obtain the stresses for the cases of bearing and by-pass load, and the rest of the theories to detect the failure. Similarly to the method of Waszczak and Cruse [23], Garbo and Ogonowski superimposed the cases of unloaded and loaded holes in an infinite plate, and utilized geometry correction factors to account for the finite width geometry of the joint. In this method, however, they followed the theory of Whitney and Nuismer [17] and applied the failure criteria at a characteristic distance from the hole to account for the non-linearity of the material.

In this method, Garbo and Ogonowski assumed a cosine load distribution inside the half of the hole, and a frictionless contact. For the selection of the appropriate failure criteria, they conducted a trade study which can be observed in Figure 2.3. For the BJSFM model the Tsai-Hill [26] failure criterion, ignoring matrix failure, was used due to the fact is more conservative compared to Tsai-Wu [27], Hoffman [28], Maximum Stress/Strain [29] criterion. The authors concluded that finite width effects influence the stress distribution around the hole. In addition, the material orientation, laminate stiffness, and load orientation play a significant role in the stress concentration on the circumference of the hole.

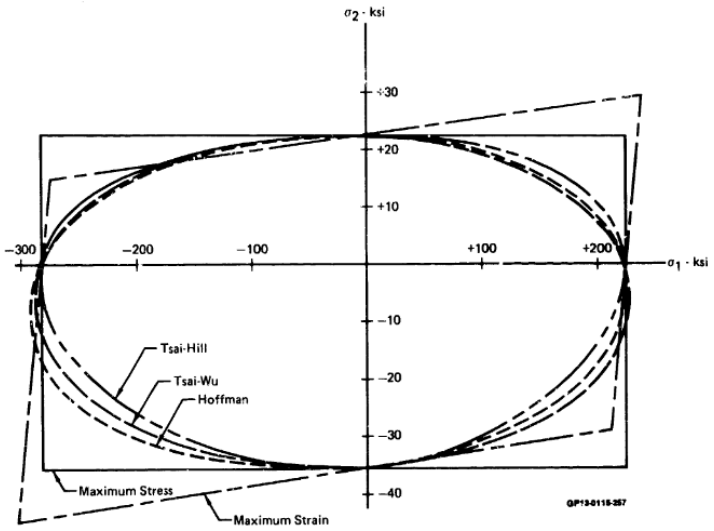

Figure 2.3: Trade study on the failure criteria [25].

For predicting the stresses in pin-loaded composite joints, Echavarria et al.[30] developed a new analytical method. Specifically, the authors derived a closed-form solution that was based on the methodology of De Jong [20]. Instead of using an arbitrary number of coefficients, Echavarria et al. [30] utilized only the first coefficient to obtain the integration constants of the stress functions. In this approach, the authors assumed a sine distributed load in the inside of the hole, a contact without friction, and a rigid pin. The main conclusion of their research is that the highest tensile stress would result in net tension failure only in joints with very low ratios of width over diameter

(w/D) and materials with low tensile strength. Additionally, shear stresses in the boundary of the hole are the main cause of shear-out failure. These findings are in accordance with the findings of Camanho and Matthews [10] who also connected net tension failure with high ratios of D/w.

It can be observed that some authors approximated the load inside the hole with a cosine series ([23], [25]) while Echavarria et al.[30] and De Jong [20] with a sine series. To further clarify, all of the preceding authors approached the load distribution inside the hole with a trigonometric function. The selection of sine or cosine depends on the global coordinate system of the problem (Figure 2.4), however, there is no difference between the two trigonometric functions regarding the slope or the magnitude of the load distribution.

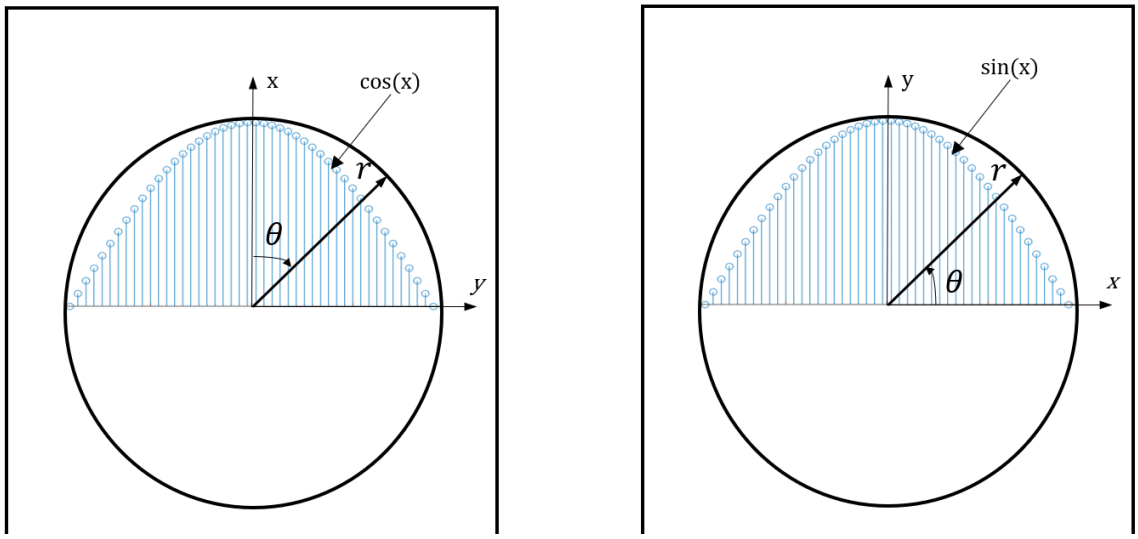

(a) Cosine distribution.

(b) Sine distribution.

Figure 2.4: Comparison of cosine and sine load distribution.

2.5 FE predictions in composite joints

Except for the analytical methods to predict the stresses in mechanically fastened composite joints, some authors approached the problem with numerical simulations. Various authors focused on describing the pin-loaded composite joint problem with two-dimensional finite element models while others tried with three-dimensional models. Regarding the 2-D models, it was obvious that with this approach, effects such as interlaminar stresses and delaminations, could not be predicted [10].

Regarding the authors that approached the problem with a 2-D model, Crews et al.[31] tried to describe the effect of the geometrical effects on the stress distribution. With an assumption of frictionless contact and rigid pin, the authors concluded that the stacking sequence and the anisotropic properties of the material have a significant effect on the magnitude and the location of the maximum hoop stress. Moreover, they associated the radial stress (σ_r) with the bearing failure, the hoop stress (σ_θ) with the net tension failure, and the shear stress $(\tau_{r\theta})$ with the shear-out failure mode. Finally, the geometric characteristic of the ratio of the width over the diameter (w/D) significantly affects the hoop stress and therefore the net tension failure mode.

In addition, York et al. [32] attempted to analyze the net tension failure in composite joints. In their research, a relationship between the geometric characteristics of the composite joint and the

stresses was established. The authors concluded the ratio of edge distance over the diameter (e/D) of the hole does not affect the stress profile in the net tension failure. However, the ratio of width over diameter (w/D) influences significantly the magnitude of stresses in the failure plane.

In the same time period, Chang et al. [33] predicted the failure load of pin-loaded composite joints with a numerical model. Their research is based on a 2-D numerical model with plane stress elements, where the joint is restrained in one edge and a cosine distributed load is applied inside of the hole. Chang et al. [33] reached the same conclusion as preceding authors, that as the ratio w/D decreases ($w/D \rightarrow 1$) the strength of the joint in tension also decreases. Moreover, they found out that for ratios below 3 ($w/D < 3$), the assumed cosine distribution of the load does not approach well the problem of the pin-loaded hole.

For the geometric characteristic of the edge distance (e), they discovered that for specific laminates ($[0/\pm45/90]_s$,$[0/90]_{2s}$) the failure load increases as the edge distance increases. Nevertheless, they concluded that for joints with $e/D > 4$, increasing the edge distance would not significantly affect the failure load. In addition, the authors managed to associate the mode of failure with the failure angle. In particular, as it is illustrated in Figure 2.5 when the failure is detected within 0 and 15 degrees from the center of the hole, the mode of failure can be assumed to be bearing. Following the same pattern, if the failure occurs between 30 and 60 degrees around the hole, the mode of failure would be shear out, and finally, if the failure is found between 75 and 90 degrees, the mode of failure would be net tension. In the degrees between the aforementioned ranges, a combination of failure modes can be assumed.

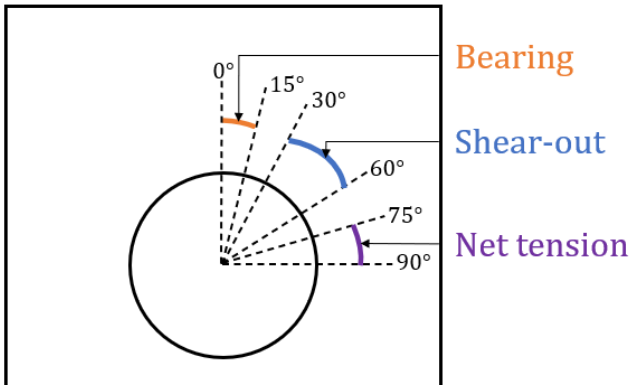

Figure 2.5: Location of failure along the circumference of the hole.

Ramamurthy [34] created a 2-D numerical model to investigate the interference between the hole and the pin. In the numerical model, a frictionless contact and a rigid pin were assumed. The author concluded that the maximum bearing stress is non-linearly associated with the magnitude of the applied force. Moreover, for high compressive loads in the laminate boundaries, the hoop stresses are low and the radial stresses are high.

Furthermore, it is substantiated by experimental data, the through-the-thickness effects play a significant role in the strength of the joint. In order to account for these effects, the simulation of the problem with three-dimensional finite element models is considered imperative. Matthews et al. [35], utilizing a 3-D model, investigated the stress distribution around a pin-loaded hole, with a frictionless interface and a rigid pin. In the conclusions, it is pointed out that the out-off-plane tensile stress (σ_z) is 7% of the bearing stress, and delaminations occur in the regions where σ_z is maximum.

As pointed out by Iarve [36], although three-dimensional models are beneficial in predicting the out-of-plane effects in composite laminates, they are computationally expensive. Moreover, when

modeling every layer with solid elements, challenges regarding the aspect ratio of the element can arise.

The most recent investigation of the stress distribution in pin-loaded composite joints is conducted by Koord et al. [37]. In their research, the authors conducted a trade study and evaluated which of the analytical methods is more accurate in predicting the stresses around the hole. The accuracy of the methods was evaluated with Digital Image Correlation (DIC) analysis, experimental data, and a 3-D finite element model. They concluded that analytical methods such as the approach of De Jong [20] can sufficiently approximate the stresses in composite joints where the ratio of the width over diameter (w/D) is higher than 3.

2.6 Composite Lug

In an aircraft structure, all the different components are assembled with the use of joints. There are many types of joints, and the most commonly used are lugs, shear clips, and bath-tub fittings. Each joint is designed for a specific load case and can be found in different locations on the aircraft [38]. Although every joint serves a unique purpose, the most commonly used joint for transferring load between two parts is the lug. As pointed out by Shridhar et al. [39] and Kathiresan et al. [40], lugs are used in connections between secondary and primary structures and are the most commonly used joints in the connection between the wings and the fuselage (Figure 2.6). Their design is very crucial, and any failure of such fitting could lead to devastating consequences for the aircraft structure [41].

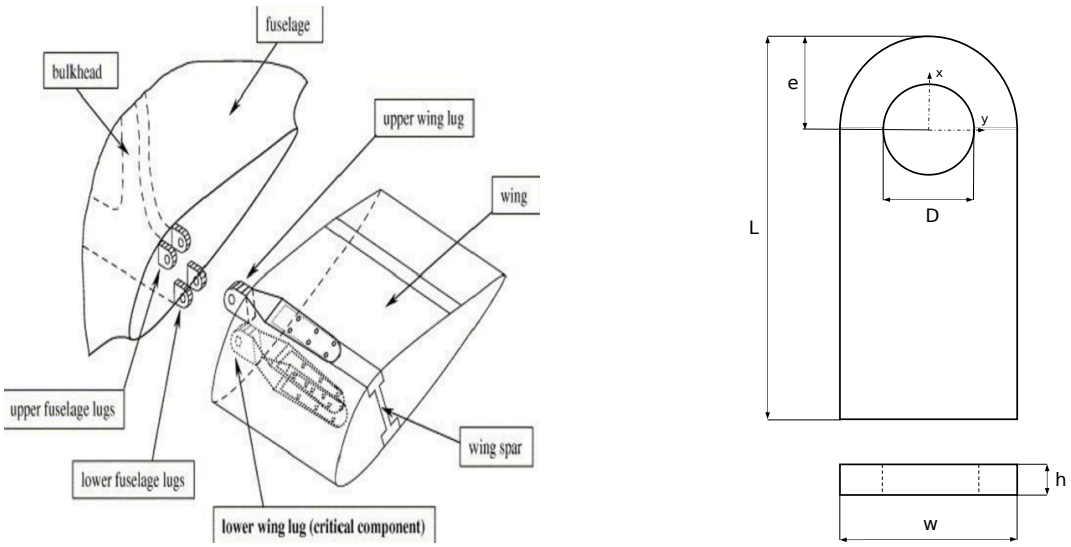

(a) Lugs in an aircraft [42]. (b) Characteristic dimensions of a lug.

Figure 2.6: Lug design.

Lugs are very effective in carrying loads in their plane. Although they are commonly used, the analytical prediction of the stresses around the hole is challenging, especially in composites where the stacking sequence, the material orientation, and the geometric characteristics of the lug influence the stress field. Kassapoglou and Townsend [43] developed an analytical solution to predict the strength of a pin-loaded lug under tension. In particular, the authors utilized the principle of superposition for the case of an infinite plate with a hole, and the case of a pin-loaded hole. In order to account for the finite width effects, geometric correction factors were used. Specifically, the expression provided by Tan [44] was utilized:

$$\frac{K_T}{K_T^{\infty}} = \frac{2 + (1 - D/w)^3}{3(1 - D/w)} \tag{2.6.1}$$

By assuming that the net tension failure of the lug is equated with the First Ply Failure of the laminate, the authors derived the strength of a finite-width composite lug in net tension:

$$F = \frac{6F^{tu}(w - D)t}{K_{\text{TOH}}^{\infty} + \frac{8}{\pi^2}\frac{w}{D}\left(2\left(\frac{w}{D}\right)^3 + \left(\frac{w}{D} - 1\right)^3\right)} \frac{\left(\frac{w}{D}\right)^3}{} \tag{2.6.2}$$

Where D is the diameter of the hole, w the width of the lug, F^{tu} the first ply failure strength of the laminate under tension, t the thickness of the laminate, and K_{TOH}^{∞} the open hole stress concentration factor for an infinite plate. The latter term can be calculated by the following expression:

$$K_{\text{TOH}}^{\infty} = 1 + \sqrt{\frac{2}{A_{22}}\left(\sqrt{A_{11}A_{22}} - A_{12} + \frac{A_{11}A_{22} - A_{12}^2}{2A_{66}}\right)} \tag{2.6.3}$$

With A_{ij} being the membrane stiffness of the laminate.

The authors concluded that for small values of the D/w ratio, bearing failure is more probable to happen, whereas for large values of D/w the bearing stress is small. Although the derived solution is within 10% of experimental data, this method could be further improved. Specifically, the authors pointed out that the approach on the internally loaded hole in an infinite plate is based on isotropic materials, and the overall method might not work for cases with high geometric and material nonlinearities.

Later Kassapoglou et al. [45] focused on predicting the strength of composite joints under tension in the other two in-plane failure modes. In particular, in the book "Design and Analysis of Composite Structures" in Chapter 11, the strength of the lug in shear-out failure mode is given by the expression:

$$F = \tau_{\text{ult}} D t \sqrt{\left(\frac{w}{D}\right)^2 - 1} \tag{2.6.4}$$

With the ultimate shear stress (τ_{ult}) being the failure strength of the first ply of the laminate under pure shear.

Furthermore, the bearing strength of the lug under tension is obtained by the equation:

$$F = \frac{F^{\text{bru}} D t}{\lambda} \cdot \frac{3\left(\frac{e}{D}\right)^2\left(\frac{e}{D} - \frac{1}{2}\right)}{2\left(\frac{e}{D}\right)^3 + \left(\frac{e}{D} - \frac{1}{2}\right)^3} \tag{2.6.5}$$

In equation 2.6.5, e corresponds to the edge distance (see Figure 2.4), λ is a factor accounting for the geometry of the specimen utilized to calculate the bearing strength, and F^{bru} is the first ply failure strength of the lug laminate in bearing.

The failure strength of a composite lug under tension is a function of material properties, stacking sequence, fiber orientation, and geometric characteristics of the lug. However, in order to achieve the optimal design, the failure loads of each failure mode should be close to each other. This translates to an optimally designed lug, which is not over-designed for any of the failure modes.

As it was mentioned, lugs are very effective in withstanding loads in their plane. However, it is very common that a composite joint can experience loads in the out-of-plane direction. The out-of-plane loading of a joint can lead to catastrophic consequences (delaminations) and failure before the design failure load is reached. This happens due to the fact that joint strength in the out-of-plane direction depends on the engineering properties of the matrix. In order to account for this and prevent a premature failure from happening there are some measures that can be implemented. As it is proposed by Kassapoglou et al. [45], a measure is to introduce alternative load paths. Moreover, there are manufacturing methods such as stitching and pinning which act as a reinforcement in the out-of-plane direction. In the designing of the laminate, this can be accounted for by reducing the in-plane engineering strengths (e.g., 2.5-5% of stitching can lead to a 10-20% in-plane compression strength reduction).

Kassapoglou et al. [45] performed a very good job in predicting the strength of a composite lug. Specifically, they compared the analytical results with test data of a composite lug under tension, and the largest deviation was 17.3%. Although the results of the analytical method correlate with test data, there is still room for improvement. Specifically, in the calculation of the net tension and shear-out failure mode, the stress is considered uniform throughout the area (shear-out, net tension failure area depicted in Figure 2.1). An equation that could predict the exact stress distribution in the failure area would lead to more accurate results. In conclusion, the authors did not provide a method to analytically calculate the stresses around the hole. It is evident from the literature that there is no previous attempt to derive an equation to predict the stresses in a composite lug.

2.7 Research questions

Finally, taking into account the research conducted by the preceding authors, the primary aim of the thesis is to derive analytical equations that can estimate the in-plane stress field around the hole of a pin-loaded composite lug under tension. Hence, the following research question is raised:

How to analytically predict the in-plane stress distribution around a hole in a pin-loaded composite lug under tension?

To address the research question effectively, it is of utmost importance to formulate additional questions that will aid in guiding the research process and provide a better understanding of the topic. Specifically, two sub-questions are: ***How accurate the analytical model will be?*** and ***How the accuracy of the model can be validated?***. Once the analytical model is developed, a numerical simulation will be created which will be utilized for validating the results of the analytical solution. In the process of creating the numerical model, more questions need to be answered. Specifically, given the fact that the aim is to predict the in-plane stresses, ***Which element type and material model will be selected?*** and ***What will be the boundary conditions that are going to be applied to the lug?***. The answers to these questions will play a significant role in the accuracy of the numerical model.

Diving deeper into the topic, it could be argued that the numerical simulations have also to be validated. The trustworthiness of the numerical model will be validated with tensile tests. In this field, more questions can be raised regarding the manufacturing of the test specimens and the overall testing process. In particular, ***How are the test specimens going to be manufactured?***, ***What sensors/equipment are going to be used?*** and ***What type of data are going to be gathered?***. After an answer to all of these questions is given, the results of the tests will validate (or not) the numerical simulation and the overall approach followed in this thesis project.

CHAPTER 3

Methodology

In this chapter the methodology to analytically predict the stresses in a composite lug will be presented. Additionally, the failure modes and criteria will be described and eventually, an overview of the design methodology for the optimal design of a composite lug will be given based on the analytical calculations.

3.1 Problem definition and assumptions

As mentioned in the previous chapter, lugs are a significant type of joint commonly used for connecting parts, due to their ability to transfer high loads in their plane. In order to assemble different components, a bolt or a pin is utilized.

In this research, a composite lug under tensile loads will be studied. The aim is to obtain the stresses around the hole and predict the location and type of failure (net tension, shear-out, bearing). In order to approach the problem analytically, some assumptions have to be made. In particular, this research will not study the effects of friction on the stress distribution, and hence a frictionless contact is assumed.

In addition, as pointed out by Hart-Smith [46], the stress distribution around the hole is influenced by the clamp-up force, the presence of a bushing, and whether the load is applied through a pin or a bolt. The influence of these characteristics will not be studied and a rigid pin is assumed. Furthermore, the pin-hole interface is assumed to be a tight fit and the effect of clearance between the pin and the hole is neglected.

Another important assumption for this approach is the loading conditions inside the hole. As it is substantiated by several academic papers and credible sources ([23], [25], [30], [33]), the load applied by the pin inside the hole can be described as a load that follows a cosinusoidal distribution. In addition, to further fortify this assumption, Bickley [47] tried to mathematically predict the load distribution inside a pin-loaded hole in an elastic plate. In his research, he concluded that the load inside the hole can be fairly well approached by a cosine distribution.

Finally, the modeling of the composite lug is approached as a plane stress problem. Hence, the thickness of every ply is considered small compared to the other dimensions. The strains ϵ_{xz}, ϵ_{yz}, ϵ_z are considered negligible and the loads are applied in the plane of the laminate. Interlaminar stresses will also be neglected and the delamination failure mode will not be taken into account. As can be observed from Figure 3.1, the principal axis of the laminate is aligned with the global coordinate system, and the 0^o direction of the plies is aligned with the loading direction.

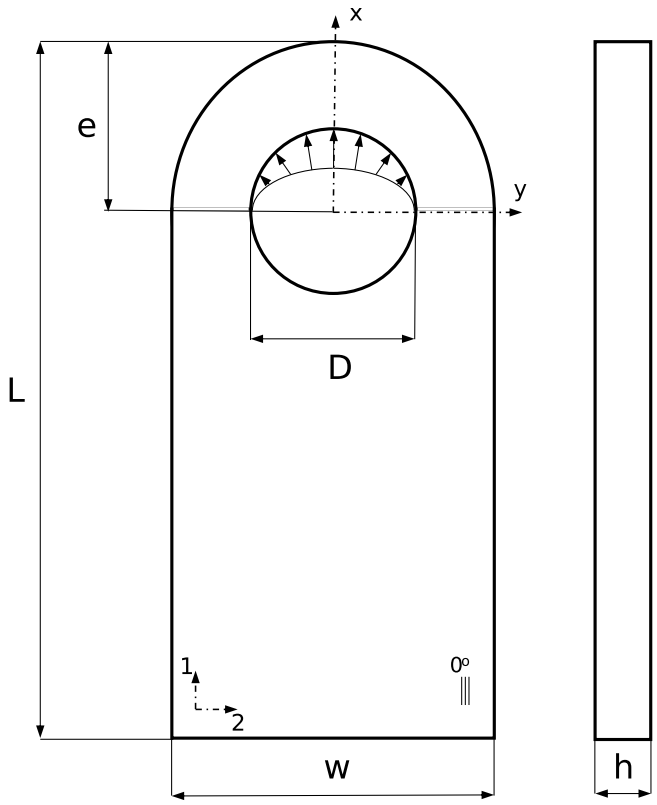

Figure 3.1: Characteristic geometry of a lug.

3.2 Analytical model and stress prediction

The methodology developed in this thesis is based on the principle of elasticity for isotropic materials developed by Timoshenko and Goodier [3] and for composite materials by Lekhnitskii et al. [19]. The analytical model developed utilizes the stress functions derived for composite materials and implements them in the equations of stresses for isotropic materials in a polar coordinate system.

The basis of the analytical model is the characteristic geometry of the lug. Unlike any other joint found in the literature, the semi-circular geometry of the top part of the lug resembles a curved beam. In addition, in a lug under tension, the stresses are crucial around the hole and particularly in the top part. Therefore, it would be safe to assume that failure would be more likely to occur around the hole rather than the rest of the joint.

The similarity in the geometry and the importance of the top part of the geometry of the lug led the focus of this research to develop an analytical model for calculating the stresses in a composite curved beam. The difference of this method regarding other methods developed for calculating the stresses in composite beams lies in the way the layers are laminated and the boundary conditions. In the research conducted by Cantero [48], the layers are stacked on top of each other parallel to the curvature. Whereas, in the method developed in this thesis, the layers are positioned perpendicularly to the curvature as can be observed in Figure 3.2.

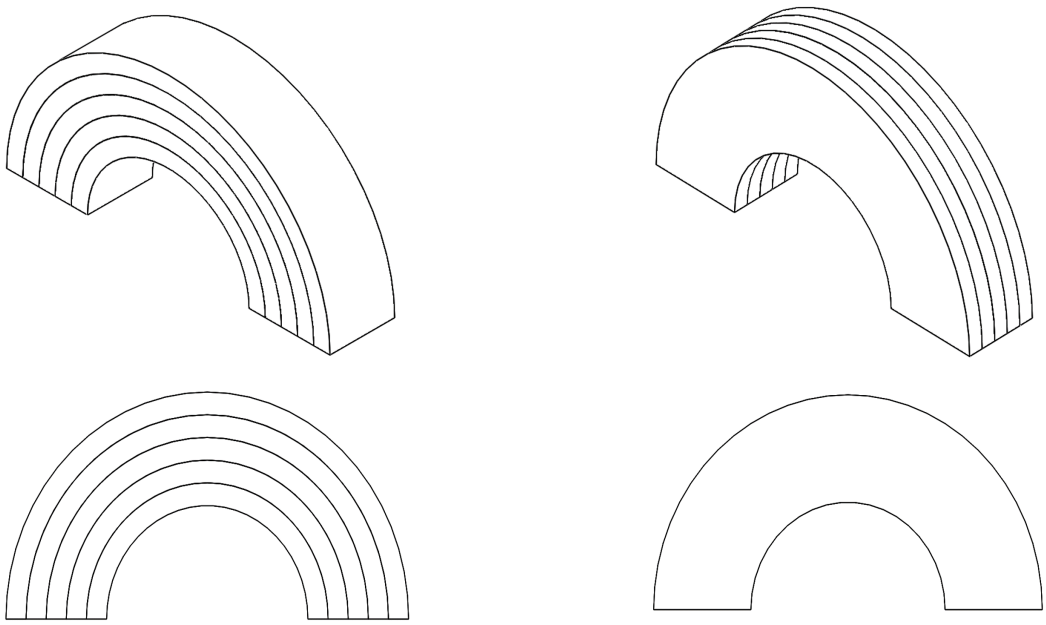

(a) Cantero [48] curved composite geometry. (b) Thesis approach curved composite geometry.

Figure 3.2: Differences between two approaches regarding the layer lamination direction.

3.2.1 Lekhnitskii approach

In the book "Anisotropic Plates" in Chapter 3, Lekhnitskii et al. [19], developed an approach to calculate the stresses in a composite curved beam. To analytically predict the stresses in an anisotropic body, the authors proposed some steps. First, the boundary conditions of the problem have to be established, and based on the type of loading, a stress function Φ has to be assumed. Later, this stress function has to be substituted in the compatibility equation for orthotopic plates with cylindrical anisotropy,

$$\begin{aligned}
&\frac{1}{E_\theta}\cdot\frac{\partial^4\Phi}{\partial r^4}+\left(\frac{1}{G_{r\theta}}-\frac{2\nu_{r\theta}}{E_r}\right)\frac{1}{r^2}\frac{\partial^4\Phi}{\partial r^2\partial\theta^2}+\frac{1}{E_r}\cdot\frac{1}{r^4}\cdot\frac{\partial^4\Phi}{\partial\theta^4}+\frac{2}{E_\theta}\cdot\frac{1}{r}\frac{\partial^3\Phi}{\partial r^3}\\
&\quad-\left(\frac{1}{G_{r\theta}}-\frac{2\nu_{r\theta}}{E_r}\right)\frac{1}{r^3}\cdot\frac{\partial^3\Phi}{\partial r\partial\theta^2}-\frac{1}{E_r}\cdot\frac{1}{r^2}\cdot\frac{\partial^2\Phi}{\partial r^2}\\
&\quad+\left(2\frac{1-\nu_{r\theta}}{E_r}+\frac{1}{G_{r\theta}}\right)\frac{1}{r^4}\cdot\frac{\partial^2\Phi}{\partial\theta^2}+\frac{1}{E_r}\cdot\frac{1}{r^3}\cdot\frac{\partial\Phi}{\partial r}\\
&=-\left[\frac{1-\nu_\theta}{E_\theta}\cdot\frac{\partial^2\bar{U}}{\partial r^2}+\frac{1-\nu_{r\theta}}{E_r}\cdot\frac{1}{r^2}\cdot\frac{\partial^2\bar{U}}{\partial\theta^2}+\left(\frac{2}{E_\theta}-\frac{1+\nu_{r\theta}}{E_r}\right)\frac{1}{r}\cdot\frac{\partial\bar{U}}{\partial r}\right]
\end{aligned}\tag{3.2.1}$$

Where, E_r and E_θ are the engineering constants of the laminate in the r, θ principal direction of the laminate. $G_{r\theta}$ is the shear modulus and ν_r, ν_θ the Poisson's ratios. Φ is the assumed stress function and the term $\frac{\partial\bar{U}}{\partial r}$ is a potential which for the case of a curved beam is set to zero.

In addition, after the stress function is substituted in the compatibility equation, both parts of the equation 3.2.1 are integrated, and an equation for the integration constants is obtained. These constants are utilized for obtaining the equations that predict the stresses in the specific geometry.

The geometry of the problem described by Lekhnitskii et al. [19] is depicted in Figure 3.3. Specifically, the curved composite beam is simply supported at the edges and a uniform external load (q) is applied on the outer edge.

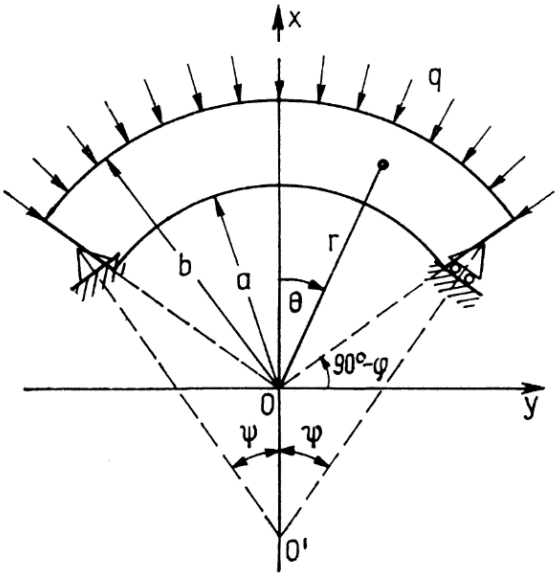

Figure 3.3: Boundary conditions of the curved composite beam [19].

The boundary conditions of this problem can be distinguished into two categories: boundary conditions that are global and boundary conditions that are satisfied in specific parts of the geometry. The global boundary conditions are the following,

$$\begin{aligned} r = a \rightarrow \sigma_r = 0, \tau_{r\theta} = 0 \\ r = b \rightarrow \sigma_r = -\frac{q}{h}, \tau_{r\theta} = 0 \end{aligned} \tag{3.2.2}$$

Where h is the thickness of the laminate. The boundary conditions at the edges ($\theta = \pm\phi$) are,

$$\begin{aligned} \int_a^b \sigma_\theta dr = -\frac{R_\theta}{h} = -\frac{qb}{h} \cdot \frac{\sin\varphi \sin(\varphi - \psi)}{\cos\psi} \\ \int_a^b \sigma_\theta r dr = 0 \\ \int_a^b \tau_{r\theta} dr = \pm\frac{R_r}{h} = \pm\frac{qb}{h} \cdot \frac{\sin\varphi \cos(\varphi - \psi)}{\cos\psi} \end{aligned} \tag{3.2.3}$$

With R_r, R_θ the reaction forces at the edges, and ϕ, θ, ψ the angles depicted in figure 3.3.

According to the authors, the problem of a curved composite beam under a uniform load along one edge can be described by a stress function in the form,

$$\Phi = f_0(r) + f_1(r)\cos\theta \tag{3.2.4}$$

Substituting the stress function equation (3.2.4) in the compatibility equation for orthotopic plates with cylindrical anisotropy (3.2.1), the terms of the stress function are obtained with respect to the integration constants. In particular,

$$\begin{aligned} f_0(r) = A + Br^2 + Cr^{1+k} + Dr^{1-k} \\ f_1(r) = Er^{1+\beta} + Fr^{1-\beta} + Gr + Hr\ln r \end{aligned} \tag{3.2.5}$$

With A, B, C, D, E, F, G, H being the integration constants and,

$$k = \sqrt{\frac{E_\theta}{E_r}}$$
$$\beta = \sqrt{1 + \frac{E_\theta}{E_r}(1 - 2\nu_{r\theta}) + \frac{E_\theta}{G_{r\theta}}} \tag{3.2.6}$$

This approach acts as a starting point for deriving the equations for predicting the stresses in a composite lug. However, further modifications to this method have to be made regarding the boundary conditions and the load distribution. It is worth noting that the approach of Lekhnitskii et al. [19] is not thoroughly documented and some steps are missing regarding the derivation of the final stress equations. For this reason, further research is required.

3.2.2 Timoshenko approach

In the book "Theory of Elasticity" Timoshenko and Goodier [3] presented various methods to derive equations for calculating the stresses in various engineering problems. In particular, in Chapter 4 of the book, the authors provide a method to derive the stresses in polar coordinates in two-dimensional problems.

When the authors reported this approach, there was not sufficient knowledge of composite materials. However, it can be assumed that the method they developed is valid for every type of material (anisotropic or isotropic). Moreover, the use of a polar coordinate system (r, θ) is considered beneficial in cases where the geometry of the problem is circular (e.g., rings, disks, curved beams). The stresses in the polar coordinate system are distinguished in stresses in the radial direction (σ_r), the tangential (σ_θ), and shear stresses $(\tau_{r\theta})$.

The stresses are given by the following equations,

$$\sigma_r = \frac{1}{r}\frac{\partial \Phi}{\partial r} + \frac{1}{r^2}\frac{\partial^2 \Phi}{\partial \theta^2} \tag{3.2.7}$$

$$\sigma_\theta = \frac{\partial^2 \Phi}{\partial r^2} \tag{3.2.8}$$

$$\tau_{r\theta} = \frac{1}{r^2}\frac{\partial \Phi}{\partial \theta} - \frac{1}{r}\frac{\partial^2 \Phi}{\partial r \partial \theta} = -\frac{\partial}{\partial r}\left(\frac{1}{r}\frac{\partial \Phi}{\partial \theta}\right) \tag{3.2.9}$$

With Φ being the stress function with respect to r and θ. After deriving the stress equations, they have to be validated by utilizing the equilibrium equation in the radial and tangential directions. Specifically,

$$\frac{\partial \sigma_r}{\partial r} + \frac{1}{r}\frac{\partial \tau_{r\theta}}{\partial \theta} + \frac{\sigma_r - \sigma_\theta}{r} = 0 \tag{3.2.10}$$

$$\frac{1}{r}\frac{\partial \sigma_\theta}{\partial \theta} + \frac{\partial \tau_{r\theta}}{\partial r} + \frac{2\tau_{r\theta}}{r} = 0 \tag{3.2.11}$$

In addition, there is a second stage of validation of the stress equations. This stage entails the substitution of the stress equations in a compatibility equation for strains,

$$\frac{\partial^2 \varepsilon_\theta}{\partial r^2} + \left(\frac{2}{r}\right)\frac{\partial \varepsilon_\theta}{\partial r} - \left(\frac{1}{r}\right)\frac{\partial \varepsilon_r}{\partial r} + \left(\frac{1}{r^2}\right)\frac{\partial^2 \varepsilon_r}{\partial \theta^2} - \left(\frac{1}{r^2}\right)\frac{\partial \gamma_{r\theta}}{\partial \theta} - \left(\frac{1}{r}\right)\frac{\partial^2 \gamma_{r\theta}}{\partial r \partial \theta} = 0 \tag{3.2.12}$$

3.2.3 Timoshenko/Lekhnitskii approach

The method developed in this thesis will be referred to as Timoshenko/Lekhnitskii approach because it incorporates elements from both methods. Contrary to the approach of Lekhnitskii et al. [19], the load is distributed in the inner edge and the distribution is not uniform. Moreover, the edges are pinned in order to account for the fact that the geometry of the lug continues in that region. A graphical representation of the problem that will be studied is depicted in Figure 3.4.

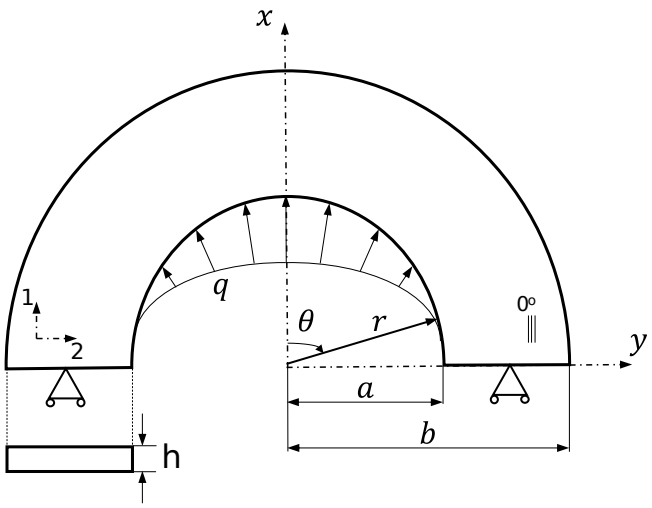

Figure 3.4: Geometry of the thesis approach.

Combining equations 3.2.4 and 3.2.5 the stress function for the current problem is,

$$\Phi = A + Br^2 + Cr^{1+k} + Dr^{1-k} + (Er^{1+\beta} + Fr^{1-\beta} + Gr + Hr\ln r)\cos\theta \tag{3.2.13}$$

Substituting the stress function (3.2.13) in the equation for the stresses (3.2.7, 3.2.8, 3.2.9), the expressions for the stresses in the radial and tangential direction can be obtained. In particular the radial stress σ_r is,

$$\begin{aligned}\sigma_r = \frac{1}{r^2}(&-D(-1+k)r^{1-k} - Fr^{1-\beta}\cos(\theta)\beta + C(1+k)r^{1+k} \\ &+Er^{1+\beta}\cos(\theta)\beta + 2Br^2 + H\cos(\theta)r)\end{aligned} \tag{3.2.14}$$

The stress σ_θ in the tangential direction is,

$$\begin{aligned}\sigma_\theta = \frac{1}{r^2}(&\cos(\theta)F\beta(-1+\beta)r^{1-\beta} + kD(-1+k)r^{1-k} + \cos(\theta)E\beta(1+\beta)r^{1+\beta} \\ &+Ck(1+k)r^{1+k} + 2Br^2 + H\cos(\theta)r)\end{aligned} \tag{3.2.15}$$

Finally the shear stress $\tau_{r\theta}$ is,

$$\tau_{r\theta} = \frac{1}{r^2}\sin(\theta)\left(Er^{1+\beta}\beta - Fr^{1-\beta}\beta + Hr\right) \tag{3.2.16}$$

Consequently, the expressions of stresses (3.2.14, 3.2.15, 3.2.16) are validated by substituting the results in the equilibrium equations 3.2.10, 3.2.11. The second step of validation is to substitute the equations for stresses in a compatibility equation of strains (3.2.12). In a polar coordinate system and in an orthotropic body, the stresses and strains are related with the following equations [19],

$$\epsilon_r = \frac{1}{E_r}\sigma_r - \frac{\nu_{\theta r}}{E_\theta}\sigma_\theta$$

$$\epsilon_\theta = -\frac{\nu_{r\theta}}{E_r}\sigma_r + \frac{1}{E_\theta}\sigma_\theta \tag{3.2.17}$$

$$\gamma_{r\theta} = \frac{1}{G_{r\theta}}\tau_{r\theta}$$

By getting the strains in the polar coordinate system and substituting them into the compatibility equation (3.2.12), the second step of validation is completed. Since the equilibrium and compatibility equations are satisfied, the following step is to specify the integration constants.

Boundary conditions

The integration constants are specified by implementing the boundary conditions. The global boundary conditions of the specific problem are,

$$r = a \rightarrow \begin{cases} \sigma_r = -\dfrac{q}{h} \\ \tau_{r\theta} = 0 \end{cases} \tag{3.2.18}$$

$$r = b \rightarrow \begin{cases} \sigma_r = 0 \\ \tau_{r\theta} = 0 \end{cases} \tag{3.2.19}$$

It is important to mention that q is defined as a load per unit length. In order to have equilibrium in the units, the second part of the radial stress in equation 3.2.18 has to be divided by the thickness of the laminate. The negative sign is implemented due to the fact the geometry of the hole has to be in compression. Since there is no friction on either the internal or external edge the shear stress is set equal to zero. Finally, there is no load applied to the external edge and hence the radial stress is zero.

In order to specify the boundary conditions at the edges, it is crucial to create a free-body diagram which is illustrated in Figure 3.5.

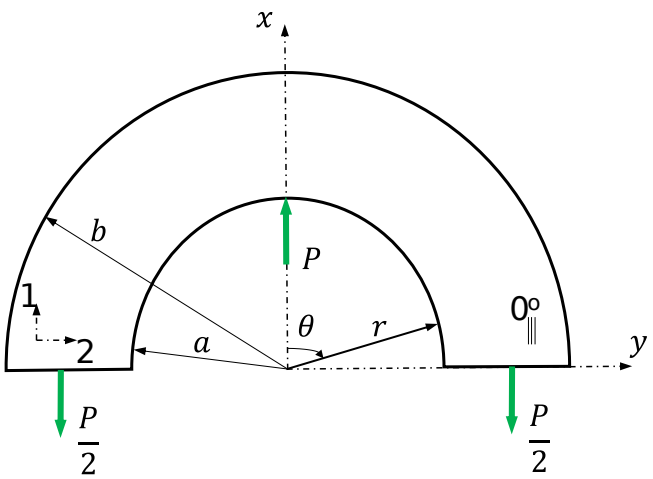

Figure 3.5: Free body diagram.

Taking this into account, the boundary conditions of the specific problem at the corners ($\theta = \pm\frac{\pi}{2}$),

$$\int_a^b \sigma_\theta dr = \frac{P}{2h} \tag{3.2.20}$$

$$\int_a^b \sigma_\theta r dr = 0 \tag{3.2.21}$$

$$\int_a^b \tau_{r\theta} dr = 0 \tag{3.2.22}$$

The right term of equation 3.2.20 is divided with the thickness of the laminate in order to have equilibrium between the two parts. P is the maximum point force applied at the center of the inner edge of the hole. Equation 3.2.21 refers to the equilibrium of the moment at the corner which is zero with respect to the center of the hole. Finally, equation 3.2.22 refers to the equilibrium of forces in the y direction, which is also zero at $\theta = \pm\frac{\pi}{2}$.

As pointed out in the literature, the load applied by the pin can be approached with a cosine distribution. The magnitude of q can be determined by analyzing the problem in more detail and specifically by selecting a small part of the geometry. In particular, as it can be noticed in Figure 3.6, the force in the radial direction is,

$$dF_r = \sigma_r \cdot h \cdot a d\theta \tag{3.2.23}$$

The radial stress,

$$\sigma_r = \frac{q}{h} \cdot \cos\theta \tag{3.2.24}$$

And the force in the x direction,

$$dF_x = dF_r \cdot \cos\theta \tag{3.2.25}$$

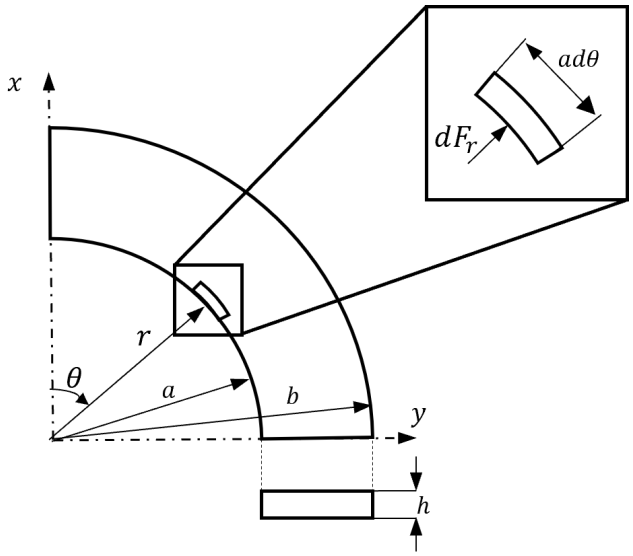

Figure 3.6: Discretization of the geometry to define the magnitude of the applied load.

Substituting equation 3.2.24 in 3.2.23 and the result in 3.2.25,

$$dF_x = q \cdot \cos^2\theta \cdot a d\theta \tag{3.2.26}$$

In addition, from the boundary conditions, it can be calculated that,

$$\int_0^{\frac{\pi}{2}} dF_x d\theta = \frac{P}{2} \tag{3.2.27}$$

Finally by integrating equation 3.2.26, and implementing the equation 3.2.27, the value of the q can be determined,

$$\left.\begin{array}{c} \int_0^{\frac{\pi}{2}} dF_x d\theta = \int_0^{\frac{\pi}{2}} q \cdot cos^2\theta \cdot a d\theta \\ \int_0^{\frac{\pi}{2}} dF_x d\theta = \frac{P}{2} \end{array}\right\} \rightarrow q = \frac{2P}{\pi a} \tag{3.2.28}$$

This result is consistent with the literature ([22], [30]) that proposed that the value of the radial stress (σ_r) is equal to the bearing stress times a trigonometric function:

$$\sigma_r = \frac{q}{h} \cdot \cos\theta = \underbrace{\frac{2P}{\pi a h}}_{bearing\ stress} \cdot \cos\theta \tag{3.2.29}$$

Having specified the boundary conditions, the next step is to specify the integration constants. By substituting the stress equations in terms of integration constants (3.2.14, 3.2.15, 3.2.16) in the boundary conditions (3.2.18-3.2.22) the following equations are obtained.

For the boundary condition $\sigma_{r,\ r=a} = -\frac{q}{h}$,

$$\begin{aligned} \frac{1}{a^2}(-D(-1+k)a^{1-k} - Fa^{1-\beta}\cos(\theta)\beta + Ca^{1+k}(1+k) \\ +Ea^{1+\beta}\cos(\theta)\beta + 2Ba^2 + H\cos(\theta)a) = -\frac{q}{h} \end{aligned} \tag{3.2.30}$$

For $\sigma_{r,\ r=b} = 0$,

$$\begin{aligned} \frac{1}{b^2}(-D(-1+k)b^{1-k} - Fb^{1-\beta}\cos(\theta)\beta + Cb^{1+k}(1+k) \\ +Eb^{1+\beta}\cos(\theta)\beta + 2Bb^2 + H\cos(\theta)b) = 0 \end{aligned} \tag{3.2.31}$$

For $\tau_{r\theta,\ r=a} = 0$,

$$\frac{1}{a^2}(\sin(\theta)\left(Ea^{1+\beta}\beta - Fa^{1-\beta}\beta + Ha\right)) = 0 \tag{3.2.32}$$

For $\tau_{r\theta,\ r=b} = 0$,

$$\frac{1}{b^2}(\sin(\theta)\left(Eb^{1+\beta}\beta - Fb^{1-\beta}\beta + Hb\right)) = 0 \tag{3.2.33}$$

For $\int_a^b \sigma_\theta|_{\theta=\pm\frac{\pi}{2}} dr = \frac{P}{2h}$,

$$\begin{aligned} -\frac{1}{ab}(2Ba^2b - 2Bab^2 + Ca^{1+k}bk - Cb^{1+k}ak - Da^{1-k}bk \\ +Db^{1-k}ak + Ca^{1+k}b - Cb^{1+k}a + Da^{1-k_b}b - Db^{1-k}a) = \frac{P}{2h} \end{aligned} \tag{3.2.34}$$

For $\int_a^b \sigma_\theta|_{\theta=\pm\frac{\pi}{2}} r dr = 0$,

$$-Ba^2 - Ca^{1+k}k + Da^{1-k}k + Bb^2 + Cb^{1+k}k - Db^{1-k}k = 0 \tag{3.2.35}$$

For $\int_a^b \tau_{r\theta}|_{\theta=\pm\frac{\pi}{2}} dr = 0$,

$$-\frac{1}{ab}(-H\ln(b)ab + H\ln(a)ab + Ea^{1+\beta}b - Eb^{1+\beta}a + Fa^{1-\beta}b - Fb^{1-\beta}a) = 0 \tag{3.2.36}$$

From these equations, it can be observed that the integration constants A and G are eliminated. Moreover, equation 3.2.33 did not aid in solving the system and hence it was discarded. Therefore, a system of 6 unknowns and 6 equations is created. The solution of the 6x6 system will provide the integration constants and eventually, the equations that predict the stress distribution for the specific problem. The values of the integration constants can be found in Appendix A. One last parameter that has to be defined before progressing to the failure analysis, is the engineering constants of the laminate.

3.2.4 Engineering Constants

In order to better understand the stress distribution in the specific geometry and more specifically in the laminate, a small introduction will be made about the Classical Laminate Theory (CLT). A more detailed overview of the CLT can be found in the book "Engineering Mechanics of Composite Materials" in Chapter 4 [49] and in Appendix B of this report.

In general, a laminate has two principal directions, the direction of the fibers (which is denoted by 1) and the direction perpendicular to the fibers (denoted by 2 and refers to the matrix). However, the principal directions do not always coincide with the global coordinate system of the laminate. The transformation between the lamina and laminate can be achieved with a transformation matrix (T). The same transformation can be applied to transform the layer's material properties in the global system.

When a laminate is subjected to a load (force, moment, or combination), stresses and strains are developed. The strains are connected with the loads with the ABD matrix, which is a table that contains information about the stiffness of the laminate. The strains are calculated at a laminate level and are connected with the stresses. At a later stage, the stresses at a laminate level (global system) are transformed into stresses at the layer level (principal system). Comparing the principal stresses with the material strength it can be concluded whether the ply will fail.

In the design of laminates made of composite materials, it is very common to use engineering constants to describe the laminate's stiffness. These constants can be obtained from simple tensile tests but also analytically from the ABD matrix. For a balanced and symmetric laminate in stretching, the flexural engineering constants are given by the following equations [45],

$$\begin{aligned} E_x &= \frac{1}{ha_{11}}, \quad E_y = \frac{1}{ha_{22}} \\ G_{xy} &= \frac{1}{ha_{66}}, \quad \nu_{xy} = -\frac{a_{12}}{a_{11}} \\ \nu_{yx} &= -\frac{a_{12}}{a_{22}} \end{aligned} \tag{3.2.37}$$

With $a_{i,j}$ being the entries of the inverse A matrix of the laminate.

As can be observed from the equations of the boundary conditions (3.2.30-3.2.36), there are some variables (k, β) that are a function of the engineering constants of the laminate in the radial (E_r) and tangential direction (E_θ). In order to determine the engineering constants in the r and θ direction, a transformation has to be applied. Specifically [19],

$$\frac{1}{E_r} = \frac{\cos^4(\theta)}{E_x} + \left(\frac{1}{G_{xy}} - \frac{2\nu_{xy}}{E_x}\right)\cos^2(\theta)\sin^2(\theta) + \frac{\sin^4(\theta)}{E_y} \Rightarrow$$

$$E_r = \frac{1}{\frac{\cos^4(\theta)}{E_x} + \left(\frac{1}{G_{xy}} - \frac{2\nu_{xy}}{E_x}\right)\cos^2(\theta)\sin^2(\theta) + \frac{\sin^4(\theta)}{E_y}} \tag{3.2.38}$$

$$\frac{1}{E_\theta} = \frac{\sin^4(\theta)}{E_x} + \left(\frac{1}{G_{xy}} - \frac{2\nu_{xy}}{E_x}\right)\cos^2(\theta)\sin^2(\theta) + \frac{\cos^4(\theta)}{E_y} \Rightarrow$$

$$E_\theta = \frac{1}{\frac{\sin^4(\theta)}{E_x} + \left(\frac{1}{G_{xy}} - \frac{2\nu_{xy}}{E_x}\right)\cos^2(\theta)\sin^2(\theta) + \frac{\cos^4(\theta)}{E_y}} \tag{3.2.39}$$

$$\frac{1}{G_{r\theta}} = 4\left(\frac{1}{E_x} + \frac{1}{E_y} + \frac{2\nu_{xy}}{E_x}\right)\cos^2(\theta)\sin^2(\theta) + \frac{\left(\cos^2(\theta) - \sin^2(\theta)\right)^2}{G_{xy}} \Rightarrow$$

$$G_{r\theta} = \frac{1}{4\left(\frac{1}{E_x} + \frac{1}{E_y} + \frac{2\nu_{xy}}{E_x}\right)\cos^2(\theta)\sin^2(\theta) + \frac{\left(\cos^2(\theta) - \sin^2(\theta)\right)^2}{G_{xy}}} \tag{3.2.40}$$

$$\nu_{r\theta} = -E_r\left(\frac{1}{E_x} + \frac{1}{E_y} - \frac{1}{G_{xy}}\right)\cos^2(\theta)\sin^2(\theta) + \frac{E_r\left(\cos^4(\theta) + \sin^4(\theta)\right)\nu_{xy}}{E_x} \tag{3.2.41}$$

It can be noticed that the engineering constants in the r, θ coordinate system are dependent on the angle θ. This is consistent with the idea that the stiffness of the laminate should not be the same around the hole.

Additionally, in order to obtain the variables k and β (3.2.6), the ratio of E_r/E_θ is needed. Since k and β are constants, the ratio of the engineering constants in every angle is obtained and then averaged to acquire a unique value. Moreover, the average of every engineering constant is calculated by integrating the equations around the hole ($-\pi/2 < \theta < \pi/2$). In particular,

$$\left(\frac{1}{E_r}\right)_{avg} = \frac{1}{\pi}\int_{-\frac{\pi}{2}}^{\frac{\pi}{2}} \frac{1}{E_r} d\theta = \frac{-2E_yG_{xy}\nu_{xy} + E_xE_y + 3G_{xy}E_x + 3E_yG_{xy}}{8E_xG_{xy}E_y} \Rightarrow$$

$$E_{r,avg} = \frac{8E_xG_{xy}E_y}{-2E_yG_{xy}\nu_{xy} + E_xE_y + 3G_{xy}E_x + 3E_yG_{xy}} \tag{3.2.42}$$

$$\left(\frac{1}{E_\theta}\right)_{avg} = \frac{1}{\pi}\int_{-\frac{\pi}{2}}^{\frac{\pi}{2}} \frac{1}{E_\theta} d\theta = \frac{-2E_yG_{xy}\nu_{xy} + E_xE_y + 3G_{xy}E_x + 3E_yG_{xy}}{8E_xG_{xy}E_y} \Rightarrow$$

$$E_{\theta,avg} = \frac{8E_xG_{xy}E_y}{-2E_yG_{xy}\nu_{xy} + E_xE_y + 3G_{xy}E_x + 3E_yG_{xy}} \tag{3.2.43}$$

$$\left(\frac{1}{G_{r\theta}}\right)_{avg} = \frac{1}{\pi}\int_{-\frac{\pi}{2}}^{\frac{\pi}{2}} \frac{1}{G_{r\theta}} d\theta = \frac{2E_y G_{xy} v_{xy} + E_x E_y + G_{xy} E_x + E_y G_{xy}}{2E_x G_{xy} E_y}$$

$$G_{r\theta,avg} = \frac{2E_x G_{xy} E_y}{2E_y G_{xy} v_{xy} + E_x E_y + G_{xy} E_x + E_y G_{xy}} \tag{3.2.44}$$

$$v_{r\theta,avg} = \frac{1}{\pi}\int_{-\frac{\pi}{2}}^{\frac{\pi}{2}} v_{r\theta} d\theta = \frac{\left(6E_y G_{xy} v_{xy} + E_x E_y - G_{xy} E_x - E_y G_{xy}\right) E_{r,avg}}{8E_x G_{xy} E_y} \tag{3.2.45}$$

In conclusion, the engineering constants of the laminate have been obtained. Therefore, by substituting the values of k and β (3.2.6) in the boundary conditions (3.2.30-3.2.36), the integration constants can be calculated.

3.3 Failure mode analysis

After specifying the integration constants, the stresses calculated from equations 3.2.14-3.2.16 are expressed in a radial and tangential direction. In order to obtain the stress distribution inside the laminate, the stresses have to be transformed in the global coordinate system. Specifically, the stresses in the global coordinate system are given by the following equations [19],

$$\begin{aligned}
\sigma_x &= \sigma_r \cos^2(\theta) + \sigma_\theta \sin^2(\theta) - 2\tau_{r\theta} \sin(\theta)\cos(\theta) \\
\sigma_y &= \sigma_r \sin^2(\theta) + \sigma_\theta \cos^2(\theta) + 2\tau_{r\theta} \sin(\theta)\cos(\theta) \\
\tau_{xy} &= (\sigma_r - \sigma_\theta)\sin(\theta)\cos(\theta) + \tau_{r\theta}\left(\cos^2\theta - \sin^2\theta\right)
\end{aligned} \tag{3.3.1}$$

By defining the radius and the angle, the stress equations can predict the stress in the specific location. Repeating the same process for a range of radii and angles, the stress distribution of the entire geometry can be predicted. The next step of the process is to calculate the stresses in every layer.

The stresses in the global coordinate system are multiplied by the thickness of the laminate. This process is used in order to obtain the internal loads applied to the laminate (N_x, N_y, N_{xy}). Therefore, by having specified the internal loads and the ABD matrix, the strains in every layer (in the layers coordinate system) at the specific location of the laminate can be estimated. Repeating this process for every location on the geometry, the stress distribution in a lamina level (σ_1, σ_2, τ_{12}) can be predicted. A schematic of this approach is depicted in Figure 3.7.

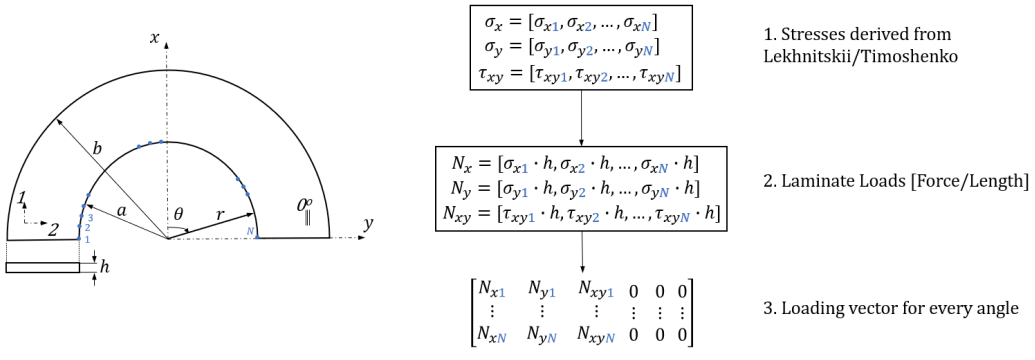

Figure 3.7: Approach of calculating the stresses per layer.

The stresses of every layer are compared with the strength of the material by implementing specific failure criteria. After checking the stresses of every layer throughout the entire geometry, the exact location of failure can be determined. Based on the location of failure (failure angle), and by applying the observations of Chang et al. [33], the failure mode of the lug (net tension, shear-out, bearing) can also be specified.

3.3.1 Failure criteria

According to Reifsnider et al.[50] there are more than 30 criteria/theories that can predict the failure in a composite laminate. These criteria can be distinguished into three categories, namely the limit criteria, the interaction criteria, and the criteria with independent failure modes.

The limit criteria compare the stresses in a lamina level with the material strength separately and can predict the failure load and the mode of failure (e.g., fiber failure, matrix cracking). However, the interaction between stress components is not taken into account. Some of the failure criteria included in this category are the *Maximum Strain* and *Maximum Stress*.

The interaction failure criteria can predict the failure load but not the failure mode. According to Reifsnider et al. [50], these criteria are curve-fitting techniques without a solid theoretical basis. These criteria use polynomial equations of the stress components, and failure is assumed when the equation is satisfied [51]. This category includes criteria such as the *Tsai-Hill*, *Tsai-Wu*, and *Yamada-Sun*.

The criteria with independent failure modes can predict the mode and load of failure. The failure of matrix or fiber is well distinguished in this category. Based on the study of Reifsnider et al. [50], these criteria are more conservative than the limit criteria which according to the authors are used to introduce simplicity to a study. Criteria included in this category are *Hashin*, *Hashin-Rotem*, and *Puck*.

The criteria mentioned in this section, are a small sample of the wide range of criteria used in the design of a composite structure. The criteria that are going to be utilized in this research are from the category of the criteria with the independent failure modes. This choice is substantiated by the fact that the criteria in this category are conservative, and can predict the mode and load of failure.

In order to ensure that the thesis topic remains within manageable time bounds, it became essential to select a limited yet representative sample of failure criteria of this category. Consequently, two failure criteria, namely Puck and Hashin, were selected. The choice of specific criteria is further fortified by the comparative analysis of Zarouchas [52] who presented that Puck and Hashin have good predictive accuracy and require few empirical parameters and are easy to implement.

Hashin

As mentioned previously, Hashin is one of the criteria in the category with independent failure modes. Specifically, with Hashin the fiber and matrix failure in tension or compression can be detected. The equations of this failure criterion are [53],

Fiber failure in tension ($\sigma_1 > 0$):

$$\left(\frac{\sigma_1}{X_t}\right)^2 + \left(\frac{\tau_{12}}{S_{12}}\right)^2 = 1 \tag{3.3.2}$$

Fiber failure in compression ($\sigma_1 < 0$):

$$\frac{\sigma_1}{-X_c} = 1 \tag{3.3.3}$$

Matrix failure in tension ($\sigma_2 > 0$):

$$\left(\frac{\sigma_2}{Y_t}\right)^2 + \left(\frac{\tau_{12}}{S_{12}}\right)^2 = 1 \tag{3.3.4}$$

Matrix failure in compression ($\sigma_2 < 0$):

$$\left(\frac{\sigma_2}{Y_c}\right)^2 + \left(\frac{\tau_{12}}{S_{12}}\right)^2 = 1 \tag{3.3.5}$$

With X_t, X_c, the strength of the material in the longitudinal direction in tension and compression. S_{12} is the shear strength of the material, and Y_t, Y_c is the strength of the material in the transverse direction in tension and compression.

Puck

Puck belongs in the same category of failure criteria. Except for the fiber failure, the Puck failure criterion can distinguish three types of matrix failure or else Inter Fiber Failure (IFF). The IFF is considered a brittle failure leading to a fracture plane parallel to the fibers at a specific failure angle θ_{fp} [54]. The three IFF failure modes (Mode A, B, C) are depicted in Figure 3.8.

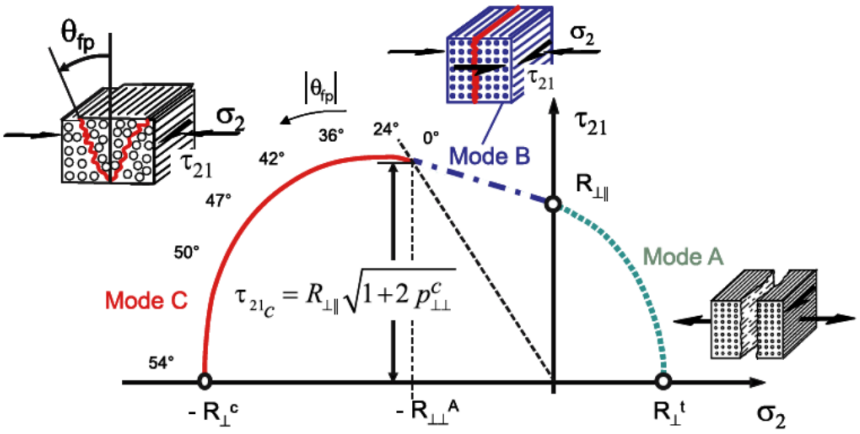

Figure 3.8: Inter Fiber Failure modes [52].

The different types of failure are given by the following equations,

Fiber failure in tension ($\sigma_1 > 0$) [45]:

$$\frac{E_1}{X_t}\left[\varepsilon_1 + \frac{\nu_{12}}{E_1} m_\sigma \sigma_2\right] = 1 \tag{3.3.6}$$

Fiber failure in compression ($\sigma_1 < 0$) [45]:

$$\frac{E_1}{-X_c}\left[\varepsilon_1 + \frac{\nu_{12}}{E_1} m_\sigma \sigma_2\right] = 1 \tag{3.3.7}$$

IFF Mode A ($\sigma_2 > 0$) [52]:

$$\sqrt{\left(\frac{\sigma_{12}}{S_{12}}\right)^2+\left(1-p_{12}^{(+)}\frac{Y_T}{S_{12}}\right)^2\left(\frac{\sigma_2}{Y_T}\right)^2}+p_{12}^{(+)}\frac{\sigma_2}{S_{12}}=1 \tag{3.3.8}$$

IFF Mode B ($\sigma_2<0$) and ($0\le\left|\frac{\sigma_2}{\sigma_{12}}\right|\le\frac{\sigma_{23}^{A}}{|\sigma_{12}^{c}|}$) [52]:

$$\frac{1}{S_{12}}\left(\sqrt{\sigma_{12}^2+\left(p_{12}^{(-)}\sigma_2\right)^2}+p_{12}^{(-)}\sigma_2\right)=1 \tag{3.3.9}$$

IFF Mode C ($\sigma_2<0$) and ($0\le\left|\frac{\sigma_{12}}{\sigma_2}\right|\le\frac{|\sigma_{12}^{c}|}{\sigma_{23}^{A}}$) [52]:

$$\left[\left(\frac{\sigma_{12}}{2\left(1+p_{23}^{(-)}\right)S_{12}}\right)^2+\left(\frac{\sigma_2}{Y_C}\right)^2\right]\frac{Y_C}{(-\sigma_2)}=1 \tag{3.3.10}$$

The parameters σ_{23}^{A}, σ_{12}^{C} and $p_{23}^{(-)}$ mentioned in the previous equations are defined as,

$$\begin{aligned}\sigma_{23}^{A}&=\frac{S_{12}}{2p_{12}^{(-)}}\left(\sqrt{1+2p_{12}^{(-)}\frac{Y_C}{S_{12}}}-1\right)\\ \sigma_{12}^{c}&=S_{12}\sqrt{1+2p_{23}^{(-)}}\\ p_{23}^{(-)}&=p_{12}^{(-)}\frac{\sigma_{23}^{A}}{S_{12}}\end{aligned} \tag{3.3.11}$$

Moreover, as it was mentioned by Zarouchas [52], Puck requires some empirical parameters. In particular, for UD carbon fiber material, $p_{12}^{(+)}=0.3$, $p_{12}^{(-)}=0.2$ and $m_\sigma=1.1$.

3.4 Design and optimization

3.4.1 Deisgn Guidelines

Before optimizing the laminate of the structure some basic design guidelines have to be followed. As specified by Kassapoglou et al. [45] in Chapter 12 of the book "Design and Analysis of Composite Structures", the basic guidelines when designing a composite laminate are the following,

- Laminates should be symmetric in order to reduce the bending/membrane coupling (the entire B matrix is zero).
- Laminates should also be balanced (for every $+\theta$ there should be a $-\theta$ in the laminate) in order to eliminate shear/stretching coupling ($A_{16}=A_{26}=0$).
- The 10% rule must always be followed. To elaborate, every laminate has to have at least 10% of the fibers aligned with the four principal directions, namely 0^o, -45^o, $+45^o$, 90^o. This gives the ability to the laminate to cope with secondary loads for which the laminate is not designed for, and prevent premature failure.
- The consecutive UD layers with the same orientation should be no more than 4. This rule is applied due to the fact that micro-cracks starting from one end of the stack travel to the other end without getting arrested.

- The stack of the same orientation layers should be interrupted by layers with orientation no more than 45^o. If the orientation of the layer is more than 45^o, the mismatch between the stiffness of the adjacent layers can initiate delaminations. Additionally, this interruption helps arrest matrix cracks.
- The 0^o plies should be positioned as far as possible from the middle plane in order to increase the bending stiffness of the laminate (entry D_{11} is increased).

These rules act as guidelines for designing an optimal laminate. To progress one step further and achieve the optimal laminate with respect to its failure load, the use of an optimization algorithm is imperative.

3.4.2 Optimization

Although an optimization algorithm is not in the scope of this thesis, it will be described in order to act as a guideline for future research topics. In particular, the optimization of a composite lug is distinguished into two categories. The first category implies the optimization of the lug with regard to its failure load. The higher the load, the stronger the lug for a specific failure mode. The second type of optimization refers to achieving a failure load which is almost the same for every mode of failure of the lug (net tension, shear-out, bearing). In this way, the laminate is not over-designed for a particular failure mode.

Regardless of the aim of optimization, there are some steps that need to be followed. For the optimization algorithm, the only parameter that can be altered is the orientation of the layers and their sequence. The geometry of the lug, for instance, the ratios w/D, e/D, and the thickness (total number of layers) should remain stable.

Optimization should be applied on a simple laminate with all 0^o degrees layers and a specific load. The stresses for this laminate are calculated, and the exact location and the mode of failure are established. As a next step, some of the 0^o degree plies are substituted by $\pm 45^o$ plies. The process is repeated and the failure load is again calculated. If the failure load is higher, the algorithm continues adding $\pm 45^o$. The process stops when the $\pm 45^o$ layers are 25% of the total laminate. It should be noted that an all 0^o layers laminate is expected to have a relatively low failure load due to the stress concentration around the hole. However, if the algorithm fails to find a layer sequence with a failure load higher than the 'all 0^o' laminate, it continues with the laminate with the second-highest failure load.

After this process, a laminate with 0^o and $\pm 45^o$ layers is obtained. However, it is important to implement the designing guidelines and specifically, the 10% rule. For this reason, some of the 0^o plies are substituted with 90^o plies. The algorithm stops when the 90^o has reached a 15% of the total laminate. The final laminate should have a ratio of 25% of $\pm 45^o$, 15% of 90^o,and 60% of 0^o layers.

At this point, it is worth justifying the layer percentage selection. Specifically, the high ratio of 0^o layers has to do with the fact that the lug is loaded in tension, and therefore more fibers are needed in the loading direction. The division of the percentages is considered appropriate given the fact that $\pm 45^o$ layers (25%) are more essential since they aid in better distributing the stresses around the hole. Finally, the percentage of 90^o layers is the lowest (15%) since these layers are placed in order to have fibers in all the principal directions of the laminate. A schematic of the optimization algorithm is depicted in Figure 3.9.

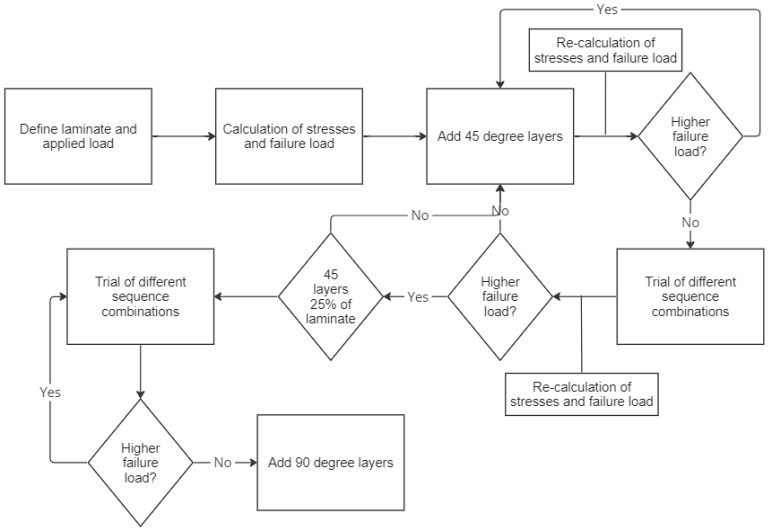

Figure 3.9: Optimization algorithm schematic.

3.4.3 Lug design

Having specified the design guidelines and the optimization technique, a laminate has to be designed in order to test the theory developed in this thesis topic. This laminate was utilized for developing the FEM model, but also for manufacturing the specimens for the tensile test. For the analytical solution, plenty of laminates were tested and compared with finite method results in order to ensure the accuracy of the method.

First of all, a thick laminate has to be developed in order to represent the actual lug geometry (lugs in the aerospace field have a thickness of $3-5mm$ [45]). For this reason, the appropriate choice would be a laminate with over 5 mm thickness. Given the fact that the average ply thickness of a UD ply is $0.13-0.18\,mm$, a 28-layer laminate was designed. By following all the design guidelines mentioned, the final laminate is,

$$laminate_{final} = [0_4/45/0/-45/0_2/45/0/-45/90_2]_s$$

It is worth mentioning that although this is the final laminate, there are many laminates with various combinations of layer orientation that adhere to the design guidelines.

Regarding the geometry of the lug, it is crucial to implement the observation of some authors from the literature. In particular, as pointed out by Chang et al. [33] the ratio of w/D should not be very low ($w/D \rightarrow 1$) due to the fact that the strength in tension decreases. Therefore, a ratio of $w/D = 2$ was selected. This selection is also substantiated by the research of Kassapoglou and Townsend [43] who also selected the same ratio.

Moreover, the length of the lug should not be very short, so that the stresses from the clamping do not influence the stresses around the hole. Hence a length of $L = 190\,mm$ was chosen. In the tensile tests conducted by Kassapoglou and Townsend [43], the same length was selected.

Concerning the edge distance ratio e/D, as pointed out by Chang et al. [33], the lower the ratio, the less the failure load. In order to have the hole concentric with the circular geometry of the lug, and given the fact that a $w/D = 2$ was selected, a ratio $e/D = 1$ was chosen. Furthermore, a second lug geometry was created with the same w/D ratio but with a lower edge distance ratio ($e/D = 0.8$). It is worth mentioning that the ratio of $e/D = 1$ was selected by some authors [43], [55] for conducting tensile tests for composite mechanically fastened joints.

3.5 Semi-analytical Approach

As a first step in validating the analytical approach, the stress equations in the polar coordinate system were checked. According to research([33], [22], [45]), the radial stress σ_r (3.2.15) at the top half of the circumference of the hole should be equal to the bearing stress ($\sigma_{bearing} = (2P)/(\pi ah) \cdot cos(\theta)$) (3.2.29). The graph of the two equations (3.2.15, 3.2.29) around the hole is depicted in Figure 3.10.

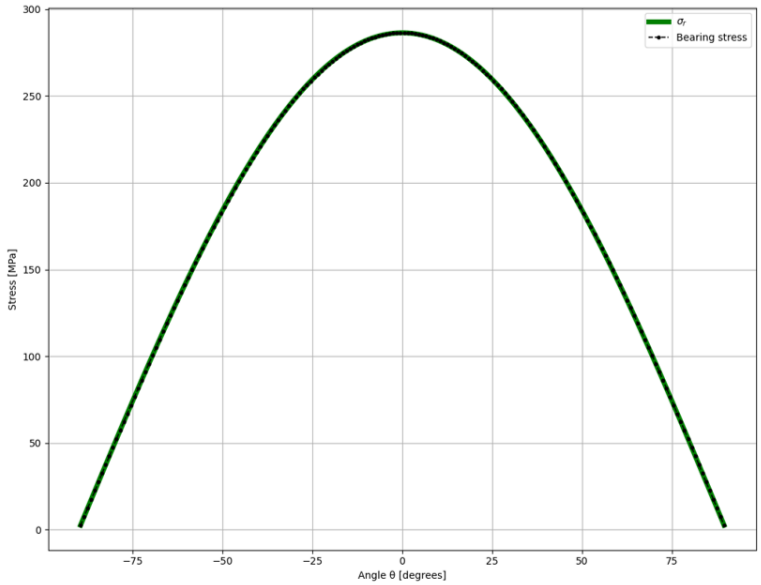

Figure 3.10: Bearing stress comparison with σ_r from analytical model.

It can be observed from the graph that the results are in accordance and hence the σ_r stress equation (3.2.14) is validated. Another point of validation is the shear stress $\tau_{r\theta}$ at the inner circumference of the hole. Since it is assumed that there is no friction between the pin and the part, the value of this term should be zero. Substituting the values and calculating the $\tau_{r\theta}$ around the hole from equation 3.2.16, the results are close to zero ($2e^{-12}$). Therefore, it is validated that the equation is correct.

Although equations 3.2.14, 3.2.16 are validated, it was noticed that the equation describing the σ_θ (3.2.15), produced results one magnitude higher than the radial stress σ_r. This is controversial with the results of Zhang and Ueng [22], who compared the normalized stress distribution for different laminates, and resulted in a σ_θ in the same magnitude with σ_r.

Even though a scrutinizing check of the method was performed, an error could not be spotted. By carefully, evaluating all the equations, it was noticed that the integration constant D influences significantly the distribution of the tangential stress σ_θ compared to the other constants. Therefore, since an error in the process could not be found, it was deemed appropriate to multiply the term containing the integration constant D with a factor ($\boldsymbol{f}$). The new equation for the tangential stress σ_θ is given by,

$$\sigma_\theta = \frac{1}{r^2}(\cos(\theta)F\beta(-1+\beta)r^{1-\beta} + \boldsymbol{f} \cdot kD(-1+k)r^{1-k} + \cos(\theta)E\beta(1+\beta)r^{1+\beta} + Ck(1+k)r^{1+k} + 2Br^2 + H\cos(\theta)r) \tag{3.5.1}$$

In order to determine the factor $\boldsymbol{f}$, a group of 10 laminates was created with stiffness in the loading direction ranging from $9GPa$ to $131GPa$. The stiffness of the laminate in the loading direction (E_x) is a very important design parameter, and hence it was chosen as the main variable for estimating the factor. Since the geometry of the lug influences the stress distribution around the hole

([31], [32], [33]), the factor was determined for two types of geometries, specifically for $w/D = 2$ and $w/D = 4$. More geometries with various geometric characteristic ratios (e.g., e/D) could have been evaluated, however, it would raise the number of cases to be assessed, and hence the overall duration of this thesis project.

The factor $\boldsymbol{f}$ was determined by comparing the stresses in a ply level (σ_1, σ_2, τ_{12}) from the semi-analytical approach with the stresses from a numerical model in Abaqus. Many iterations for every laminate were performed and every time the factor was adjusted until the results of the comparison reached a satisfactory level (the results of this comparison are presented in section 4.5.2).

The 10 laminates for the two geometries (20 cases to be evaluated in total), were created by implementing some of the design guidelines presented in 3.4.1. Specifically, adjacent layers do not have a change in the orientation greater than 45^o, no more than four consecutive plies of the same orientation (exceptions apply), and laminates are symmetric and balanced. Since the thickness of a composite lug is between $3-5mm$ (with an approximate layer thickness of $0.18mm$), 28-layer laminates were created. The laminates that were tested are presented in Table 3.1.

Table 3.1: Laminates for estimating the multiplication factor $\boldsymbol{f}$.

N	**Laminate**	E_x **[GPa]**
1	$[0,0,0,0,0,0,0,0,0,0,0,0,0,0]_s$	131.62
2	$[0,0,0,45,0,0,0,-45,0,0,0,45,0,-45]_s$	99.80
3	$[45,0,45,0,0,-45,0,-45,0,45,0,0,0,-45]_s$	83.4
4	$[45,45,45,0,-45,-45,-45,0,45,45,0,0,-45,-45]_s$	50.29
5	$[0,0,0,0,45,0,-45,0,0,45,0,-45,90,90]_s$	85.48
6	$[90,90,45,0,-45,0,0,0,45,90,90,-45,0,0]_s$	69.01
7	$[0,0,0,90,0,0,0,90,0,0,0,90,0,90]_s$	97.09
8	$[0,0,90,0,0,0,90,0,0,90,90,0,90,0,90]_s$	79.54
9	$[90,90,90,0,90,0,90,0,90,0,90,0,90,90]_s$	53.192
10	$[90,90,90,90,90,90,90,90,90,90,90,90,90,90]_s$	9.23

As it can be observed, the laminates are categorized into groups that have: only a combination of $0^o/45^o$ (2, 3, 4), those with $0^o/45^o/90^o$ (5, 6), those with $0^o/90^o$ (7, 8, 9), an all 0^o (1) and an all 90^o (10) laminate. The laminates were discretized in these categories in order to include various combinations of laminates with fibers in the four principal directions ($0^o, \pm 45^o, 90^o$) and hence make the approach of determining the factor more universal.

The result of this approach is a graph (different for every lug geometry) with the x-axis being the stiffness of the laminate in the loading direction (E_x) and the y-axis the multiplication factor $\boldsymbol{f}$. By obtaining the curve, the multiplication coefficient for laminates that are not included in the table 3.1 can be determined.

The curve is estimated as a polynomial regression of the points of every laminate. In order to determine the optimal degree of the polynomial function a statistical analysis was performed. In particular, as pointed out by Pakdemirli [56], the optimal degree in a polynomial regression is obtained when the standard regression error ($S_{y/x}$) is minimized. Particularly, the $S_{y/x}$ is defined by,

$$S_{y/x} = \sqrt{\frac{RSS}{N-(n+1)}} \tag{3.5.2}$$

With N being the total number of points (in this case, N is equal to the number of laminates $N = 10$), n the polynomial degree, and RSS the Residual Sum of Squares which is defined by,

$$RSS = \sum_{i=1}^{N} (y_i - f(x_i))^2$$
$$y_i : i^{th} \text{ value of the variable to be predicted}$$
$$f(x_i) : i^{th} \text{ predicted value of } y_i \tag{3.5.3}$$

The standard regression error ($S_{y/x}$) with respect to the degree of the polynomial equation for the two different geometries is presented in Figure 3.11.

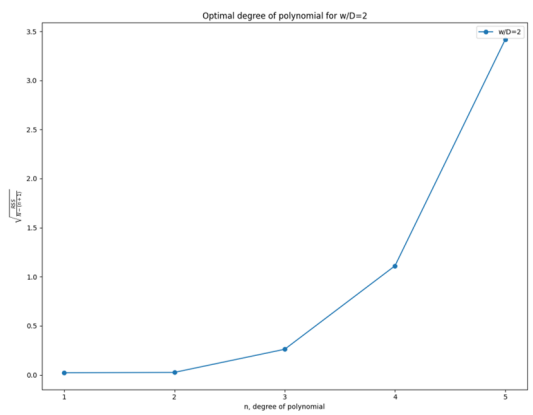

(a) $S_{y/x}$ versus the polynomial degree for $w/D = 2$.

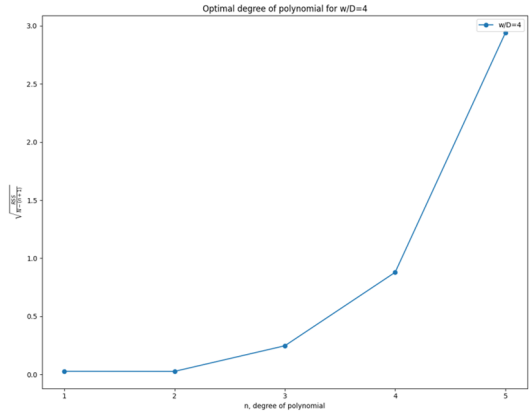

(b) $S_{y/x}$ versus the polynomial degree for $w/D = 4$.

Figure 3.11: Standard regression error as a function of the polynomial degree for the two different geometries.

As it can be observed from the graphs, the standard regression error is minimized for a second degree in both geometries. Therefore, the data are better fitted with a second-degree polynomial equation. For every geometry, the fitted curves with the data are presented in Figure 3.12.

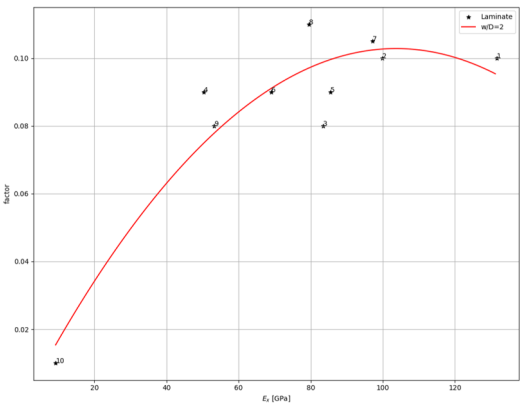

(a) Fitted factor curve for $w/D = 2$.

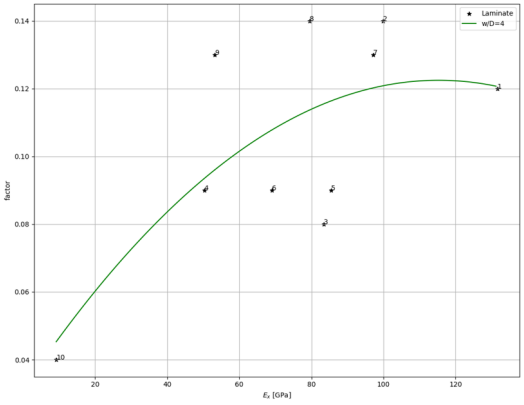

(b) Fitted factor curve for $w/D = 4$.

Figure 3.12: Fitted second-degree polynomial curves for the two geometries.

For the geometry $w/D = 2$, the equation that predicts the factor based on the laminate's E_x is,

$$y = -0.00001 \cdot x^2 + 0.00203 \cdot x - 0.00260 \tag{3.5.4}$$

For the geometry $w/D = 4$, the equation is,

$$y = -0.00001 \cdot x^2 + 0.00158 \cdot x + 0.03129 \tag{3.5.5}$$

These polynomial curves act as a guideline for determining the factor for laminates with similar geometries in the same range of E_x. The curves are depicted in a common graph in Figure 3.13.

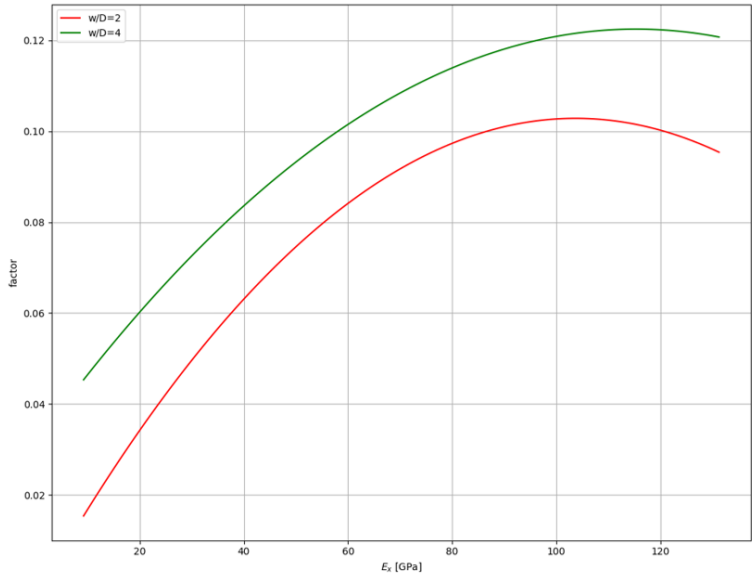

Figure 3.13: Polynomial fitting curves for geometries $w/D = 2$, $w/D = 4$.

Finally, comparing the principal stresses of the semi-analytical approach around the hole presented good proximity with the results of the numerical simulation. It is worth noting that the results were concurrent with the conclusion of the research of York et al. [32]. Specifically, the w/D did not influence the stress distribution, however, it affected the magnitude of the stresses. The results of the comparison are presented in 4.5.2.

CHAPTER 4

Numerical Simulations

Chapter 4 entails information about the process followed for developing the numerical models. In this chapter, the boundary conditions, the geometry, and the materials utilized for modeling the lug will be described. Furthermore, a new numerical model will be developed in order to reduce the solving time. Finally, the results of the numerical model will be used to validate the results of the semi-analytical approach presented in the previous chapter.

4.1 Simulation set-up and parameters

For simulating a composite lug under tension, the Finite Element Method (FEM) was utilized. All the simulations were performed in the Abaqus software, which is a numerical simulation tool for modeling structures with various geometries and materials including composites. The creation of a numerical model entails specific steps. Particularly, the first step is the creation of the geometry of the component under investigation and its discretization in elements, and the next step is the assignment of the material. Lastly, loads and restraints are applied to the model in order to simulate the actual loading conditions of the component.

4.1.1 Geometry

There are two types of geometries that can be created in the simulation software. There are the 3-D and the 2-D geometries. The semi-analytical approach developed in this research project focuses mainly on describing the in-plane phenomena on the lug (e.g., stresses and strains) and hence, a 2-D geometry was selected. A 3-D geometry would have been ideal for studying the out-of-plane stresses and strains.

As was discussed in the Literature Review (Figure 2.6), the important geometric characteristics of a lug are the ratio of width over its hole diameter (w/D) and the ratio of the edge distance over the hole diameter (e/D). These characteristics have a crucial influence on the failure mode of the lug. Moreover, the length of the lug is selected based on lug geometries used in previous research.

The geometry that was modeled is based on the research of Kassapoglou and Townsted [43] (see 3.4.3). Specifically, a ratio of $w/D = 2$ and $e/D = 1$ was selected, and a length of $L = 190mm$. Additionally, a second geometry was tested with different geometric characteristics but with approximately similar ratios ($w/D = 2$ and $e/D = 0.8$) and length ($L = 190mm$). The second geometry was selected as a means to observe how the differences in the geometry influence the stress distribution, failure load, and failure mode of the composite lug. The designs are depicted in Figure 4.1.

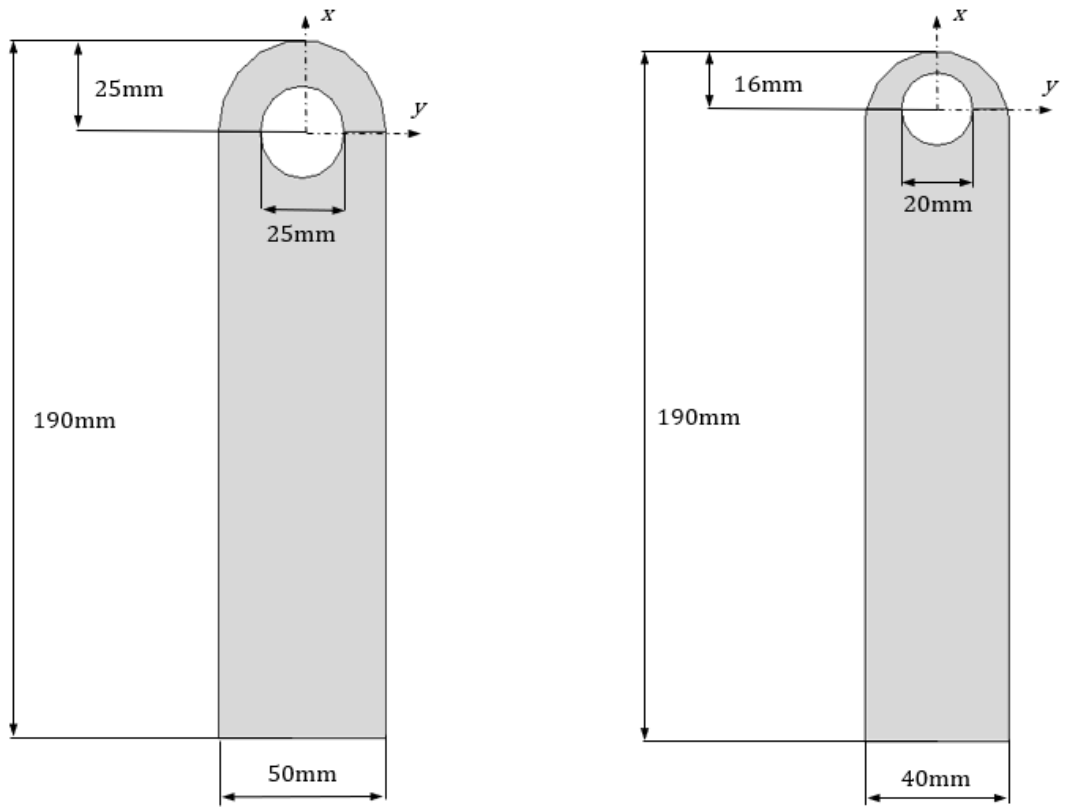

(a) Design 1: $w/D = 2$, $e/D = 1$.

(b) Design 2: $w/D = 2$, $e/D = 0.8$.

Figure 4.1: Geometric characteristics of the two designs that were studied.

4.1.2 Element type

Modeling of a composite component in a numerical simulation software can be performed with the use of either shell or solid elements. For the composite lug that is studied in this research topic, shell elements were utilized. The selection of this type of element is substantiated by the fact that the main focus of this research is studying the in-plane stresses and strains.

In particular, the lug geometry was modeled with fully integrated, conventional shell elements (Element type: S4). As described in the Abaqus manual [57], full integration elements are useful for models with local stress concentrations that are not subjected to bending loads. Since the lug is subjected only to tensile loads, and stress concentration is expected around the hole, this type of element was considered ideal.

Another important characteristic of the mesh of the model is the number of elements. In order to acquire the optimal element length a trade study was conducted. The converge criterion was the maximum in-plane principal stress. This choice is supported by the fact that maximum stress is the main reason for failure, and hence knowing its exact value is very crucial.

In the beginning, a large element length is selected and then it is decreased at a standard pace (dividing the element length in half in every iteration) in order to be able to compare the results. A mesh is considered converged when its values are within 5% of the values of the most refined mesh. The convergence study is depicted in Figure 4.2.

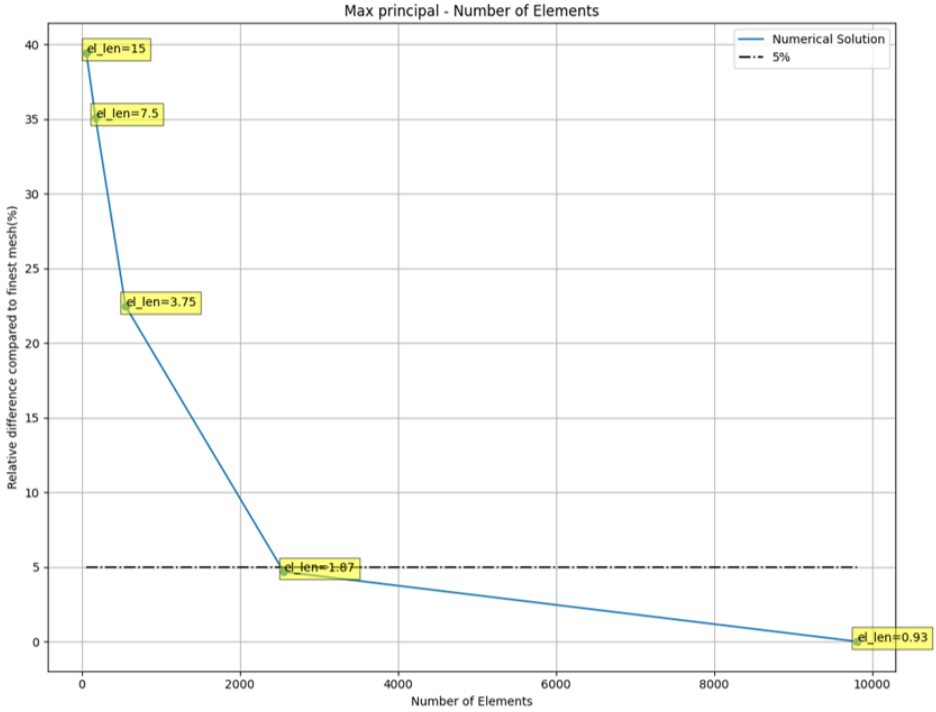

Figure 4.2: Convergence study for the element length.

It can be observed that the optimal element length is $1.87mm$, which results in a lug with a total number of elements equal to 2555. Selecting the finest mesh would not aid significantly in the accuracy of the model however, it would increase the processing time.

4.1.3 Material model

The material that was utilized in the simulations was the HexPly AS4 8552 Uni-directional carbon fiber prepreg tape, manufactured by Hexcel. The same material was later used for the manufacturing of the lug specimens for the tensile tests. The material properties are presented in Table 4.1 [58].

Table 4.1: Material properties.

Hexply AS4 8552		
Property	**Value**	**Unit**
E_1	131.62	GPa
E_2	9.23	GPa
G_{12}	4.813	GPa
v_{12}	0.302	-
t	0.187	mm
X_t	2063.04	MPa
X_c	1484.37	MPa
Y_t	63.91	MPa
Y_c	268.55	MPa
S_{12}	91.56	MPa

For modeling the material in Abaqus, a conventional shell approach was used. Another important step in laminate creation is establishing the correct fiber orientation. Specifically, a coordinate system is created, with the x direction aligned with the load. In addition, every layer orientation is

given with respect to the created coordinate system. An example of how the principal axis (1: fiber, 2: matrix) are oriented for a 45^o layer is depicted in Figure 4.3.

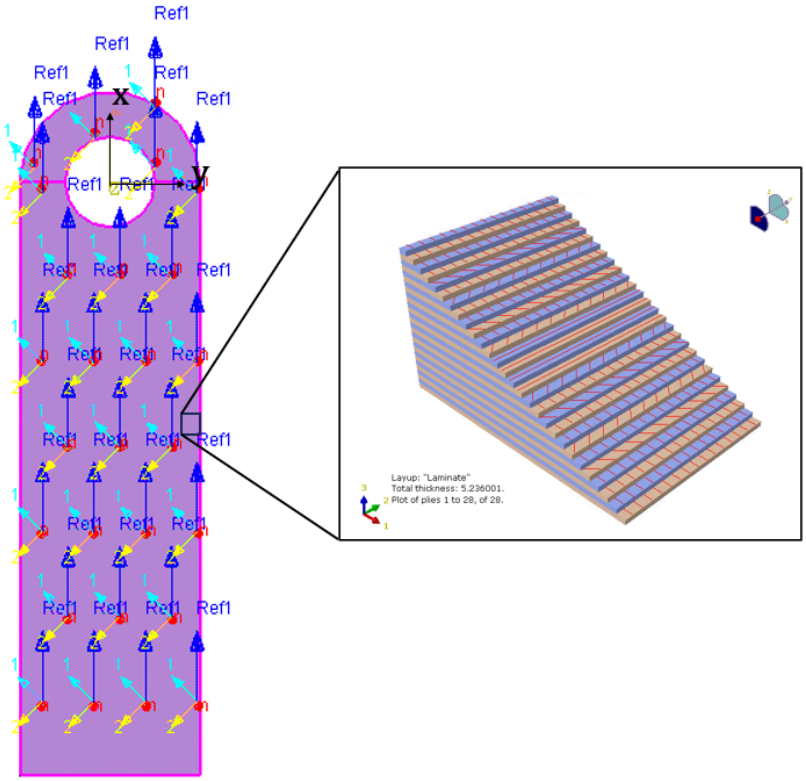

Figure 4.3: Layer orientation in the FEM model.

4.2 Lug model

The primary aim of the FEM simulation is to obtain the stress field around the hole of the lug, in the plane of loading. Therefore, a static analysis was performed. The output of this analysis are the stresses in the principal direction of every layer, which were used for validating the semi-analytical approach of this research topic. Moreover, a first-ply failure criterion (4.3) was applied in order to determine the mode of failure of the composite lug.

4.2.1 Boundary conditions

In order to compare the stress results of the two methods, it is of crucial importance to have the same boundary conditions. Since the load in the semi-analytical approach is applied as cosine distribution, the same approach was used in the FEM model.

Particularly, a shell edge load was applied at the circumference of the upper part of the hole. The value of the shell edge load was defined as a constant (C) multiplied by a trigonometric function ($q_{shell-edge-load} = C \cdot cos(\theta)$). As specified in the semi-analytical approach in Chapter 3, the constant was set equal to the magnitude of the load per unit length q (3.2.28) and therefore $C = 2P/\pi a$, with P being a load (N) and a (mm) the radius of the hole. Furthermore, the lug geometry is restrained in all degrees of freedom at the bottom edge. A schematic of the boundary conditions can be observed in Figure 4.4.

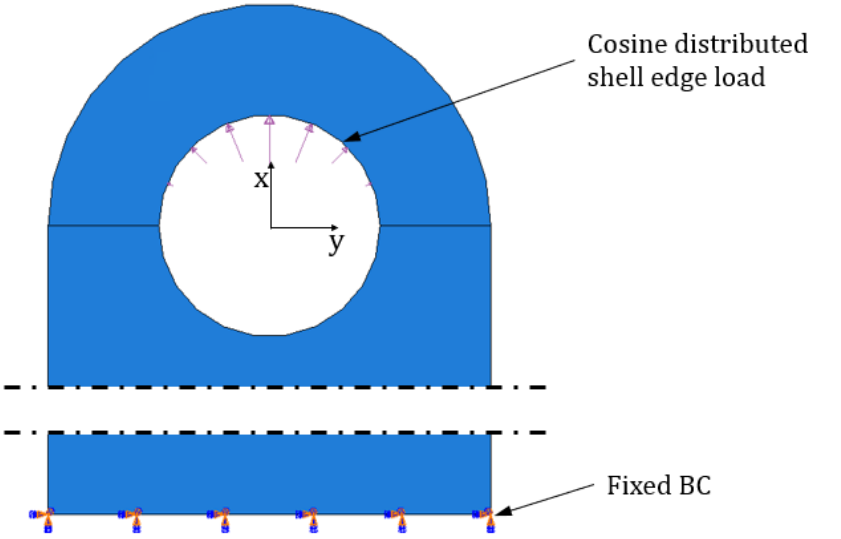

Figure 4.4: Boundary conditions of the FEM model.

4.2.2 Lug stress distribution

The last step of the processing is running the model to the solver and acquiring the results. Particularly, the output of the analysis is the stresses and strains in each ply of the laminate. The stresses in each layer are projected in the principal direction of the layer, specifically direction 1 which corresponds to the fiber direction, and direction 2 which corresponds to the direction perpendicular to the fibers (matrix). An example of how the principal stresses are distributed in the first layer (0^o) of Design 1 ($w/D = 2, e/D = 1$) for laminate $[0_4/45/0/-45/0_2/45/0/-45/90_2]_s$ is depicted in Figure 4.5.

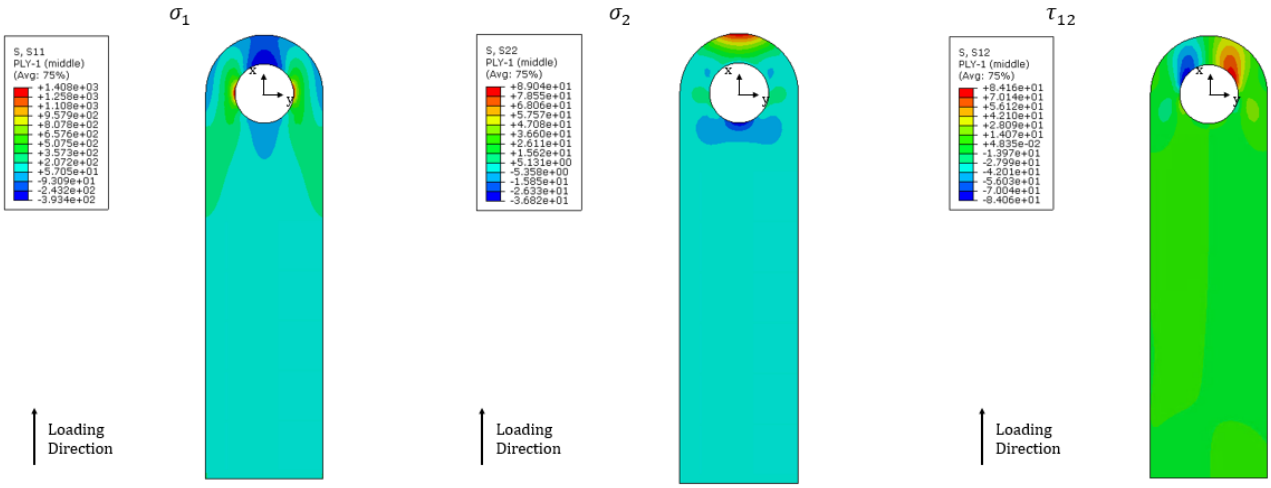

Figure 4.5: Principal stresses on the 0^o layer in the FEM model.

It is worth noting that the distribution of the principal stresses is affected by the fiber orientation. After acquiring the stress distribution for each ply, the following step is to apply a first-ply-failure criterion in order to detect which ply is failing first, and how the failure progresses in each layer.

4.3 First Ply Failure

As was described in section 3.3.1, there are many failure criteria in the composite material field, however, Abaqus offers only 5 in-plane failure criteria. It is worth mentioning that these criteria are

used only as a means of detecting failure, and no degradation of the material properties is applied after failure is detected [57].

These five criteria are distinguished in stress-based and strain-based failure theories. In the first category, failure criteria such as the Maximum Stress, Tsai-Hill, Tsai-Wu, and Azzi-Tsai are included. For the strain-based failure theories, only the Maximum Strain criterion is included. In a trade study presented in the manual of the numerical simulation software, it was concluded that the Tsai-Hill is the most conservative of the ones provided [57]. Moreover, it is one of the simplest to implement since it requires only the strength of the material.

By inserting the strength of the material in tension (X_t, Y_T) compression (X_c, Y_c) and shear (S_{12}), the failure value R is calculated. This variable has positive values, and it is lower than one ($R < 1$) when for the given loading case, failure does not occur. If the value of R is greater than one ($R \geq 1$) then failure is implied.

Applying the Tsai-Hill failure criterion, on the lug with the $[0_4/45/0/-45/0_2/45/0/-45/90_2]_s$ laminate, it can be observed that for a given load, failure occurs firstly in the 90^o layers in the middle of the laminate as can be observed from Figure 4.6.

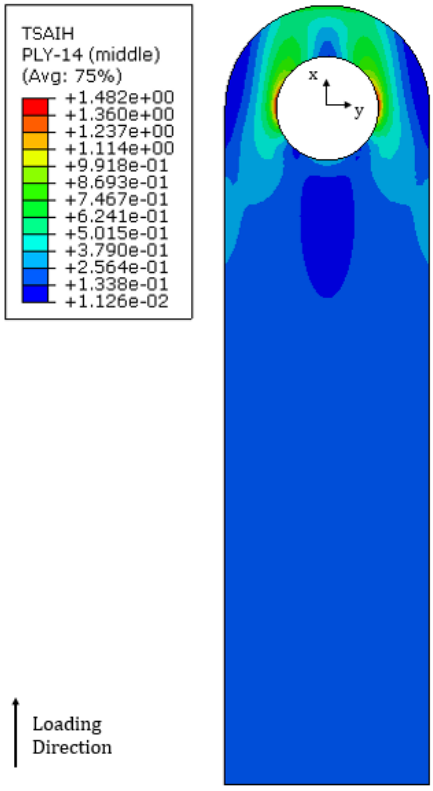

Figure 4.6: First Ply Failure on the 90^o layer in the FEM model.

It can be noticed that for the 90^o layer, failure occurs at the edge of the hole ($R > 1$) and specifically on the left and right side. Moreover, it is observed that the failure follows an upward path. Hence, it can be assumed that in a case of a higher load, failure would occur along the path depicted with green color in the previous image. According to Chang et al. [33], this resembles a shear-out type of failure. The failure mode prediction will be described thoroughly in Chapter 6.

4.4 Half circle spring model

In some applications, in an aircraft, lugs can have a larger width and length than the one modeled in this research topic. Analysing a larger lug would increase the total number of elements and hence the overall processing time. In addition, the semi-analytical stress results could have deviated from the results of the lug, due to the difference in the geometry. For all these reasons, it was deemed appropriate to create a model that would have the same geometry as the one modeled in the semi-analytical approach, give nearly the same results as the full lug model and at the same time be more efficient (in terms of element number and processing time) in analyzing large lugs.

The new model is called *'Half Circle Spring model'* and is a combination of a semi-circular geometry with springs attached at the edges. The springs are attached at the bottom side of the geometry, and their stiffness value is calculated so that it matches the stiffness of the elements to which they are attached. The springs were added in order to approach the response of the lug geometry in a tensile load applied in the hole. The geometry of the model is depicted in Figure 4.7.

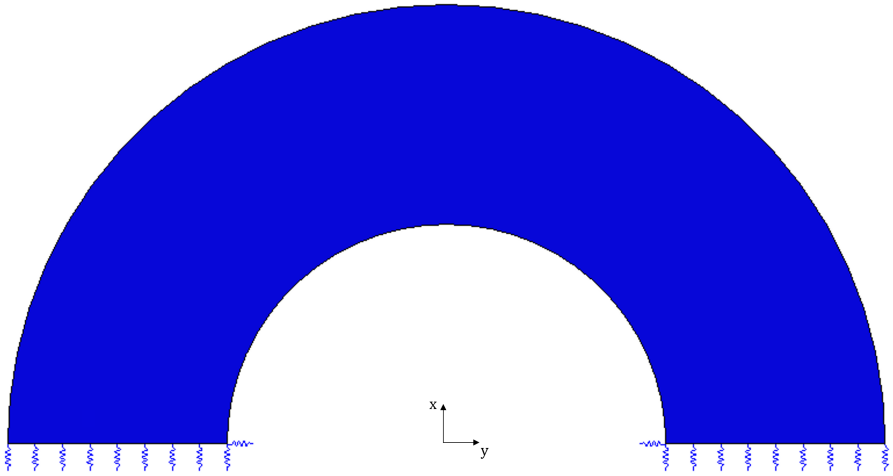

Figure 4.7: Half Circle Spring model.

The same modeling approach with the lug was followed in this model. Specifically, plane stress conventional elements (S4) were used, with an element length of $1.87mm$. It is worth noting that the total number of elements is 240, which translates to 90% element reduction compared to the full lug model.

4.4.1 Spring constant calculation

In order to define the springs two points are needed. The first point is positioned at a distance of one element length exactly opposite from the edge. The second point is the element node on the edge of the geometry. To perfectly define the spring, the next step is to calculate its stiffness $K[Force/Length]$. The value is given by the equation,

$$K = \frac{E \cdot A}{l} \tag{4.4.1}$$

Where E is the stiffness of the laminate in the direction of the spring (for the bottom edge E_x), A is the cross-sectional area of the element ($A_{el} = x \cdot h$) and l is the length of the element in the direction of the springs. In addition, in order to simulate the resistance of the pin inside a hole, a spring was placed inside the hole, perpendicular to the applied load. The position of the springs and an approximation of their stiffness is observed in Figure 4.8.

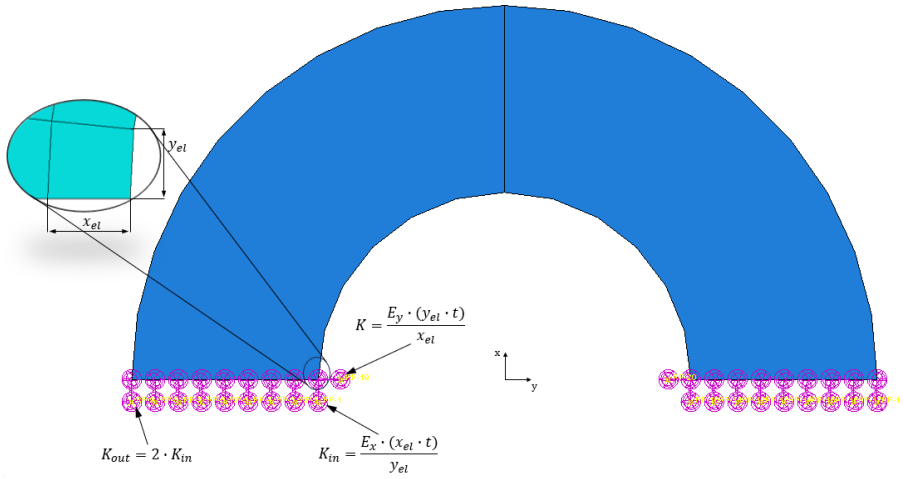

Figure 4.8: Spring stiffness calculation.

During the simulation of the lug, it was noticed that the outer side is stiffer than the side of the hole (the displacement of the nodes perpendicularly to the force on each side where measured, and the inside node has a larger displacement). In order to account for this in the Half Circle model, it was decided that the stiffness of the spring would vary across the edge. Specifically, the stiffness of the spring in the hole would be calculated with the expression 4.4.1, and the spring at the outside would have a stiffness which would be a factor/multiplier times the stiffness of the inner spring ($K_{out} = factor \cdot K_{in}$).

In order to determine this factor a convergence study was conducted. The criterion of comparison was the maximum principal in-plane stress (at the elements on the edge), which is the most crucial for predicting failure. The results were compared with the maximum in-plane stress of the lug model. The factor would start from a very high value and would decrease exponentially. When the results between the two models would have a difference lower than 20% (percentage assumed as a fair comparison between the models), the optimal factor was specified. The results of the convergence study are presented in Figure 4.9.

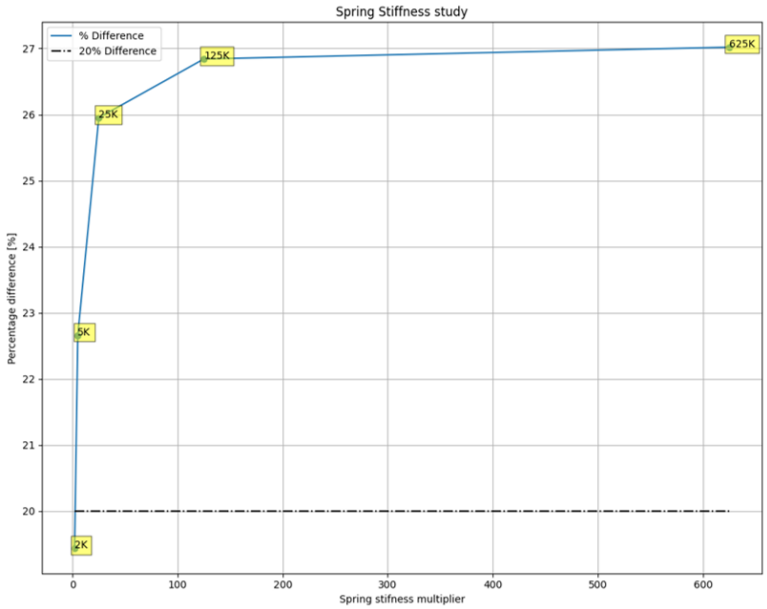

Figure 4.9: Convergence study for obtaining the spring stiffness multiplier.

The outcome of this study is a factor equal to two ($factor = 2$). The values of the stiffness for the springs between these two points are calculated by using a linear equation between the extreme values.

4.4.2 Boundary conditions

Boundary conditions are applied on one of the nodes of the springs, and the geometry of the model. Specifically, one node of the springs (Figure 4.10) is fixed in all degrees of freedom, so that it does not move in any direction. On the geometry, one node on each side is pinned, in order to match the conditions applied in the analytical model. Finally, a constraint is placed on a node at the top side of the geometry, in order to restrain the movement of the model in the 3-D space. Regarding the loading condition, a cosine distributed shell edge load is applied with the same magnitude as in the case of the lug and the analytical model. A summary of the boundary conditions on the model is depicted in Figure 4.10.

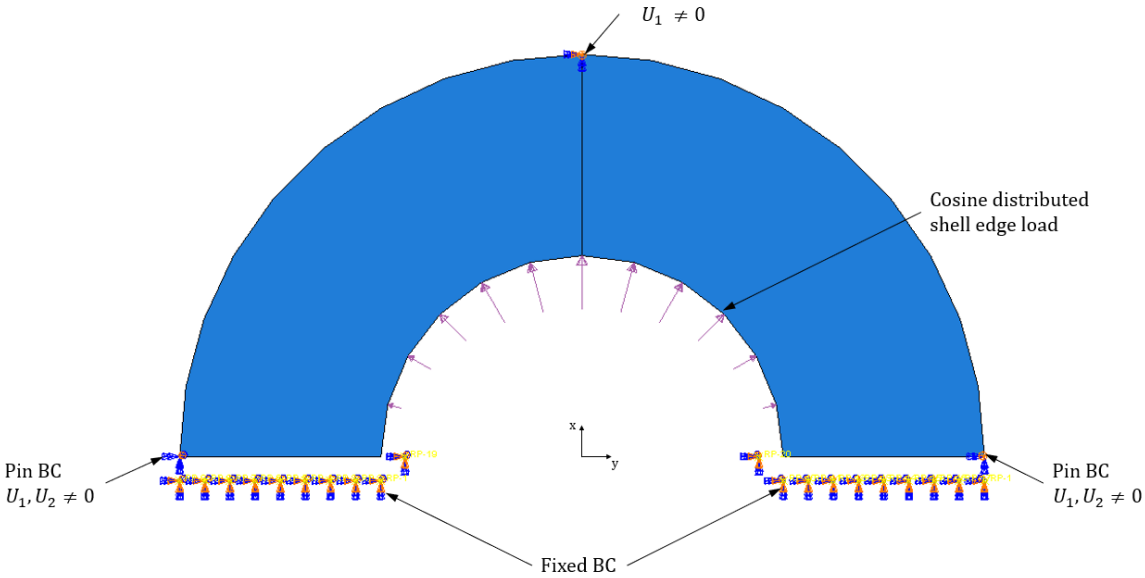

Figure 4.10: Boundary conditions of the half circle spring model.

As in the lug model, a simple static analysis is run. In order to validate this approach, the principal stresses are going to be compared in three regions in various layers of the laminate. Finally, the stress distribution of the principal stresses between the two numerical approaches is going to be compared.

4.5 Results

4.5.1 Numerical models comparison

In order to validate the half circle spring numerical model, a comparison with the lug approach was made. Specifically, this comparison entails the stress distribution (principal stresses contour plots) between the two models, and their principal stresses in three key regions. These regions include the elements where the springs are attached (Region 1), the elements on a line at the top part of the circle (Region 2), and the elements around the circle (Region 3). Reporting all the stress components of all the layers in every region would make this research report difficult to follow. Hence, the stress components and distribution are going to be presented in arbitrary layers (for validating the model all cases were processed and compared).

In particular, for Region 1, the stress distribution of the principal stress in the fiber direction (σ_1) in the 0^o layer is presented in Figure 4.11.

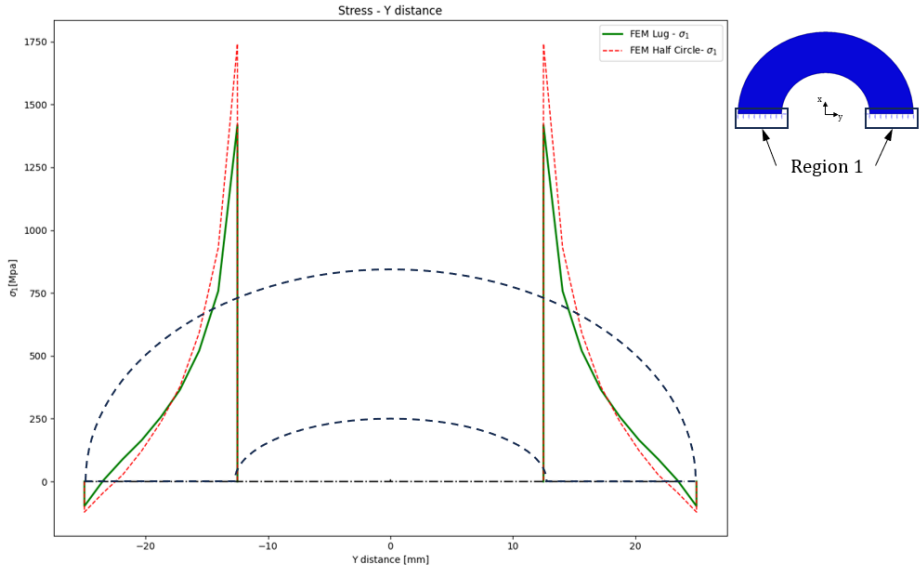

Figure 4.11: σ_1 in the 0^o layer across Region 1.

It can be observed from the graph, that the stresses from the two models are in accordance. The highest difference is at the edge of the hole, where the maximum stress concentration is observed. However, the difference between the principal stresses of the two models is approximately 20%. The same principal stress (σ_1) comparison in the is 0^o layer for Region 2, is presented in Figure 4.12.

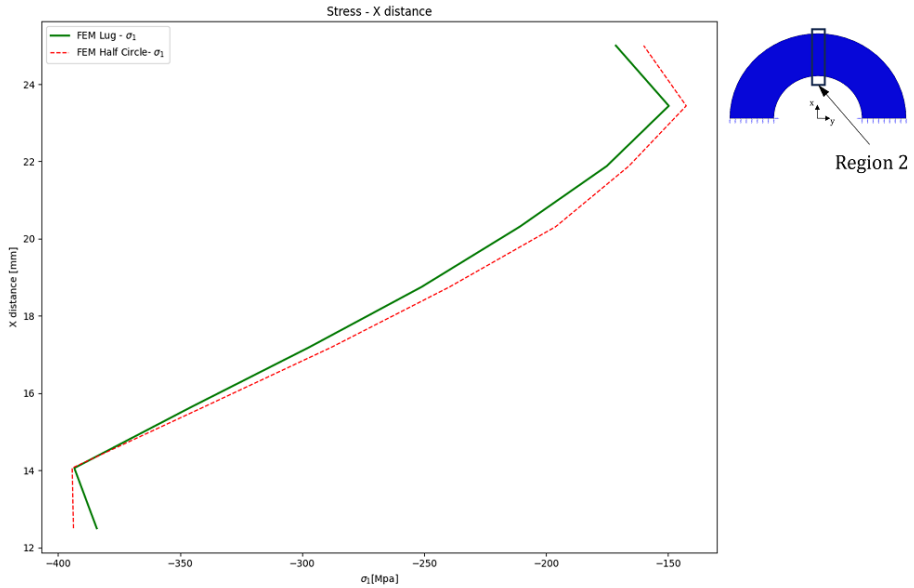

Figure 4.12: σ_1 in the 0^o layer across Region 2.

In this comparison, the highest difference between the two models is around 7%. Therefore, the stresses in Region 2 are in good accordance. Furthermore, the stress distribution around the hole (Region 3) is very important. In order to present more data that would increase the validity of this model, all the principal stress components were evaluated for Region 3. However, the comparison is made for the 45^o layer of the laminate. The results are depicted in Figure 4.13.

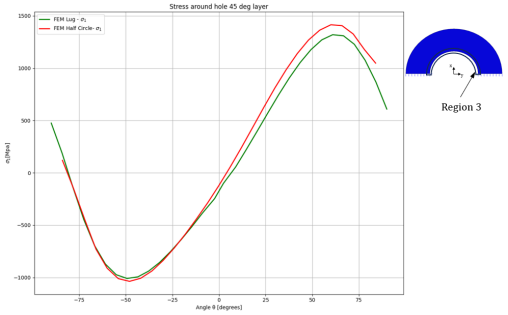

(a) σ_1 in the 45^o layer across Region 3.

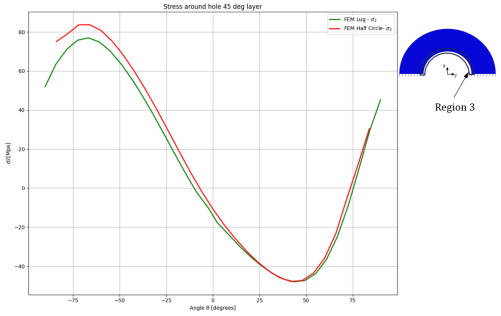

(b) σ_2 in the 45^o layer across Region 3.

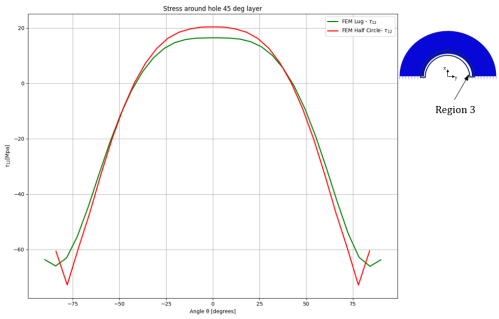

(c) τ_{12} in the 45^o layer across Region 3.

Figure 4.13: Principal stress components in the 45^o layer across Region 3.

From the results, it can be concluded that the principal stress components for the 45^o layer are in good proximity. The maximum difference is observed for the stress component τ_{12}, at an angle of 84^o (19%). It is worth mentioning that the results of the half circle spring model are plotted from -84^o to 84^o (instead of -90^o to 90^o). This choice is derived from the fact that the presence of two springs attached to one element node at $\pm 90^o$, increases the stiffness of that element. This leads to an increase in the stress calculated in the particular element (see figure 4.11), hence making this approach more conservative.

Having already compared the stresses in every region for the 0^o and 45^o, the last step was to compare the stress distribution in the 90^o layer. In this case, the comparison is made with the use of contour plots in order to better represent the stress distribution. The stress distribution on the 90^o layer of the lug is depicted in Figure 4.14.

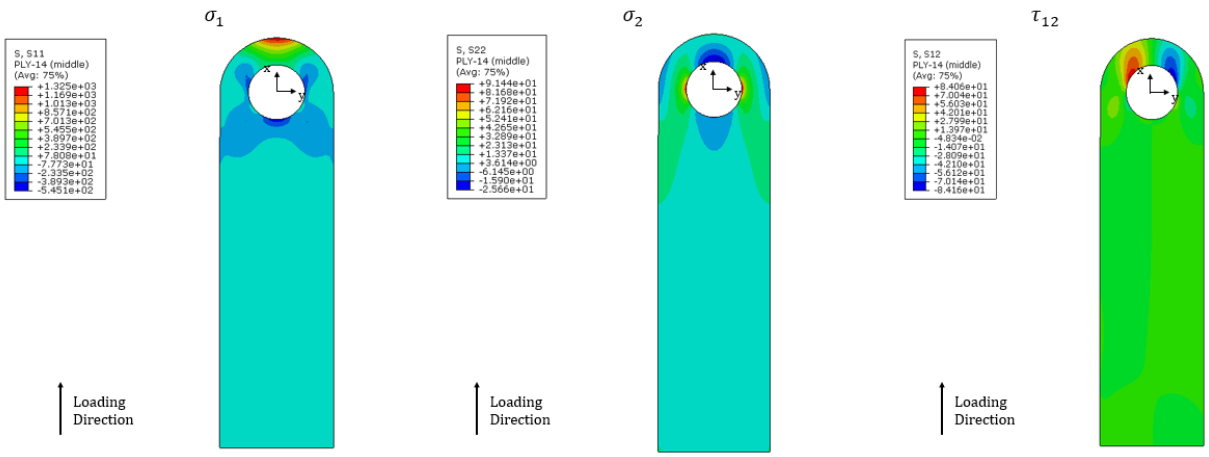

Figure 4.14: Principal stresses on the 90^o layer in the lug model.

The principal stress distribution (σ_1, σ_2, τ_{12}) on the 90^o layer of the half circle spring model is depicted in Figure 4.15.

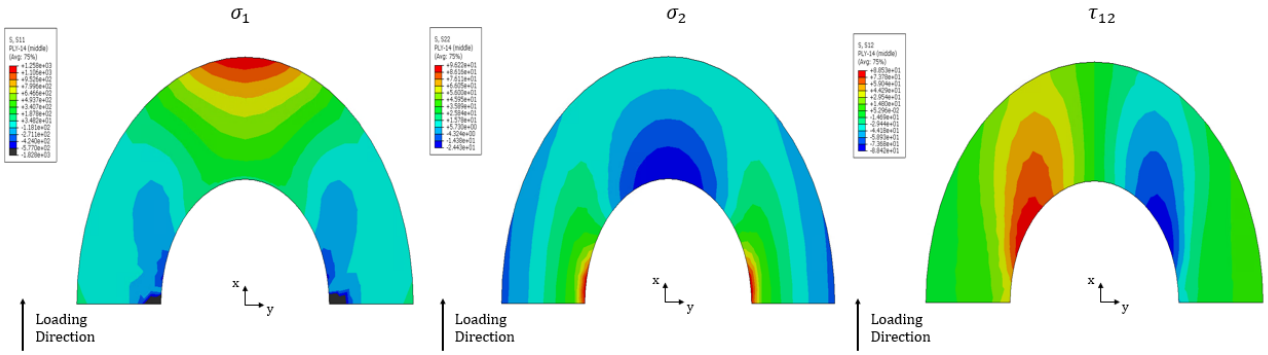

Figure 4.15: Principal stresses on the 90^o layer in the half circle spring model.

The stress distribution between the two models is concurrent. The discrepancy in the σ_1 stress of the half circle spring model is attributed to the fact that the specific element in the corner has two springs attached to a single node (increasing the stiffness of the element). If this value is to be considered very conservative and ignored, the maximum difference between the two models is approximately at 22% (regarding the stress component σ_1).

In conclusion, the half circle spring model gives a satisfactory approximation of the stress distribution compared with the full lug model. This approach can be utilized for obtaining quick estimates for the margin of safety of a lug, and when the design is finalized a detailed FE model of the entire lug geometry can be made.

Moreover, observing the stress distribution in figures 4.14 and 4.15, it could be concluded that the half circle spring model approach substantiates the initial assumption of this thesis that the most critical part of the lug is around the hole and hence it can be approached by a curved beam approximation. Finally, this approach concluded that a 90% reduction in the total element number, results in a maximum of 22% difference in the stress results. For large lugs, this approach could be proven valuable and reduce the processing time of the analysis.

4.5.2 Semi-analytical method evaluation

In order to determine the validity of the semi-analytical approach, the principal stresses (σ_1, σ_2, τ_{12}) in every layer at the circumference of the hole were compared with the results from the numerical simulation (full lug model, half circle spring model).

A crucial parameter in the semi-analytical approach is the multiplication factor which is presented in section 4.3. Particularly, for every laminate the factor $\boldsymbol{f}$ was determined by trying to approach (at the highest possible degree) the results of the semi-analytical method to the results obtained through the numerical simulations. Although this methodology was tested for a variety of laminates (see Table 3.1) and two geometries ($w/D = 2$, $w/D = 4$), for reporting reasons, only the results of the $[0_4/45/0/-45/0_2/45/0/-45/90_2]_s$ are presented for the geometry $w/D = 2$.

A comparison of the principal stress distribution between the two numerical models (lug, half-circle spring) and the semi-analytical method, for the 0^o, 45^o, 90^o layers, is depicted in Figure 4.16, Figure 4.17 and Figure 4.18 respectively. The lug numerical model is represented by the green curve, the half-circle spring model with the red, and the semi-analytical approach with the black.

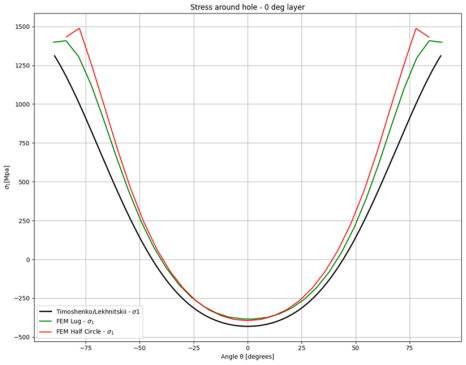

(a) σ_1 in the 0^o layer on lug with $w/D = 2$.

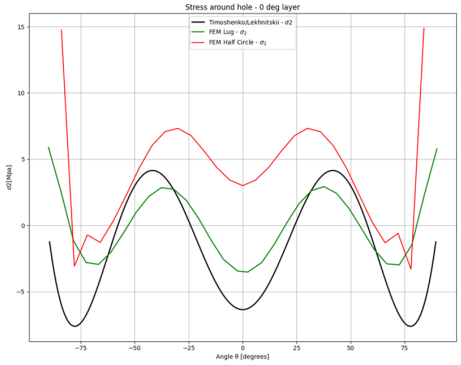

(b) σ_2 in the 0^o layer on lug with $w/D = 2$.

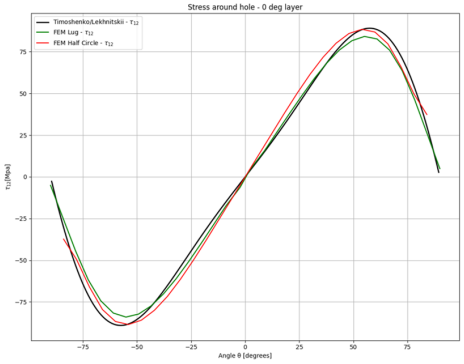

(c) τ_{12} in the 0^o layer on lug with $w/D = 2$.

Figure 4.16: Principal stress components in the 0^o layer on lug with $w/D = 2$.

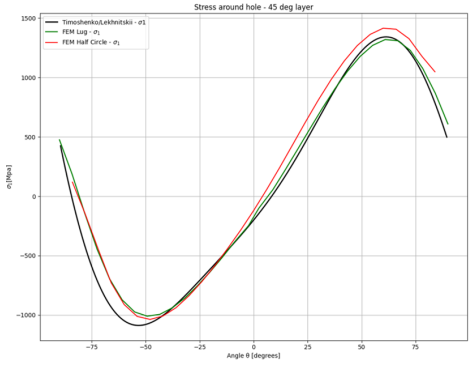

(a) σ_1 in the 45^o layer on lug with $w/D = 2$.

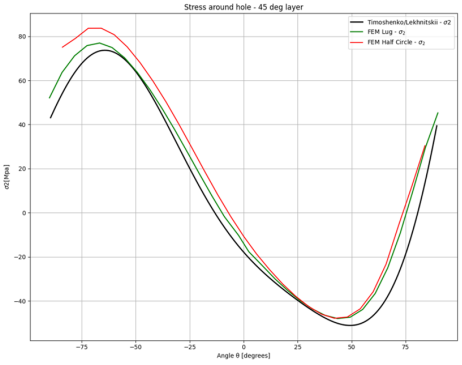

(b) σ_2 in the 45^o layer on lug with $w/D = 2$.

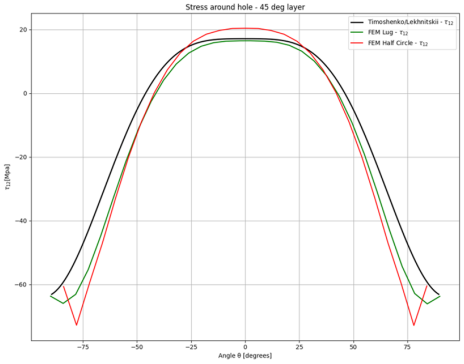

(c) τ_{12} in the 45^o layer on lug with $w/D = 2$.

Figure 4.17: Principal stress components in the 45^o layer on lug with $w/D = 2$.

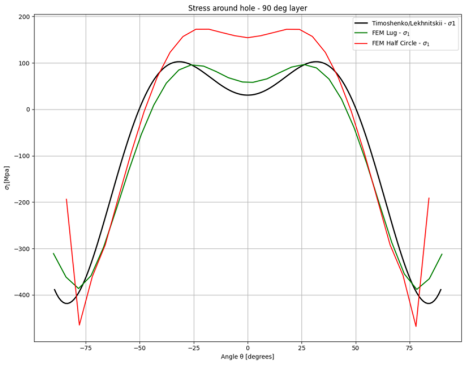

(a) σ_1 in the 90^o layer on lug with $w/D = 2$.

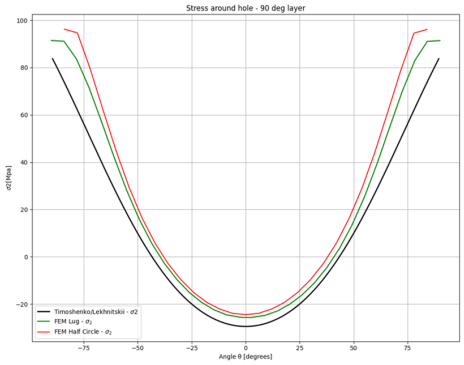

(b) σ_2 in the 90^o layer on lug with $w/D = 2$.

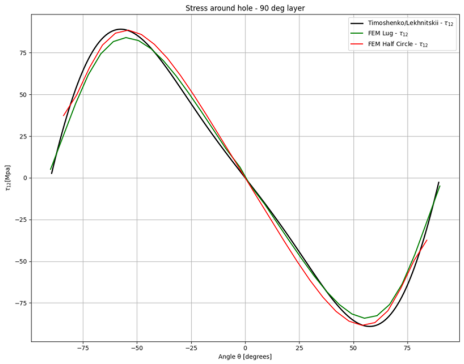

(c) τ_{12} in the 90^o layer on lug with $w/D = 2$.

Figure 4.18: Principal stress components in the 90^o layer on lug with $w/D = 2$.

The results of the comparison for every layer are encouraging. In particular, the difference between the semi-analytical and the full lug numerical model varies between 1% to 19% for the largest portion around the hole. However, there are some cases (e.g., σ_2 in the 0^o) where the stresses have a difference of 44%. Given the fact that this difference refers to areas where the stresses are not critical (in the magnitude of $0 - 20MPa$), the approach is considered promising. One last step of the validation of the semi-analytical approach is to verify that the polynomial curves that estimate the multiplication factor work for laminates different from the ones presented in Table 3.1.

In order to test the accuracy of the polynomial curves (3.5.4, 3.5.5) for the prediction of multiplication factor from the semi-analytical approach, two new laminates were created and evaluated for both geometries. One laminate with relatively low E_x and one with high. The two new laminates are presented in Table 4.2.

Table 4.2: Laminates for accessing the multiplication factor's f equations.

N	**Laminate**	**Ex [GPa]**
1	$[0, 45, 90, 90, 90, 90, -45, 90, 90, 90, 45, 0, -45, 90]_s$	34.73
2	$[0, 0, 0, 45, 0, -45, 0, 0, 0, 0, 45, 90, -45, 0]_s$	93.17

Substituting the E_x of the laminates in the polynomial equations 3.5.4 and 3.5.5 the multiplication factors are obtained ($w/D = 2 \rightarrow f_1 = 0.06/f_2 = 0.12$, $w/D = 4 \rightarrow f_1 = 0.08/f_2 = 0.11$). Substituting the relevant factor in 3.5.1 and following the methodology of the semi-analytical approach, the principal stresses on the layers of the laminate can be determined. The principal stress distribution of the first layer for laminate 1 with $E_x = 34.73GPa$ is illustrated for geometry $w/D = 2$ in Figure 4.19. The same distribution for the second laminate $E_x = 93.17GPa$ for the geometry $w/D = 4$ is depicted in Figure 4.20.

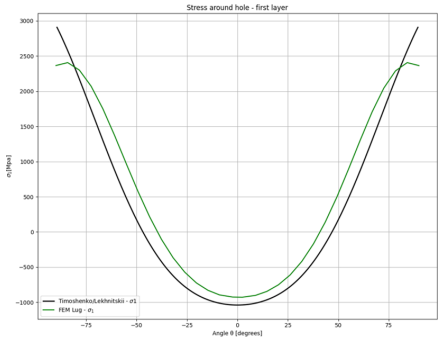

(a) σ_1 in the 0^o layer on lug with $w/D = 2$.

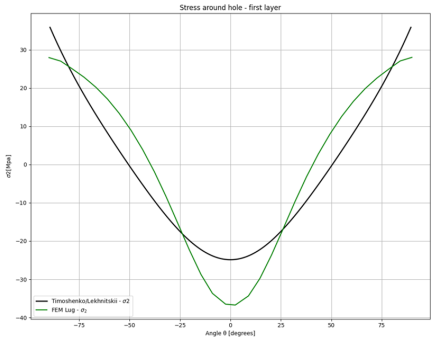

(b) σ_2 in the 0^o layer on lug with $w/D = 2$.

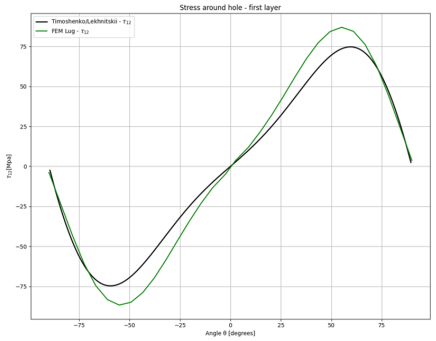

(c) τ_{12} in the 0^o layer on lug with $w/D = 2$.

Figure 4.19: Stress components in the 0^o layer on lug with $w/D = 2$ for laminate $E_x = 34.73GPa$.

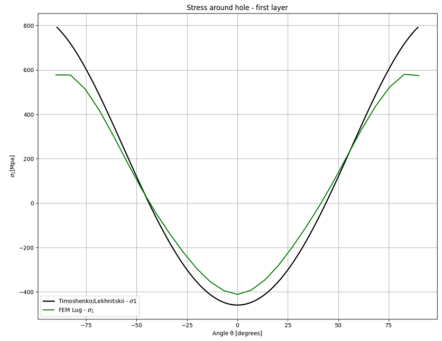

(a) σ_1 in the 0^o layer on lug with $w/D = 4$.

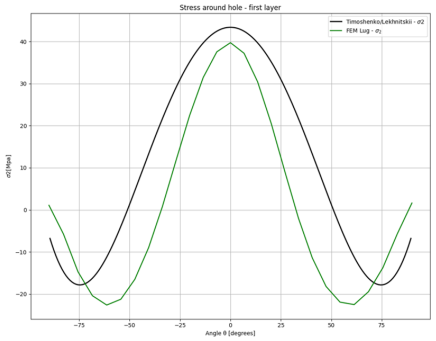

(b) σ_2 in the 0^o layer on lug with $w/D = 4$.

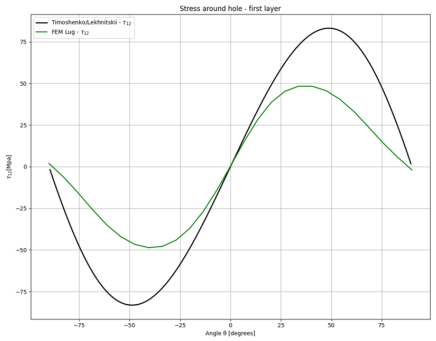

(c) τ_{12} in the 0^o layer on lug with $w/D = 4$.

Figure 4.20: Stress components in the 0^o layer on lug with $w/D = 4$ for laminate $E_x = 93.17GPa$.

The results of the two methods are in accordance. Although there are cases with a difference of 46% (e.g., τ_{12} in the 0^o layer on lug with $w/D = 4$), it pertains to areas that the stresses are not critical (e.g, difference magnitude of $20 - 30MPa$) and hence the results are considered promising. Finally, it could be concluded that the semi-analytical approach, gives a satisfactory approximation of the stresses developed in a laminate which could be used in a preliminary design phase of a composite lug.

CHAPTER 5

Experimental Validation

In order to validate the results of the numerical simulations, tensile tests were conducted. This chapter will describe a detailed overview of the experimental process. Particularly, information about the manufacturing process, micro-structural analysis, and testing set-up will be presented.

5.1 Manufacturing

With the purpose of acquiring the failure mode and load of a composite lug under tension, tensile experiments were conducted. Two different geometries of specimens were tested with the same geometric characteristics as the numerical simulation models described in Chapter 4. To recapitulate, the first geometry of the lug is similar to the geometry proposed in the paper of Kassapoglou and Townsted [43], and the geometric characteristics (Figure 3.1) are: $w = 50mm$, $D = 25$, $L = 190mm$, $e = 25mm$ ($w/D = 2$, $e/D = 1$). The second type of specimen has the same ratio w/D as the first design; however, a different e/D ratio was selected. In particular, the geometric characteristics of the second design are: $w = 40mm$, $D = 20$, $L = 190mm$, $e = 16mm$ ($w/D = 2$, $e/D = 0.8$). It is worth mentioning that the second geometry was designed in order to test how the differences in the geometric characteristics could affect the failure load and mode of a lug.

For the manufacturing of the composite specimens, curing with an autoclave was selected. A composite lug is comprised of many layers, and hence laminating processes such as hand lay-up or infusion would raise the difficulty of the manufacturing process. Furthermore, Resin Transfer Molding (RTM) techniques were not taken into account due to the high production cost of the molds [59].

All the specimens were manufactured with a prepreg carbon fiber UD tape, specifically the HexPly 8552/AS4 [58] manufactured by Hexcel. One of the main reasons for the specific selection was the availability of the material, which was provided by the composite laboratory of the Aerospace faculty of TU Delft. It is of utmost importance to mention that the material provided expired in 2015. For this reason, it was imperative to conduct a micro-structural analysis in a later stage, to assess the compaction of the layers and the fiber volume fraction of the laminate.

Manufacturing each specimen separately would require a lot of time and would increase the production difficulty. Therefore, it was deemed appropriate to manufacture a large orthogonal plate ($450mmx250mm$) that could fit all the specimens and at a later stage the specimens would be cut out with waterjet or a CNC mill.

The cutting of the prepreg material was performed by hand with a sharp cutting blade. The width

of the prepreg tape is 150mm and hence, the orthogonal plate would be made from strips of UD tape, carefully positioned next to each other, and fixed with tape in order to create an orthogonal layer. The material was cut carefully and the cuts between two adjacent layers would be at least 25.4mm (1 inch) apart as can be observed in Figure 5.1.

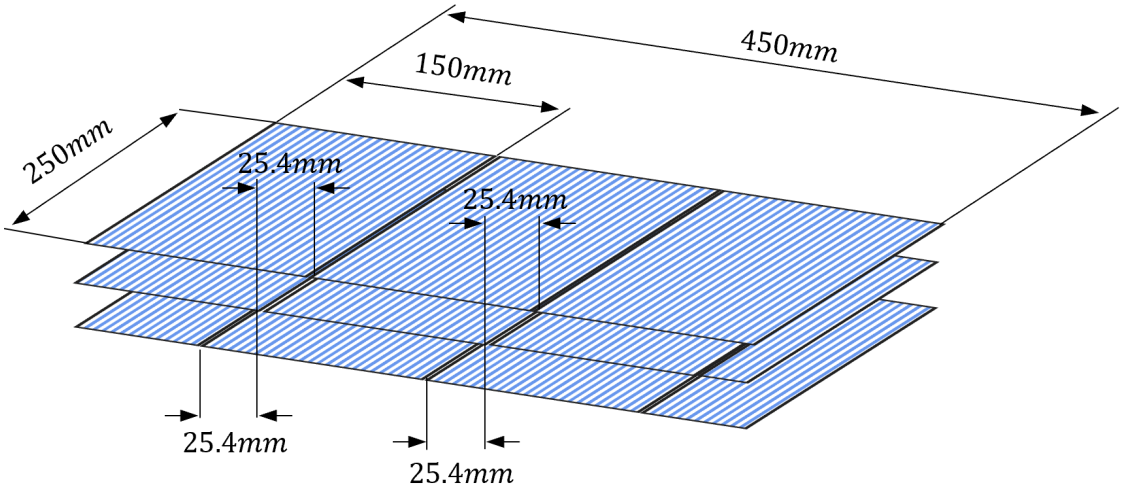

Figure 5.1: Cutting pattern of the UD tapes.

If the cuts between the layers were aligned, the strength of the plate would be minimized due to the fact that in the event of a crack propagating through the layers, the plate would break at the point where the cuts of the material were aligned. An example of how a layer of +45 degrees orientation is cut is depicted in Figure 5.2.

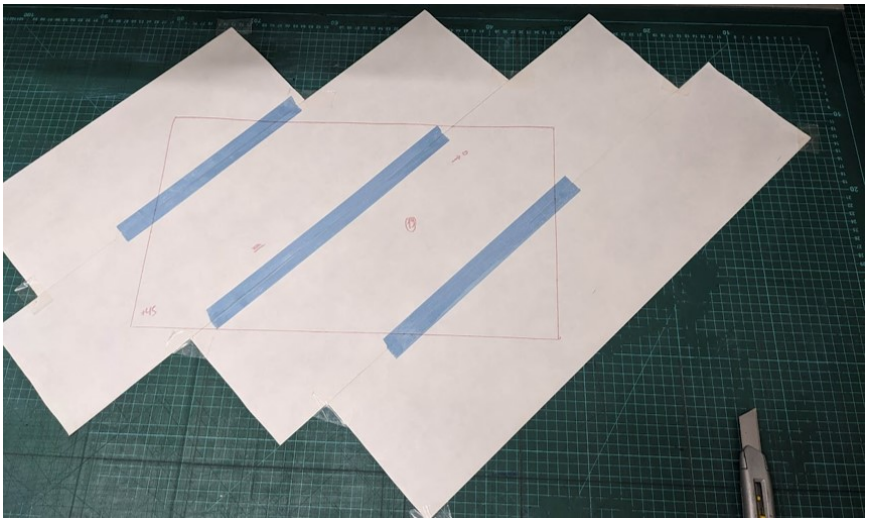

Figure 5.2: Cutting process of a 45-degree layer.

Another important step in the manufacturing process is the compaction of the layers. After all the layers are assembled and trimmed, they are placed into a debulking table. The protective film of the prepreg is removed, and the adjacent layers are placed together in pairs. The pair of layers are placed on the table and 1 bar pressure is applied for 3 minutes (Step 1). After the compaction of the pairs is completed, the protective film from one side is removed and the adjacent pairs of layers are placed together. Pressure is then applied again for 6 minutes (Step 2). The same process is repeated until all the layers are placed together (Step 3-4). This process ensures that all the layers are well compacted and potential bubbles or voids between the layers are removed. The process is described in Figure 5.3.

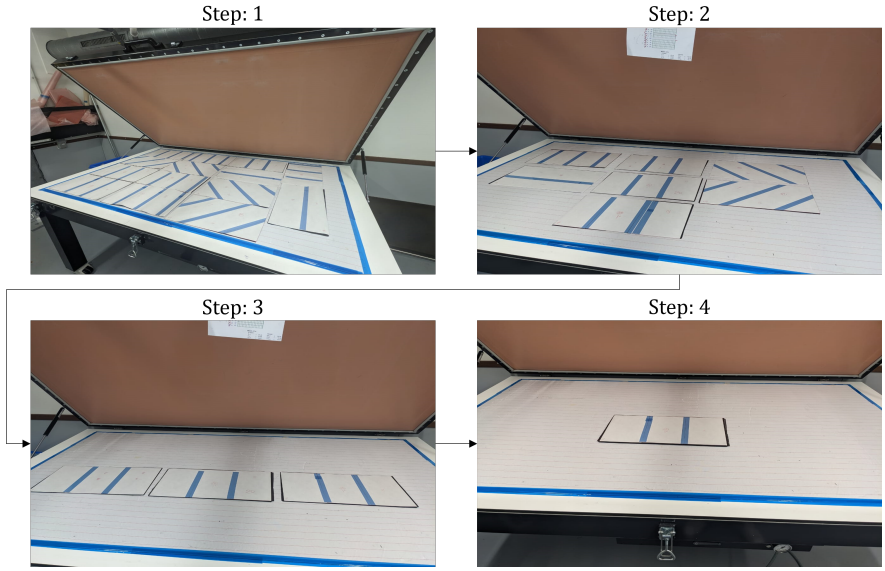

Figure 5.3: Debulking process.

The next step of the process is the preparation of the mold. An aluminum flat plate was chosen as a mold. The material of the mold was chosen due to its good thermal conductivity, ease of cleaning, and for its availability in the composite lab of the faculty. In order to prevent any type of bending of the mold due to the high temperature and the pressure applied in the autoclave, a thick plate ($t = 5mm$) was selected.

The aluminum plate is cleaned thoroughly with acetone, and then a release agent is applied. A tacky tape (sealant tape) is placed around the edge of the mold which is used later for attaching the vacuum bag. First, a peel-ply is placed on the mold, and then the orthogonal carbon fiber plate is positioned on top. Next, another layer of peel-ply is applied, and finally a layer of breather. The peel-ply ensures that the breather is not going to get bonded with the part while curing, and the breather is used for uniformly distributing the pressure applied in the vacuum bag, but also to absorb the excess resin of the prepreg [60]. Finally, the vacuum bag is placed on top, and a vacuum of 1 bar is applied. An overview of the laminating process is depicted in Figure 5.4.

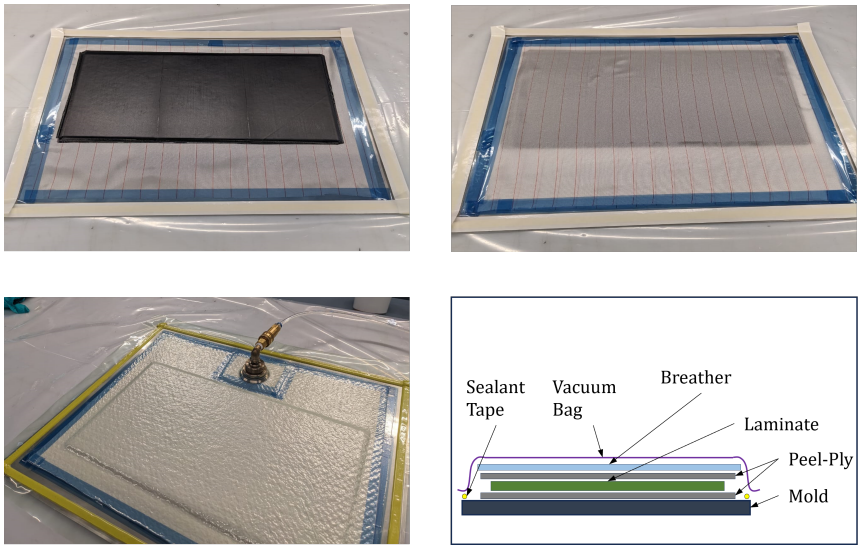

Figure 5.4: Overview of the laminating process.

When the mold is prepared, it is placed in the autoclave (Figure 5.6a). As specified by the manufacturer, the curing temperature of the material is 180 C and the applied pressure is 7 bar. The duration of the entire curing cycle is 5.5 hours and can be observed in Figure 5.5.

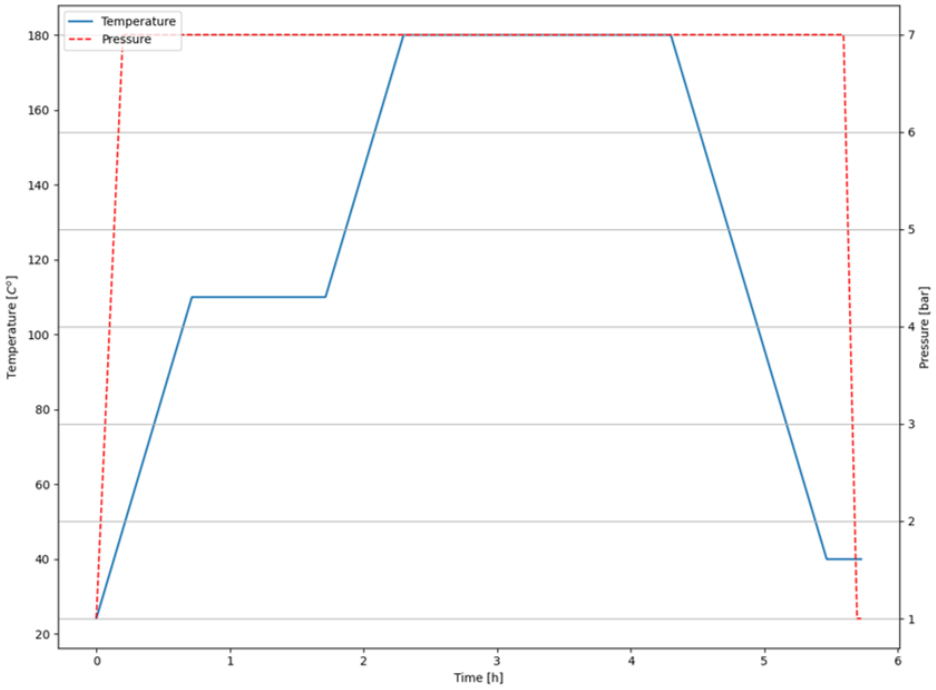

Figure 5.5: Autoclave curing cycle.

When the material is cured, it is removed from the autoclave, and the excess consumables (e.g., peel-ply, breather) are thrown away. The final cured plate is depicted in Figure 5.6b.

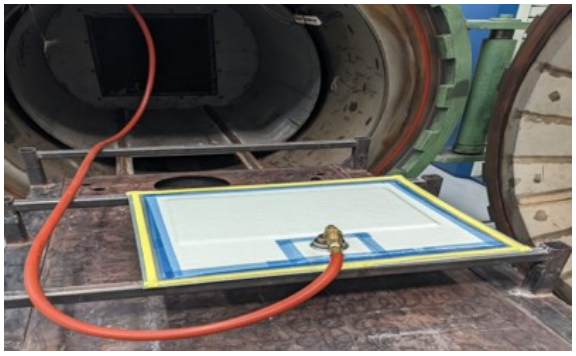

(a) Mold prepared for the autoclave.

(b) Cured composite plate.

Figure 5.6: Differences between two approaches regarding the layer lamination direction.

The final step of the manufacturing procedure is to cut out the specimens from the plate. For this process, the waterjet cutting machine was utilized. This cutting process was selected due to the high accuracy of the waterjet, and its ability to precisely cut parts with small thicknesses ($t < 10mm$). The downside of this method is that the water hits the plate with pressure which can initiate delaminations near the point of impact.

As a final stage of the manufacturing process, it was deemed appropriate to paint the area around the hole white. In this way, it would be easy to detect the appearance of cracks or delaminations at the edges while testing. The final form of the test specimens can be seen in Figure 5.7.

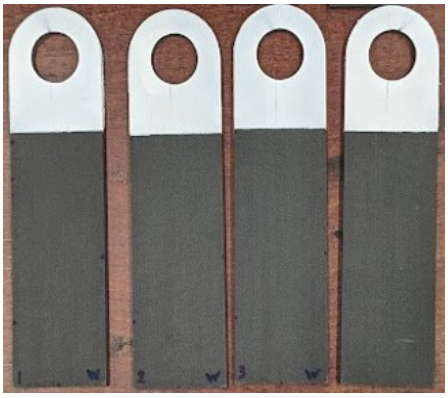

(a) Lug geometry 1: $w/D = 2$, $e/D = 1$.

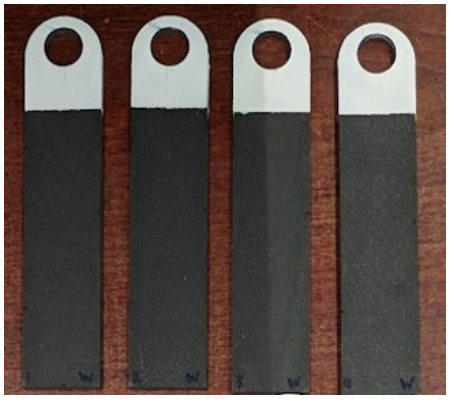

(b) Lug geometry 2: $w/D = 2$, $e/D = 0.8$.

Figure 5.7: Lug specimens.

Before initiating the testing phase, a microstructural analysis was conducted. This step aided in calculating the fiber volume fraction and detecting the presence of voids in the laminate. Moreover, an attempt was made to predict the angle deviation of the fibers with regard to the laminate's direction.

5.2 Micro-Structural Analysis

Micro-structural analysis is the study of the laminate at a microscopic level. The interaction of the constituents of the laminate (e.g., fibers, matrix) are studied in the scale of a fiber's diameter (μm) [61]. By observing a part of the laminate in this scale, the presence of voids, the compaction of the layers, and the exact fiber orientation after manufacturing can be calculated.

5.2.1 Specimen Manufacturing

As a first step of this process, a piece of the laminate is cut with a diamond saw. The diamond blade ensures that the edges of the sample that are placed in the microscope will not get damaged or scratched. The samples are placed in a silicon mold and a fast-curing resin is poured. The sample that was used for the analysis is presented in Figure 5.8.

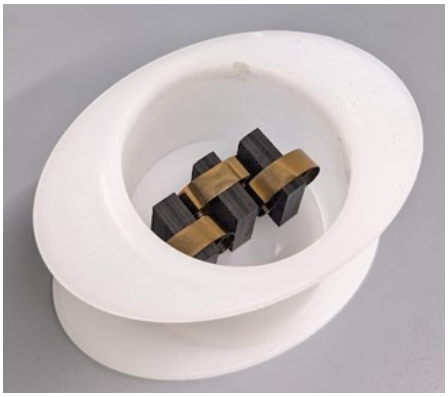

(a) Samples placed in the silicon mold.

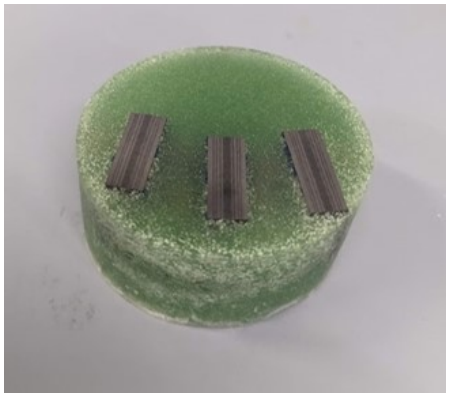

(b) Final form of the sample before polishing.

Figure 5.8: Preparation of the samples for micro-structural analysis.

Next, the sample is sanded with various sanding papers starting from Grid 200 up to Grid 2000 and then polished. For this process, a machine is used, which applies a standard force in order not

to create scratches on the specimens (Figure 5.9a). The sanding and polishing process achieves a smooth surface on the sample, which is later placed under the microscope (Figure 5.9b).

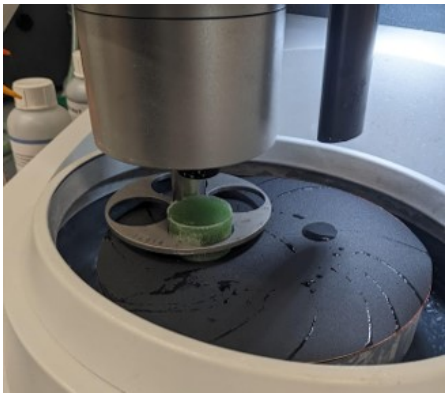

(a) Sample in the sanding/polishing machine.

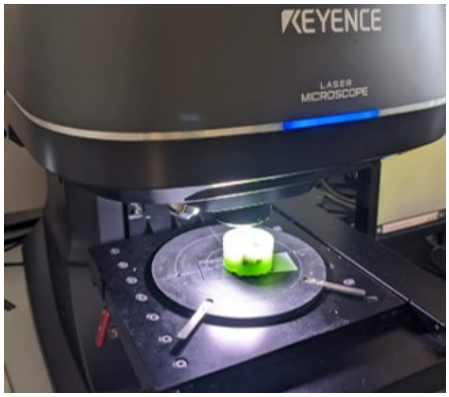

(b) Sample under the microscope.

Figure 5.9: Machines used for the micro-structural analysis.

In order to have variability in the results, 6 specimens were created. In 3 specimens (Type A) the 0-degree fibers point toward the lens of the microscope (upward), and in the rest (Type B) the 90-degree fibers point upward. A 20x magnification lens was used, and images were collected from different regions of the specimens. The final result of the magnification for a random sample is illustrated in Figure 5.10.

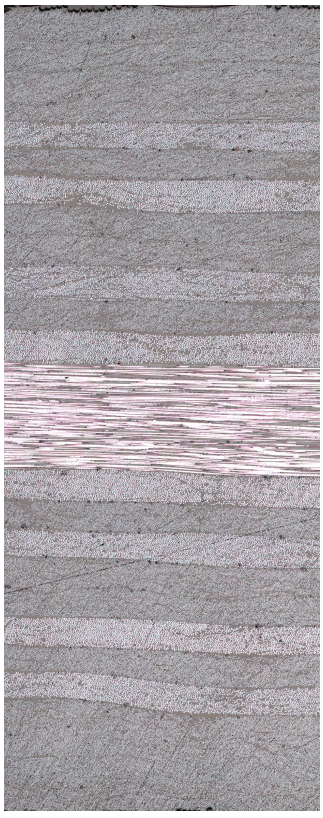

(a) Sample Type A.

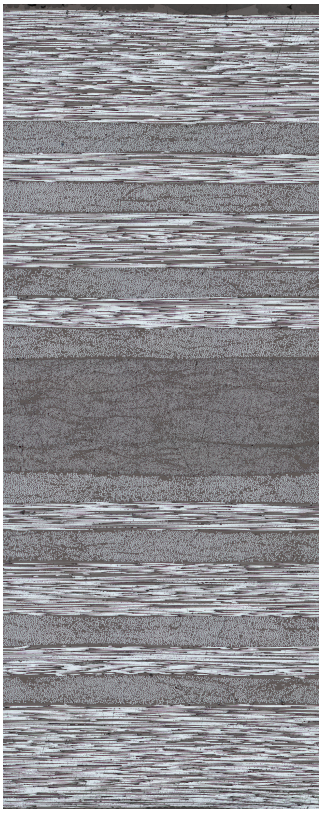

(b) Sample Type B.

Figure 5.10: Images from the microscope for the two types of samples.

5.2.2 Fiber Volume fraction estimation

Process description

The fiber volume fraction (V_f) of the laminate is obtained by implementing image processing techniques. Since this is not the scope of the thesis a simple explanation will be given. In a grayscale image (all colors in the image are shades of black and white e.g., Figure 5.10) the intensity of a pixel ranges between 0 and 255 bins. The color black is represented by 0 bins and the color white by 255. By creating a histogram of the pixel intensity of an image, a threshold value can be determined. This value is utilized for converting the image into binary (image with only white and black pixels) [62]. Particularly, all the pixels with values below the threshold are converted to black and the rest to white. It can be assumed that the pixels with values below the threshold represent the matrix and potential voids and the pixels above the threshold represent the fibers. The binarization of the image with the threshold method is depicted in Figure 5.11.

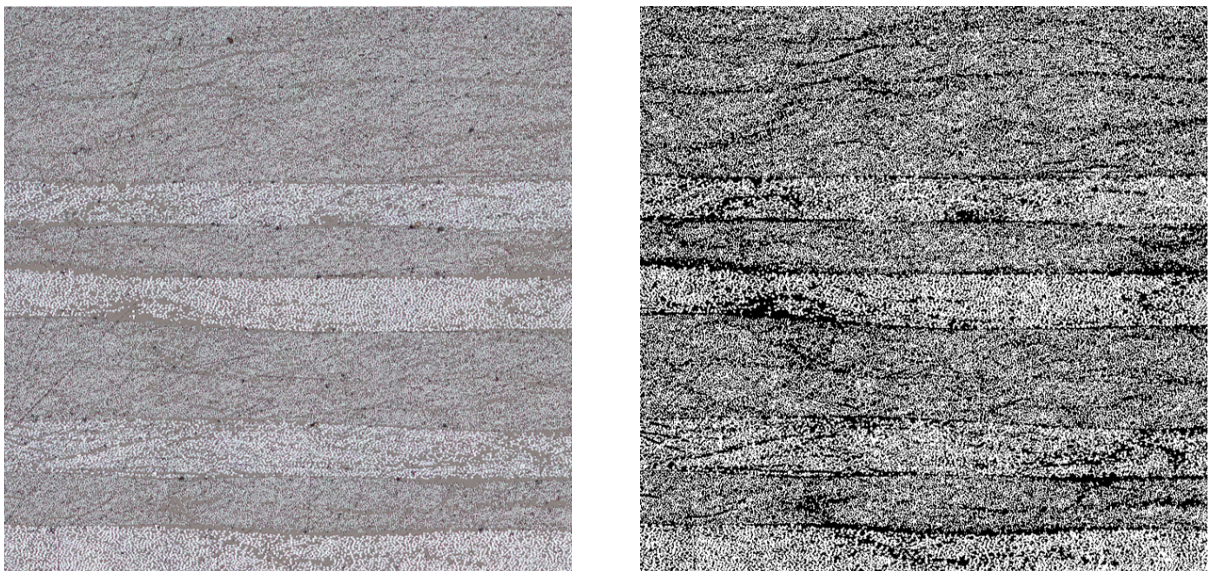

(a) Grayscale image. (b) Binary image.

Figure 5.11: Microscope images for the two types of samples.

When the image from the microscope is transformed to binary, the white pixels represent the fibers. Hence, the fiber volume can be calculated as the ratio of the white pixels divided by the total number of pixels in the image.

Tensile specimen laminate V_f estimation

Analyzing the image of the $[0_4/45/0/-45/0_2/45/0/-45/90_2]_s$ laminate from the first three specimens (Type A, Figure 5.10a) it can be observed that the 90 layers in the middle of the laminate appear as white lines, and hence this would result in incorrect calculation of the fiber volume fraction. For this reason, these types of specimens are divided into a top and a bottom region which are processed as separate images. For each region the pixel intensity is analyzed with a histogram and the threshold value for the specific image is specified. The histogram of the top region of the first specimen is depicted in Figure 5.12.

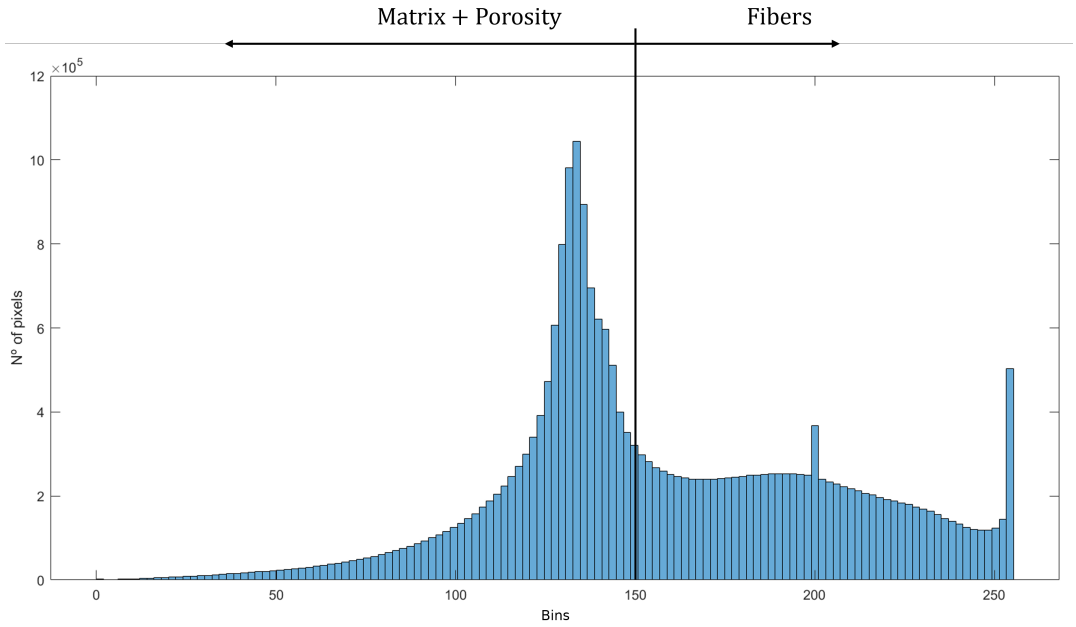

Figure 5.12: Histogram of the pixel density of an image.

After binarizing the images, each region is divided into smaller areas. In each of the areas, the fiber volume fraction is calculated and then averaged to obtain the total V_f of the region. A convergence study was conducted and it was noticed that the optimal number of areas that a region should be divided is 10. The result of the convergence study indicated that the change in the average fiber volume fraction is lower than 2% for a number of areas greater than 10. The final value of V_f of type A specimens is the average of all the areas of the two regions. The process described is illustrated in Figure 5.13.

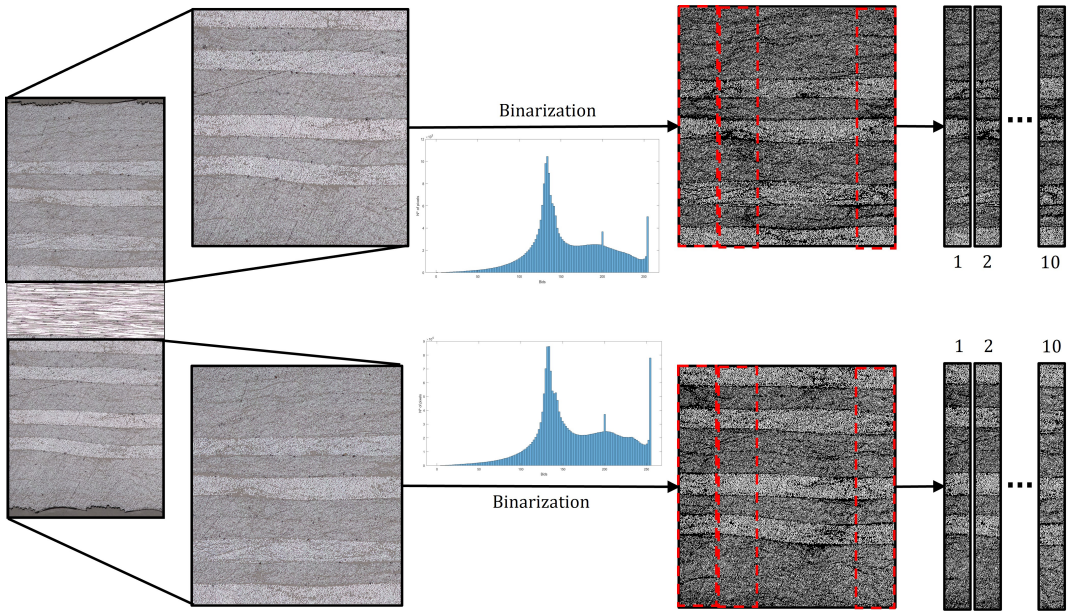

Figure 5.13: Process of estimating the V_f of a laminate.

For type B specimens (Figure 5.10b), only one region is distinguished, specifically the region that contains the 90-degree fibers in the middle of the laminate. This middle region is divided into 10 areas and an average V_f value is calculated for the specimen. For each of the specimens, one V_f

value is calculated and the overall fiber volume of the laminate is the average of all the values. The results of this method are presented in Table 5.1.

Table 5.1: Calculation of the overall V_f of the laminate.

Specimens	**Regions**			**Avg** V_f
-	**Bottom**	**Middle**	**Top**	[-]
A_1	0.526	-	0.524	0.525
A_2	0.497	-	0.545	0.521
A_3	0.588	-	0.526	0.557
B_1	-	0.560	-	0.560
B_2	-	0.488	-	0.488
B_3	-	0.477	-	0.477
	Overall V_f			**0.525**

As can be observed from table 5.1, the overall fiber volume fraction of the laminate is 0.525. The achieved V_f is lower than the fiber volume fraction specified by the manufacturer (V_f = 0.66) [58]. This difference is attributed to the presence of voids and most importantly to the fact that the material was expired. However, the V_f is within the boundaries of a laminate manufactured with the autoclave process (V_f>0.5 [63]) and hence the results of the manufacturing process are considered satisfactory.

5.2.3 Fiber orientation estimation

Observing the image of the microscope the constituents of the laminate can be detected. In particular, as depicted in Figure 5.14, the fibers are represented by circles or ellipses, and the matrix by the grey area between the fibers. Moreover, some matrix-rich areas are also evident, along with scratches, voids, or defects that were inflicted on the specimen during the sanding process.

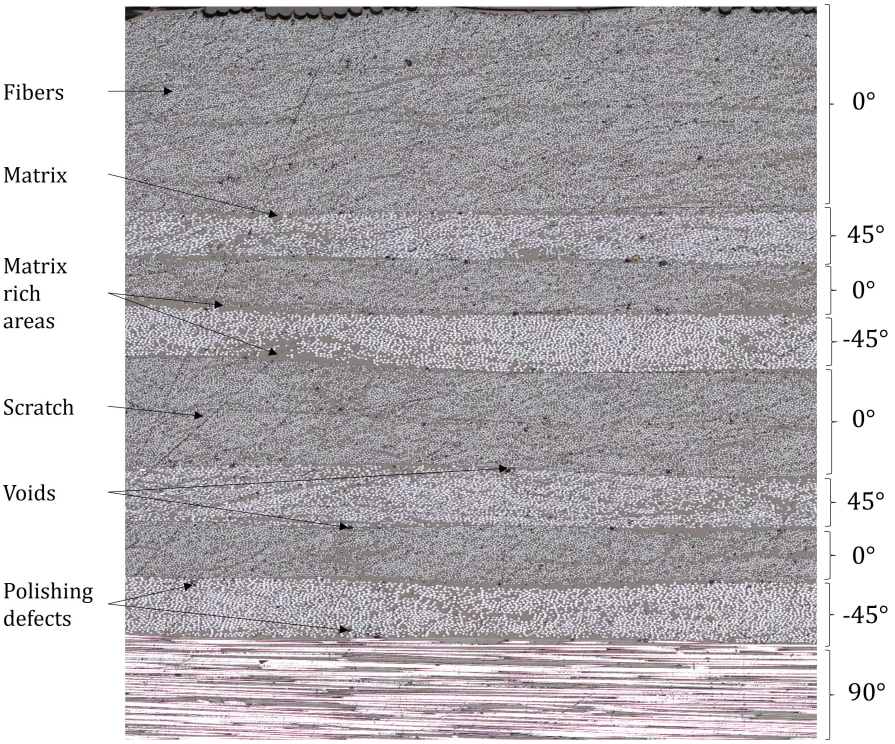

Figure 5.14: Distinction of laminate features.

In addition, from the image, a distinction between the material orientation can be made. The 0 orientation fibers have the shape of a circle, whereas the fibers that are cut at a 45 angle have the shape of an ellipse. Based on the literature [49], the diameter of an AS4 fiber is $7\mu m$ and hence the area of the circle is $A = 38.4\ \mu m^2$. By calculating the area of the circles in the microscopy image and comparing it with the value from the literature, the deviation from the ideal 0-degree fiber can be obtained. With this process, the manufacturing error of the laminating and cutting process is evaluated.

In order to obtain the area of the circles and ellipses, image processing techniques are utilized. In particular, every layer of the laminate is processed separately. After the image is binarized, a circle/ellipse detection algorithm [64] is applied to the white pixels (Figure 5.15). In a later stage, the area of the circles or ellipses is estimated in pixel units.

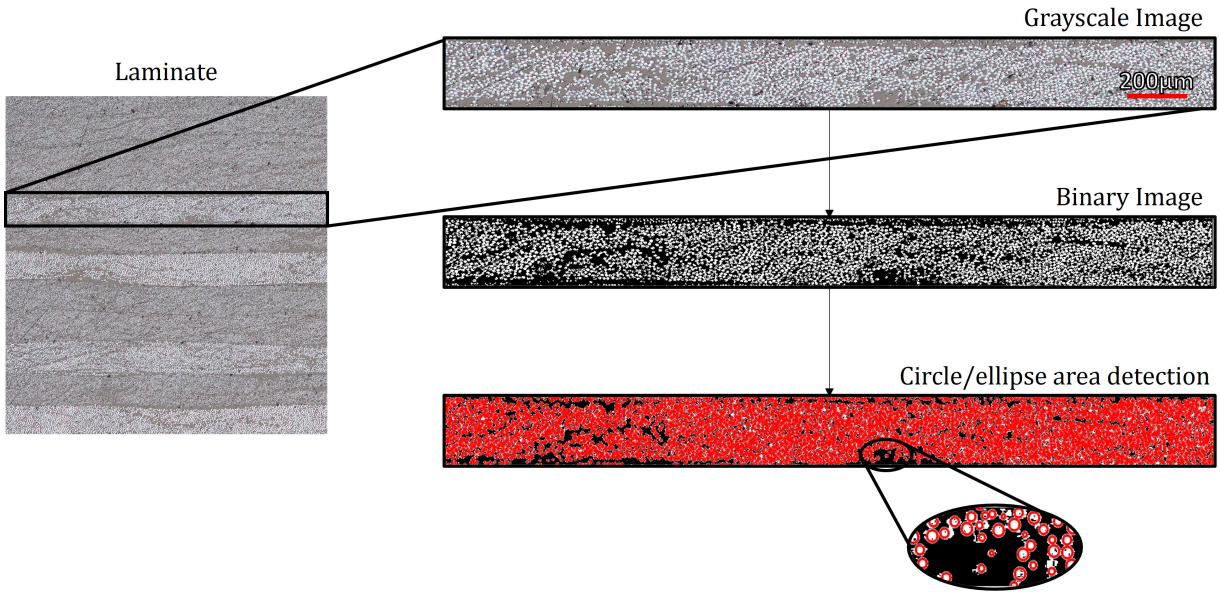

Figure 5.15: Process of detecting circles or ellipses and calculating their area.

The pixel-to-length ratio ($r_{pxl-\mu m}$) is obtained by utilizing specific image processing software such as ImageJ. A known distance is selected on the image in length units, and the program calculates the analogy between pixels and length units. The area of the fibers is finally calculated as $A_{\mu m}$= $A_{pixels} \cdot r^2_{pxl-\mu m}$.

For the case of 45^o layers, the cross-section of the fiber is an ellipse. The area of this ellipse is calculated by utilizing a CAD program, namely Solidworks. To elaborate, a $7\mu m$ fiber is designed and then cut at an angle of 45^o. The area of the ellipse is then compared with the area calculated from the ellipse detection algorithm.

The average fiber cross-sectional areas estimated with the algorithm are compared with the areas calculated from the CAD program. However, there are cases where the values of the areas of the two methods do not match. For this reason, the fiber is cut in Solidworks at various angles until the value of the area is within an acceptable range from the area calculated with the ellipse detection algorithm. The cut angle with the same area is finally the actual orientation of the layer.

For instance, by applying the method presented in Figure 5.15, the average area of the 45^o layer is estimated to be equal to $A_{45^o-detectAlg} = 55.91\mu m^2$. However, as it can be observed in Figure 5.16, this area corresponds to a fiber orientation of approximately 46^o. Hence it can be assumed that the actual orientation of the fibers of the specimen that was manufactured has 1^o deviation from the

orientation that was designed for.

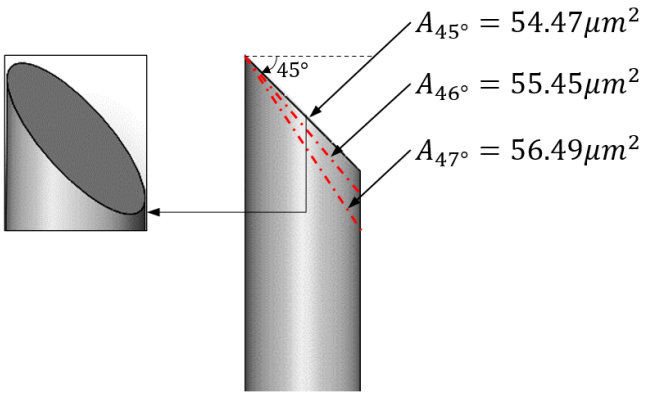

Figure 5.16: Calculation of the area of the fiber depending on its orientation.

The 90^o layers are depicted as circles in the Type B specimens and therefore the same technique as the 0^o layers is applied. By performing this method for every layer of the laminate for every specimen, the actual orientation of the fibers of the laminate is obtained. The results are presented in Table 5.2.

Table 5.2: Estimation of the fiber deviation.

	Specimen orientation						
Designed orientation	A_1	A_2	A_3	B_1	B_2	B_3	**Avg. Deviation**
[^{o}]	[^{o}]	[^{o}]	[^{o}]	[^{o}]	[^{o}]	[^{o}]	[^{o}]
0	1	0	1	-	-	-	0.66
45	46	47	45	-	-	-	1
90	-	-	-	90	90	91	0.33

From the results, it can be observed that the 0^o fibers are actually 0.66^o, the 45^o are 46^o and the 90^o are 90.33^o. It is worth mentioning that this approach is an estimate of the actual orientation of the fibers' deviation. The results of the algorithm have a variance based on the selected threshold value.

5.3 Testing set-up

For every geometry, a total of 4 specimens were manufactured. The number of specimens is an attempt to gain a better insight about the variability of the results. Although a higher number of specimens would provide more information, the processing of all the data would require a lot of time. Since the tensile tests are a validation method and not the sole purpose of the thesis, the number of specimens was considered satisfactory.

It is important to note that the primary objective was to acquire the failure load and mode of the lug, and hence no strain gauges were attached to the specimens. Moreover, in order to get an accurate measurement of the displacement in the middle of the specimen, an extensometer was attached. Finally, a high-speed camera and a source of light were placed opposite to the specimen in order to observe the phenomena that occur in the exact moment of failure.

The test-set up was a clevis and pin configuration on top, and a clamp on the bottom. Specifically, the specimen was placed inside the clevis and a pin was used in order to ensure the connection between the parts. While the bottom part of the specimen was fixed inside the clamp, an upward

force was applied to the clevis, resulting in a tensile load on the specimen through the pin. The actual configuration of the test set-up is presented in Figure 5.17.

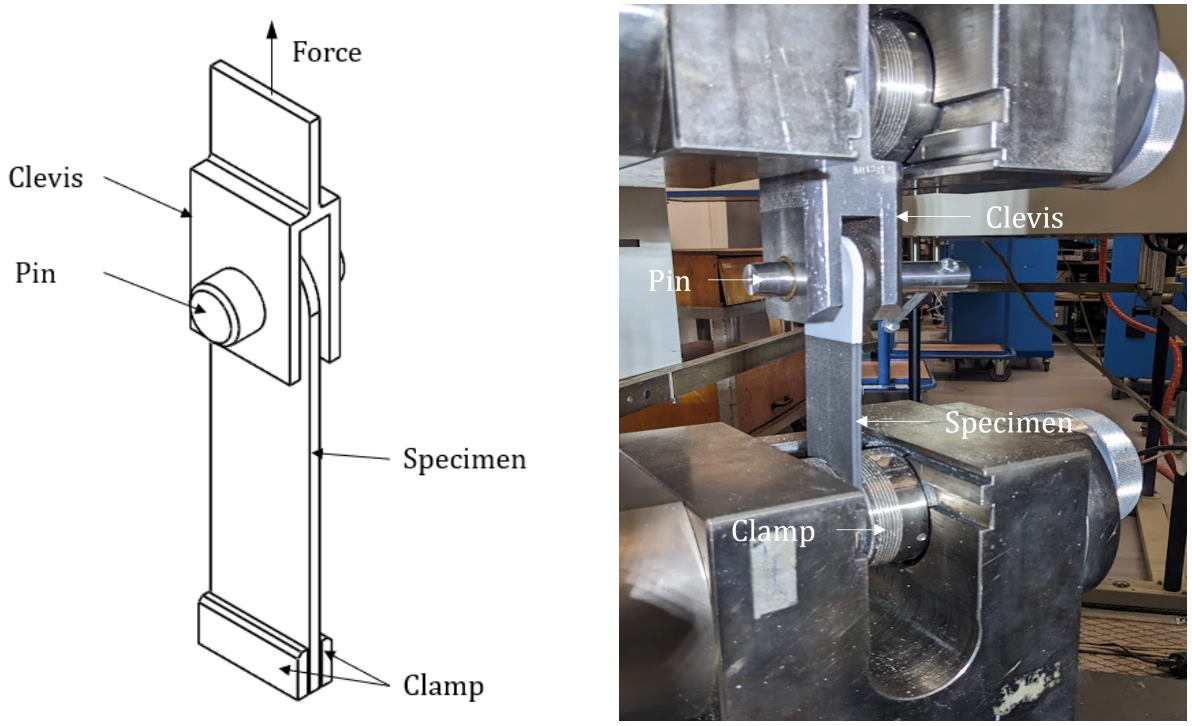

(a) Schematic of the test set-up.

(b) Tensile test set-up.

Figure 5.17: Configuration of the tensile test.

5.4 Data collection and analysis

In the tensile test, in the first stage, the applied force and the displacement of the machine can be measured. From the moment the pin is engaged in the hole, a force-displacement curve can be obtained. However, if there is enough clearance between the pin and the hole, a zero-force region can be observed at the beginning of the curve [65].

When the pin is finally engaged, the linear part of the curve starts which represents the resistance of the composite lug to the applied load (Figure 5.18). While the load increases, the laminate starts getting damaged, which can be detected by a characteristic cracking noise and a small abrupt change in the linear part of the curve. Although the noise represents the First Ply Failure of the laminate, the load continues to increase.

A sudden drop of the curve represents the point where the load exceeded the capacity of the composite. If the load continues to increase to higher load values after that drop, it means that the ultimate strength of the laminate is not reached. Finally, when the laminate cannot withstand any increase in the load, the curve plunges to low load levels, which corresponds to the Last Ply Failure.

The failure load of the laminate is considered the highest value of the load during the tensile tests. After that point, it can be observed the laminate does not have the capacity to withstand any higher loads. The tensile tests were terminated a few seconds after the failure of the lug.

The displacement presented in this graph represents the displacement of the machine's head. There-

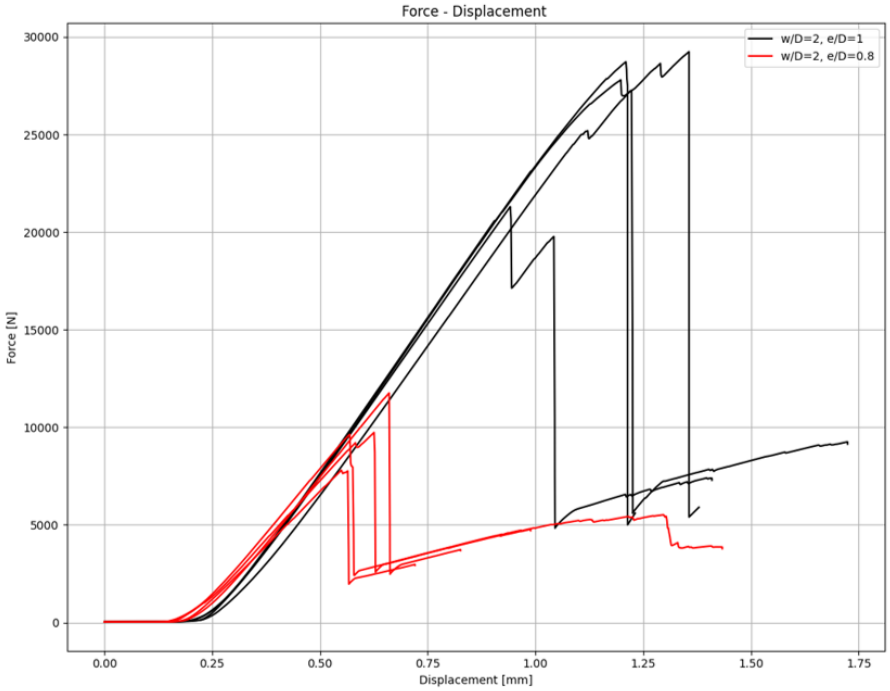

Figure 5.18: Force displacement curves from machine data.

fore, due to the fact that there are many components involved, there is a high possibility of noise (or else compliance) in the results due to the relative displacement between the various components. In order to account for this an extensometer was attached during testing of every specimen. This device measures the displacement on the specimen and hence is considered more accurate. The force-displacement with data from the extensometer is depicted in Figure 5.19.

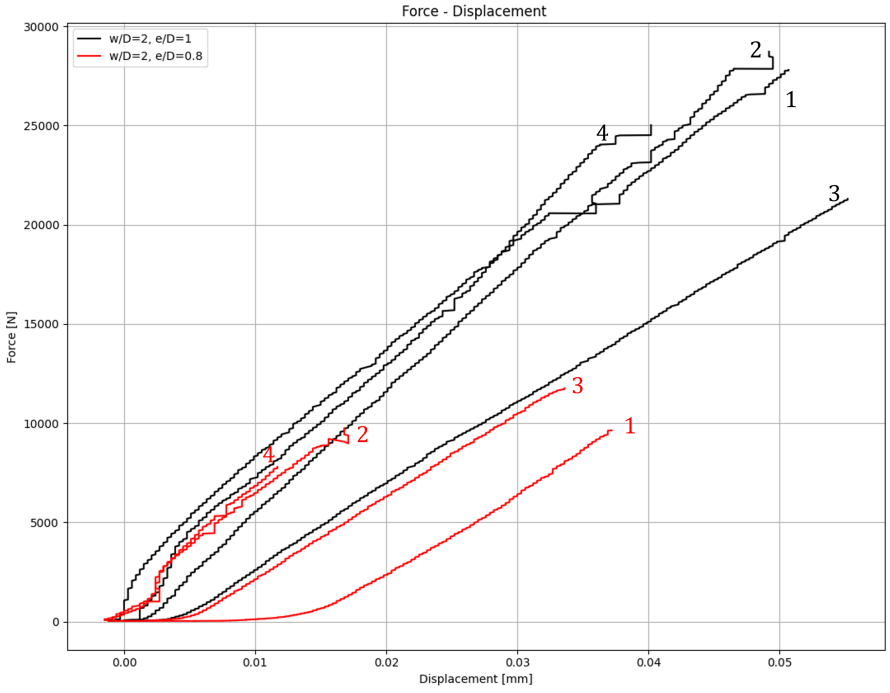

Figure 5.19: Force displacement curves from extensometer data.

The highest point of these curves represents the failure load of the specimen. When failure occurs

on the specimen, the extensometer loses contact with the specimen and therefore every data acquired after failure are not considered valid.

In the beginning, a zero-force region can also be observed. Moreover, in the same phase, it can be noticed that some of the curves have some noise and then the linear part of the curve starts. This phenomenon is due to the fact that although force is applied, the grip between the extensometer and the specimen was not satisfactory. Hence the force is increased but the extensometer does not read any displacement.

Another feature that can be observed in these curves is some abrupt changes in the slope of the curve. These changes are interpreted as a sign of damage to the lug. This is substantiated by measurements that were taken during testing. Particularly, when a cracking noise was heard during testing the force was noted down. At a later phase, these noises were matched with the changes in the slope of the curves.

The variance between the results of the different specimens is attributed to the manufacturing method. During the water-jet cutting some delaminations were initiated in the area around the circle. This phenomenon was more obvious in the specimens with a smaller diameter ($w/D = 2$, $e/D = 0.8$). Finally, the failure load of every specimen is presented in Table 5.3.

Table 5.3: Failure load of every specimen.

	Failure Load	
Specimen	$w/D = 2$**,** $e/d = 1$ $[N]$	$w/D = 2$**,** $e/d = 0.8$ $[N]$
1	27794.93	9633.64
2	28721.61	9734.00
3	21301.73	11757.64
4	29241.22	7799.00

As was expected the geometry of the lug has a significant effect on the failure load. The difference between the geometric characteristics of Design 1 ($w = 50mm$, $D = 25$, $L = 190mm$, $e = 25mm$, $w/D = 2$, $e/D = 1$) and Design 2 ($w = 40mm$, $D = 20$, $L = 190mm$, $e = 16mm$, $w/D = 2$, $e/D = 0.8$) resulted in a drop of the failure load of approximately 63%.

5.5 FEM Validation

One of the main reasons for conducting tensile experiments was the validation of the numerical simulation models. For a more accurate comparison of the two methods, the boundary and loading conditions of the experimental set-up are transferred into a FEM model. In this way, the modeling approach of the numerical simulation models is validated.

The modeling approach of the numerical simulation is described in detail in Chapter 4. However, the boundary conditions are altered in order to match the tensile experiments. In particular, the loading of the lug is applied as a displacement in the middle of the hole instead of a cosinusoidal shell edge load. In order to account for the presence of a pin, a coupling constraint is applied on the top half part of the hole. Finally, the clamp on the bottom part of the lug is modeled with a fixed condition that restrains all the degrees of freedom. The boundary conditions are depicted in Figure 5.20.

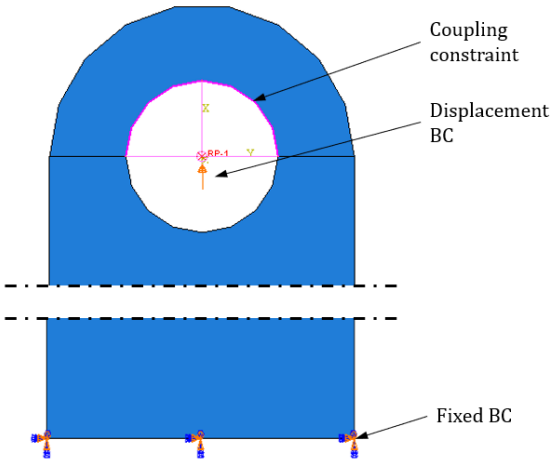

Figure 5.20: Boundary conditions of FEM model that resembles the tensile experiment.

In order to calculate the displacement of the specimen in the FEM model two sections cuts are made at the same point where the extensometer is attached to the actual tensile experiment. The displacement of all the elements in the loading direction of the top section is calculated and then subtracted from the element displacement at the bottom section. Hence, the relative displacement of the specimen is calculated by imitating the way that the displacement is measured with the use of an extensometer. The results of comparing the force-displacement curves from the two methods (numerical and tests) are presented in Figure 5.21.

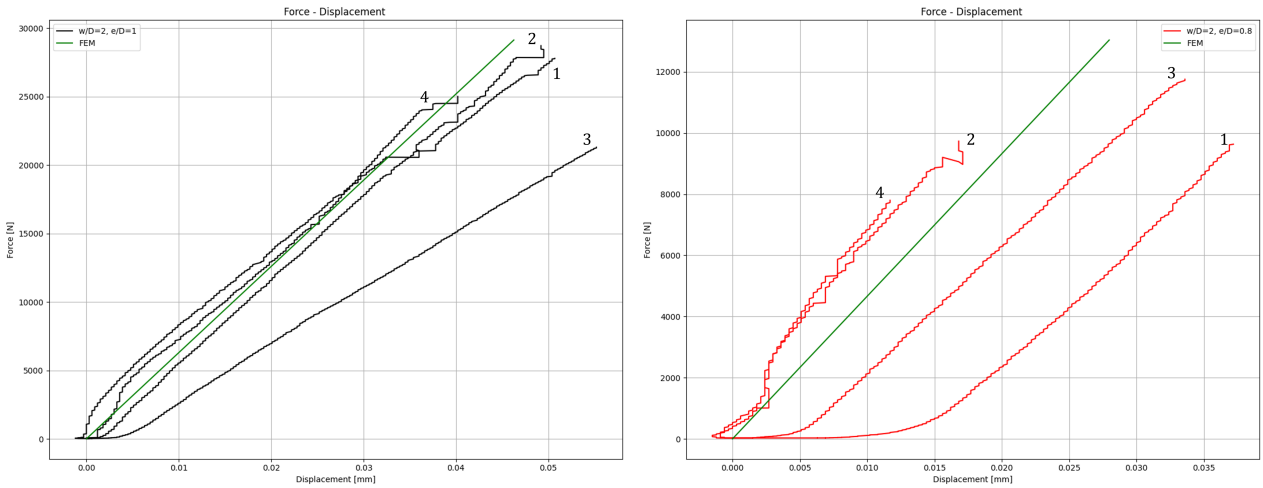

(a) Force displacement $w/D = 2$, $e/D = 1$.

(b) Force displacement $w/D = 2$, $e/D = 0.8$.

Figure 5.21: Force displacement curves comparison between extensometer and FEM approach.

The comparison of the slopes of these curves proves that the numerical simulation approaches the tensile experiments and the results (regarding force-displacement) of the two methods are in accordance. In order to further validate the numerical approach, the stress-strain curves of the two methods were compared in two regions. One region is the middle of the specimen, and the second region is next to the hole. Particularly, in the tensile experiments the gross stress can be estimated by the equation [3],

$$\sigma_{gross} = \frac{F}{w \cdot h}$$

where w is the width of the lug and h is the thickness of the laminate. The strain is calculated by [3],

$$\epsilon = \frac{\Delta L}{L_0}$$

with ΔL being the displacement of the extensometer and L_0 its initial length. The net section stress is specified by [3],

$$\sigma_{net} = \frac{F}{(w - D) \cdot h}$$

where D is the hole diameter. It is of utmost importance to mention that it is assumed that the stress is distributed uniformly in these regions. Hence, by utilizing these curves the stress-strain curves are obtained for the case of the tensile experiments.

For the case of the numerical simulations, the approach differs. Specifically, the FEM model calculates the stresses in the principal directions (1: fibers, 2: matrix), for every element in every layer. In order to obtain the gross stress, a region in the middle of the specimen is defined (the middle is selected so that the stress field is not influenced by the stress concentration around the hole). Additionally, the principal stresses (σ_1, σ_2, τ_{12}) are calculated for a specific element and then translated to the global system (x, y of the model) with the use of a transformation matrix (Equation B.1.3). The value of the stress in the loading direction is calculated for that element through the thickness of the laminate and then averaged. For every element in the middle of the specimen, a stress value is calculated. Finally, the gross stress is the average of the stress values of all the elements in the width direction. The methodology is depicted in Figure 5.22.

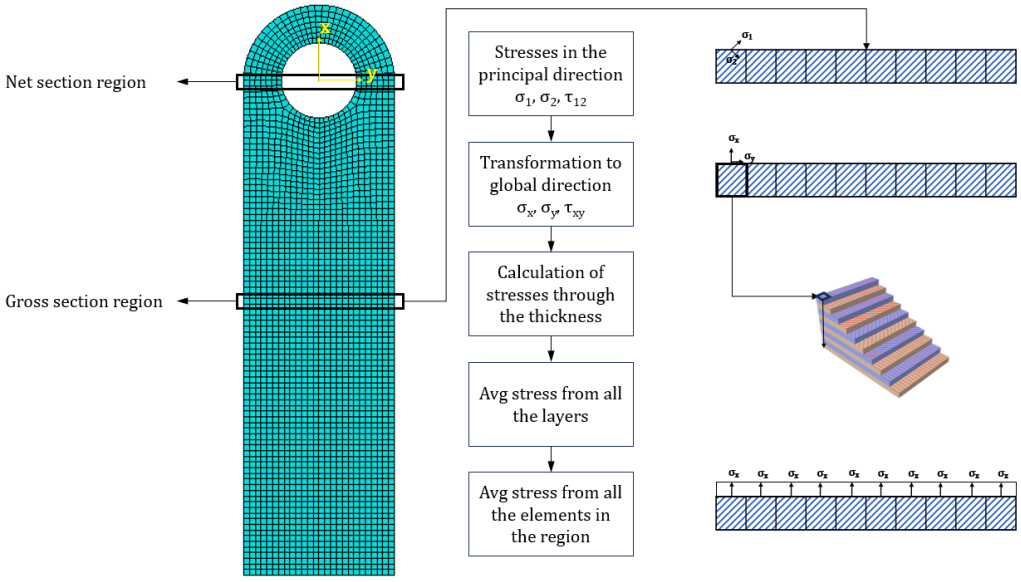

Figure 5.22: Methodology to predict the gross & net stress from a FEM model.

The exact same process is applied to calculate the strains of the model. Moreover, the process described in the previous paragraph is applied to the calculation of the net stress. However, a region is selected next to the hole and not in the middle of the specimen as in the case of gross stress. This approach is valid for a specific time instance. In order to create a curve, this methodology is applied for various time frames, until the first-ply-failure of the laminate.

The stress-strain curves of the numerical and experimental method for the gross stress are presented in Figure 5.23.

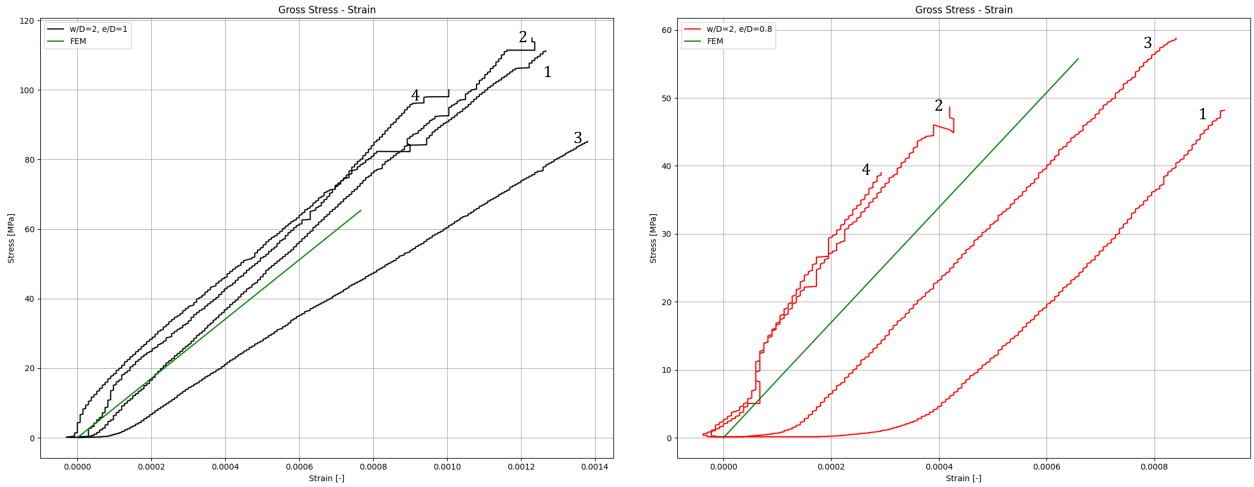

(a) Gross stress-strain $w/D = 2$, $e/D = 1$.

(b) Gross stress-strain $w/D = 2$, $e/D = 0.8$.

Figure 5.23: Gross stress-strain curves comparison between experimental and FEM approach.

As can be observed, the averaging of the stresses in the FEM model did not influence the distribution of the stresses, and hence it can be concluded that the results of the two methods regarding the gross stress are in close proximity. Regarding the net section, the stress-strain curves are depicted in Figure 5.24.

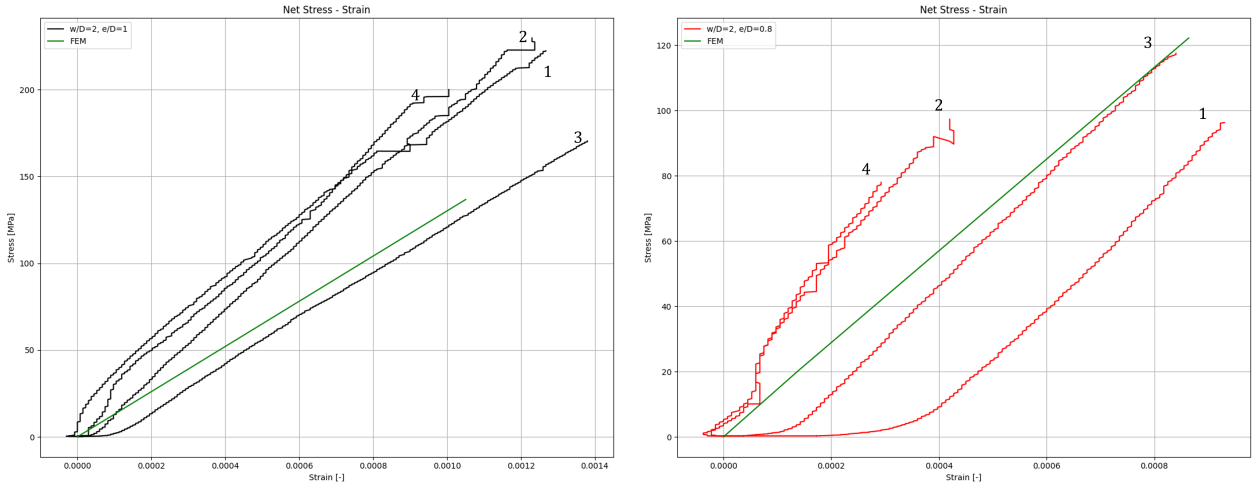

(a) Net stress-strain $w/D = 2$, $e/D = 1$.

(b) Net stress-strain $w/D = 2$, $e/D = 0.8$.

Figure 5.24: Net stress-strain curves comparison between experimental and FEM approach.

From the curves, it can be noticed that the slopes of the two methods do not match very well. This discrepancy is attributed to the fact that in the FEM model, the stress field around the hole follows a very steep curve. Averaging the stress and assuming a uniform distribution results in a smaller slope for the FEM curve. However, although the curve of the numerical method is less steep, it still is within the boundaries of the curves of the tensile tests.

In order to quantify the difference between the methods regarding the gross stress, the slope of the curves was estimated. Particularly, the slope of the stress-strain curve is the stiffness of the laminate in the loading direction (E_x). The results for the Design 1 ($w/D = 2$, $e/D = 1$) and Design 2 ($w/D = 2$, $e/D = 0.8$) specimens are presented in Table 5.4 and Table 5.5 respectively.

Table 5.4: Comparison of the stiffness of the laminate between the specimens and FEM (Design 1).

Design 1: $w/D = 2$, $e/d = 1$

Specimen	E_x	**Dif with FEM**	**Perc Dif with FEM**	**Avg** E_x	**Avg Dif with FEM**	**Perc Avg Dif with FEM**
Units	$[N/mm^2]$	$[N/mm^2]$	[%]	$[N/mm^2]$	$[N/mm^2]$	[%]
1	87500	-2300	2.70			
2	91000	-5800	6.81	84100	1100	**1.29**
3	72250	12950	15.20			
4	85650	-450	0.53			
FEM	85200	-	-	-	-	-

Table 5.5: Comparison of the stiffness of the laminate between the specimens and FEM (Design 2).

Design 2: $w/D = 2$, $e/d = 0.8$

Specimen	E_x	**Dif with FEM**	**Perc Dif with FEM**	**Avg** E_x	**Avg Dif with FEM**	**Perc Avg Dif with FEM**
Units	$[N/mm^2]$	$[N/mm^2]$	[%]	$[N/mm^2]$	$[N/mm^2]$	[%]
1	80079	5121	6.0			
2	90337	-5137	6.0	86770	1570	**1.84**
3	83058	2142	2.5			
4	93605	-8405	9.9			
FEM	85200	-	-	-	-	-

For Design 1 the average calculated E_x from the tensile experiments is $84100MPa$, whereas the estimated E_x from the numerical simulation is $85200MPa$. This leads to a difference of 1.29%. In the case of Design 2, the calculated stiffness in the loading direction is $86770MPa$, and from the FEM model is again $85200MPa$. The difference between the two methods is 1.84%. In conclusion, the results of the stress-strain curves, and the stiffness in the loading direction, validate the numerical approach. Therefore, the results of the in-plane FEM method are trustworthy and can be used as a valid reference for comparing them with the results of the semi-analytical solution.

5.5.1 First Ply Failure

As it was described in section 4.3, for the numerical simulations the Tsai-Hill failure criterion was selected. By gradually increasing the load in the FEM model, it was observed that the first ply that fails is the 90^o in the middle of the laminate. It is worth noting, that the failure of the 90^o occurs in both geometries that were tested. Regarding the experimental method, while performing the tensile tests, every time a cracking noise was heard, the load of the machine was noted down. Furthermore, in the force-displacement curves (extensometer data), the first time that a sudden change in the slope of the specimen was observed, the load was also noted down. If the load that the noise was heard was in the area of the abrupt change of the slope of the curve, it was assumed that the first cracking noise corresponds to the first ply failure of the laminate. Finally, the first ply failure of every specimen and the FEM model is presented in Table 5.6.

Table 5.6: First Ply Failure load of every specimen.

	First Ply Failure Load	
Specimen	$w/D = 2$, $e/d = 1$	$w/D = 2$, $e/d = 0.8$
	$[N]$	$[N]$
1	19359	7727
2	12883	4458
3	13347	10401
4	15690	5535
Average	15319	7030
FEM	14320	12600

Moreover, the change in the slope when the first ply failure occurs is noted in the force-displacement graph with an asterisk. The results for the two geometries are depicted in Figure 5.25.

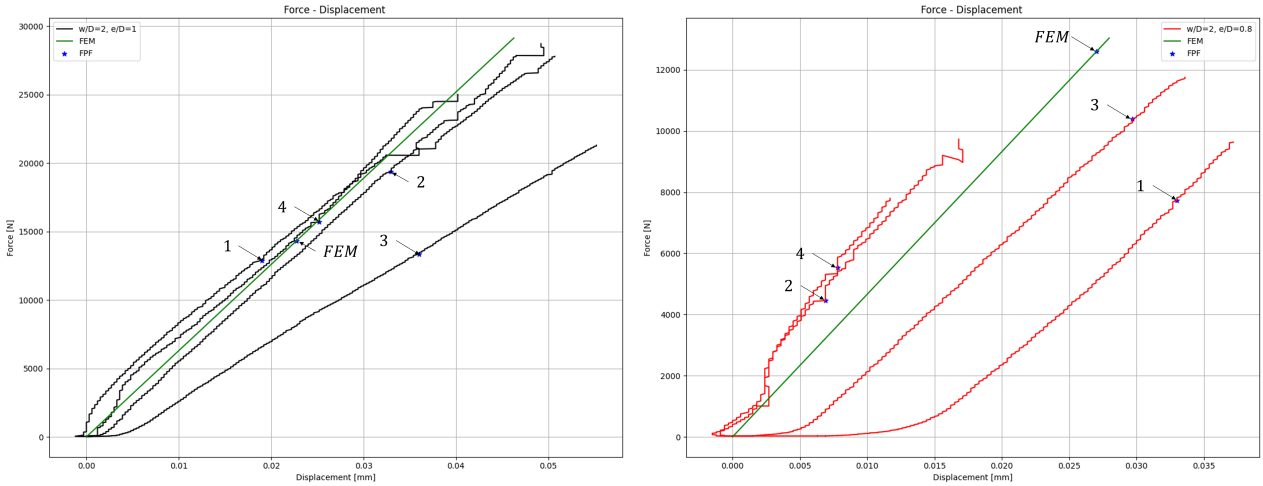

(a) First Ply Failure $w/D = 2$, $e/D = 1$.

(b) First Ply Failure $w/D = 2$, $e/D = 0.8$.

Figure 5.25: Force displacement curves with First Ply Failure.

It can be observed that for the first geometry ($w/D = 2$, $e/D = 1$), the results of the numerical method regarding the FPF, are in close proximity with the results of the experiments. Particularly, the difference between the results of the two methods varies from 7% to 26%. However, for the second geometry ($w/D = 2$, $e/D = 0.8$), the difference regarding the FPF value of the two methods varies from 21% to 127%. The high variation of the second geometry is attributed to the fact that the lug specimens were damaged during the water-jet cutting process. Hence their first ply failure load is low.

Except for the first ply failure, it is very common to seek which ply is going to fail afterward. Abaqus offers progressive damage failure methods, however, there are plenty of variables requested in order to obtain a valid result. Specifically, these damage evolution variables define how the properties of the material are going to degrade. Some of these parameters are the longitudinal and transverse fracture energy in tension and compression. Moreover, linear softening material behavior is assumed.

Due to the fact that these parameters were not known for the specific material utilized in the simulations, a manual approach was implemented in order to detect the next layer that was going to fail. Particularly, after it was ensured that the 90^o layers failed first, the analysis was run again. However, in the new attempt a new material was assigned in the 90^o layer which had a very low stiffness perpendicular to the fiber direction ($E_2 \approx 0$) and a high strength in tension ($Y_t \approx X_t$). This is a rough approach to manually degrade the properties of the 90^o, and at the same time ensure that the failure will happen in another layer (reason for increasing the strength of the 90^o). The results of this approach pointed out that the 45^o layers are the ones that fail next. Given the fact that the strength of a 45^o layer in the loading direction is less compared to the 0^o, this outcome is reasonable.

Finally, the failure of the 90^o in the middle of the laminate, results in an inability of these layers to carry any load. Therefore the capacity of the laminate to carry a higher load slowly decreases. The failure of a layer implies matrix cracking or fiber breakage. These cracks can be the reason for the initiation of delaminations [66]. Therefore, it can be assumed that the failure mode of the laminate could be a combination of failure modes, and one of them would be delamination. This assumption is consistent with the images obtained from the high-speed camera. Specifically, it

was noticed that at the moment of the final failure, a delamination would occur in the middle of the laminate. The moment of failure for the two types of geometries can be observed in Figure 5.26. The load that these images were taken are $F = 28721N$ for geometry 1 (5.26a) and $F = 11757N$ (5.26b) for geometry 2.

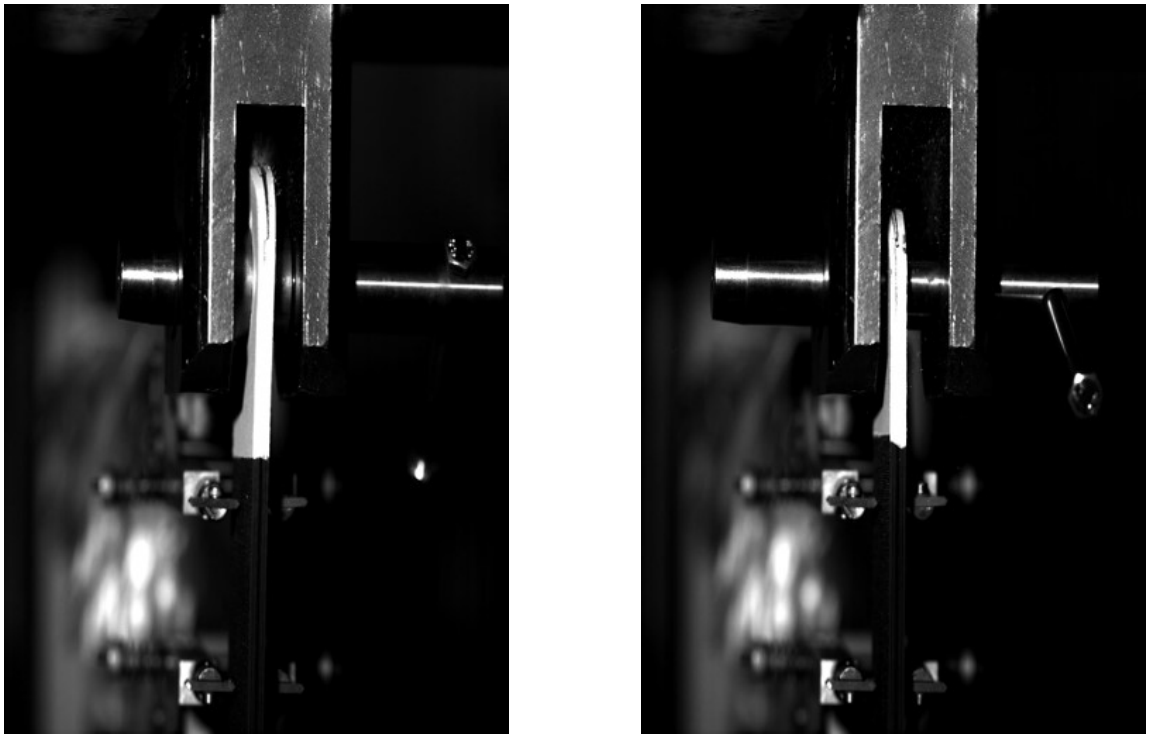

(a) Moment of failure for $w/D = 2$, $e/D = 1$.

(b) Moment of failure $w/D = 2$, $e/D = 0.8$.

Figure 5.26: Images from the high-speed camera at the moment of failure for the two geometries.

The approach described in this chapter verified that the methodology followed for the in-plane modeling of a composite lug in a numerical simulation environment, provides results that can be trusted. This conclusion is derived from the fact that the stress-strain data and the slope of the curves between the experimental and numerical methods are in accordance. Although the results are promising, the validation refers only to the in-plane phenomena that occur in the composite lug. A more detailed FEM model should be developed in order to include the delamination failure mode which seems to be a driving factor in the failure of the specimens.

CHAPTER 6

Failure Mode Prediction

In this chapter, an attempt to predict the in-plane failure mode of the lug will be made. Specifically, with the semi-analytical approach, the failure of the ply will be predicted using the Puck and Hashin failure criteria. The mode predicted with this approach will be compared with the mode predicted from the numerical simulations. Finally, the outcome of these two approaches is going to be compared with the mode of failure noticed in the tensile tests.

6.1 Semi-analytical mode prediction

As it was described in the previous chapters, the approach presented in this thesis can predict with close proximity the stress field around the hole for the given load case. Various points were utilized throughout the geometry and in-plane failure criteria were applied in each point. The discretization of the geometry into points is observed in Figure 6.1.

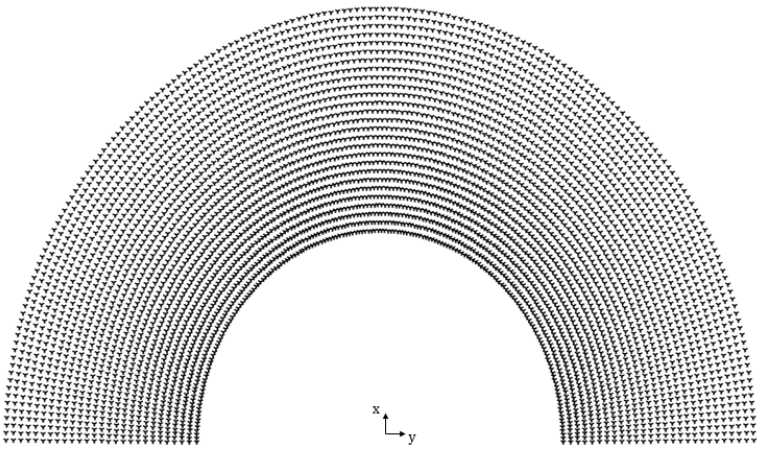

Figure 6.1: Data points for calculating a failure index.

In every point Puck and Hashin failure criteria (justification for selection in section 3.3.1) were applied and a failure index R was estimated (for every point). When the failure index is greater or equal to 1 ($R \geq 1$) failure can be assumed. This methodology assumes that if the failure indexes follow a specific path the mode of failure of the lug could be determined. In particular, if the failure index is increasing perpendicular to the load on the edge of the hole, net-tension failure can be assumed. If the failure follows a path tangent to the edge of the hole and parallel to the load, a shear-out failure can be assumed. An illustration of the results of this approach in a contour plot for the Puck criterion is observed in Figure 6.2. A similar distribution is obtained for the Hashin criterion.

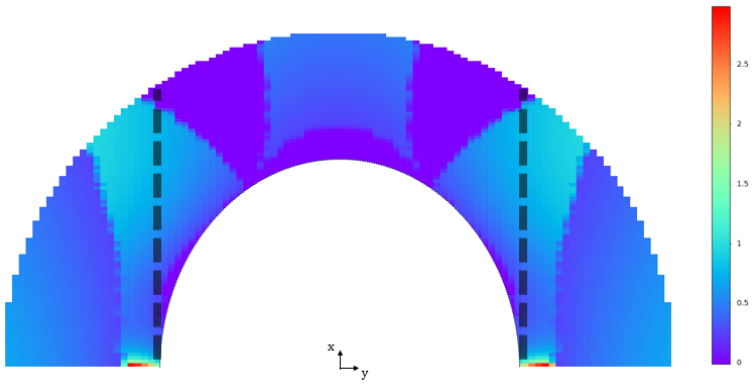

Figure 6.2: Failure index contour plot utilizing the Puck criterion.

The results are obtained for the first layer of the laminate (0^o layer). This choice is substantiated by the fact that the outcome could be easily compared with the results of the tensile tests. As it can be noticed in figure 6.2, the maximum failure index is highest at the edge of the hole. The failure index fluctuates with values of $R \geq 1$, in a path (black dashed line) tangent to the circumference of the hole. The outcome is concurrent with lines formed on the tensile specimens, and it will be discussed in section 6.3. Based on the theory of Chang et al. [33], it could be assumed that the in-plane failure of the lug is a shear-out failure.

6.2 FEM mode prediction

In the numerical simulation model, the Tsai-Hill failure criterion (justification for selection in section 4.3) was utilized. The boundary conditions and information about the model are described thoroughly in section 5.5. The results were obtained for an applied load of approximately $29kN$, which corresponds to the maximum failure load of the specimens in the tensile tests (the same load was applied to the semi-analytical approach). The outcome of the numerical model for the 0^o layer is illustrated in Figure 6.3.

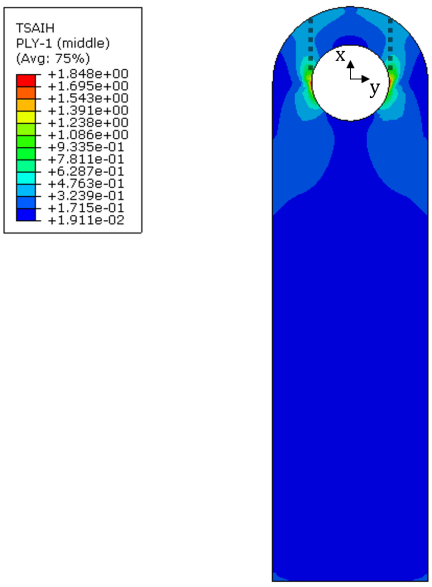

Figure 6.3: Failure index contour plot in the numerical method.

From the results, it can be observed that the failure index follows a path (black dashed line) tangential to the circumference of the hole, parallel to the applied load. It can be assumed that a shear-out failure mode is predicted. The different values of the failure index compared to the semi-analytical approach are attributed to the different failure criteria applied and assumptions made in the semi-analytical approach.

6.3 Experimental failure mode

The failure mode of the lug in the tensile tests can be determined by observing the specimens after failure. It was determined that the specimens failed due to a combination of failure modes. From the high-speed videos, it was noticed that delamination would occur in the moment of failure. In addition, by carefully inspecting the specimens after failure it was concluded that the second failure mode was shear-out mode. These observations are presented in Figure 6.4.

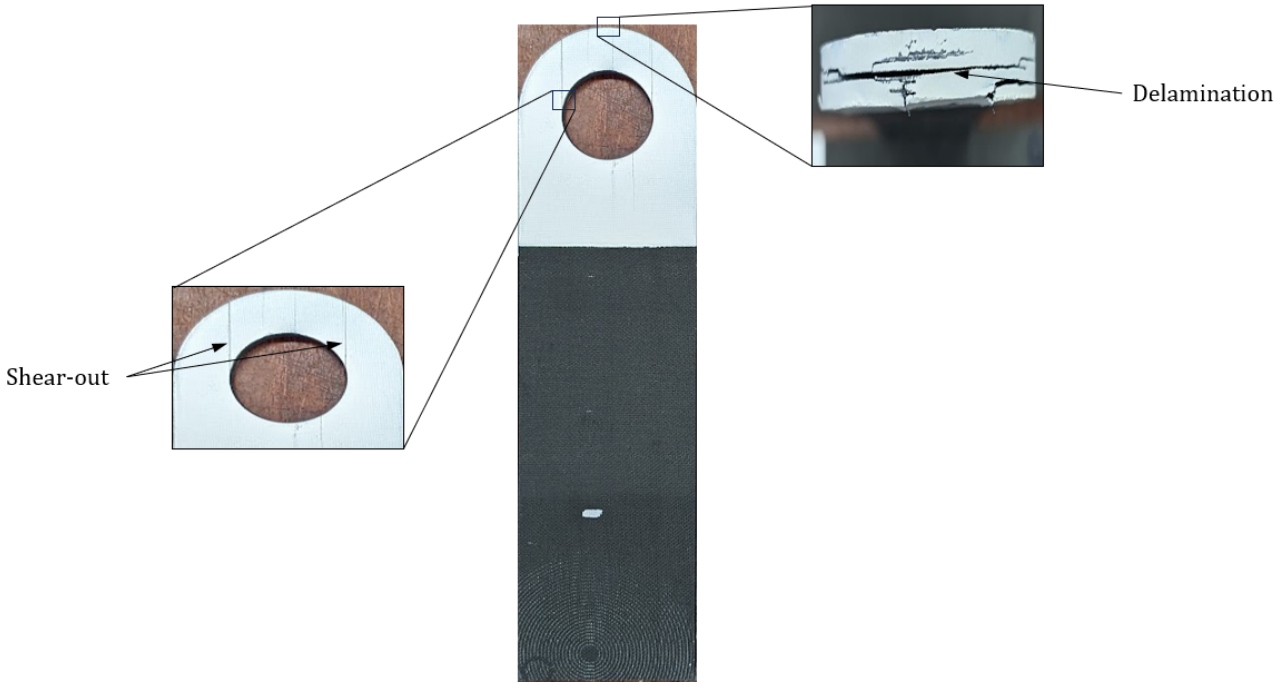

Figure 6.4: Failure modes on a tensile specimen.

It can be concluded that the predicted failure mode of the three methods (semi-analytical, numerical, experimental) are in accordance. Although the results are promising it should be noted that the results of the numerical and semi-analytical are a simple approximation. In particular, in the numerical models, a post-ply failure analysis was not conducted. Additionally, for the semi-analytical approach, a first-ply failure analysis was conducted without taking into account progressive damage failure techniques.

CHAPTER 7

Conclusion

The primary objective of this thesis was to develop a model that could predict analytically the stresses and failure modes of a composite lug subjected to tensile pin loading. This approach required the creation of a semi-analytical methodology, which was later validated with the use of numerical simulations. The scope of the thesis also entails tensile tests which were utilized for evaluating the trustworthiness of the numerical simulation.

In the scope of this research project, an analytical approach was developed which was based on the theory of Lekhnitskii [19] for anisotropic plates, and the theory of elasticity of Timoshenko [3]. This methodology entailed, deriving the stress functions from Lekhnitskii and implementing them into stress expressions for a generic solid body in a polar coordinate system. A key point for determining the stress equation for the specific lug problem is the application of the boundary conditions. The results of this approach were in accordance with the results presented in the literature regarding radial and shear stress, however, a discrepancy was noticed regarding the tangential stress.

For this reason, a semi-analytical approach was developed which implemented a multiplication factor in the stress equation of the tangential stress. The factor was determined by trying to fit the results of the semi-analytical approach with the results of the numerical simulations. A total of 10 laminates with a wide range of stiffness (E_x ranging from $9GPa$ to $131GPa$) were tested for two different geometries and two design curves were created. These design curves were later evaluated by deriving the stress distribution for two new laminates (that were not included in the group of laminates for creating the curves) for every geometry and comparing them with FEM results.

The results of the semi-analytical approach were in accordance with the results of the numerical simulations. In particular, in specific laminates (e.g., laminate 4, 5, 6) with Ex ranging from $50GPa$ to $89GPa$ the results between the two methods had a difference of approximately 2% – 30%. Although this approach works effectively in these laminates, it was noticed that for laminates with very high ($E_x = 131GPa$) and very low ($E_x = 9GPa$) stiffness, the approach was more conservative. Specifically, a maximum difference of 46% was noticed between the results of the two methods (however this difference was noticed in areas where the stresses were not critical).

In addition, it can be concluded that the semi-analytical approach works effectively for laminates that include fibers in the four principal directions (0^o, $\pm 45^o$, 90^o). However, the method does not produce results for quasi-isotropic laminates. This limitation is attributed to the fact that the term $k = \sqrt{E_\theta / E_r}$, is equal to one. This term is in the denominator of some of the integration constants and when set equal to one it leads to terms that tend to infinity. Furthermore, the method also works efficiently for laminates that are a combination of $0^o/\pm 45^o$. It was derived that for these types of laminates, the average maximum deviation between the results was approximately 44%.

For the laminates with a combination of $0^o/90^o$, the method produces results with an average maximum deviation of 46%. The predicted results estimate stresses lower than the ones predicted from the numerical simulation model. However, it was concluded by Wazcak and Cruse [7], that $0^o/90^o$ laminates are not preferred in composite joints under tensile loads. Hence, although the semi-analytical approach underestimates the stresses, this combination is not commonly used in the industry.

For the numerical simulation approach, a 2-D FEM model was developed in the software Abaqus. Plane stress conventional elements were selected in order to estimate the in-plane stress distribution around the hole. The selection is in accordance with the plane-stress assumption of the semi-analytical approach. Moreover, solid elements were not selected due to the fact that 3-D phenomena like delaminations are not an objective of this research topic. The boundary conditions are described by a cosine-distributed shell-edge load in the circumference of the hole and a fixed constraint at the bottom edge of the geometry.

Two geometries were tested, specifically with $w/D = 2, e/D = 1$ and $w/D = 2, e/D = 0.8$. Observing the stress distribution, it can be concluded that the results are in accordance with the research findings of York et al. [32] and Chang et al. [33]. Specifically, the geometry with ratio $e/D = 0.8$ did not influence the stress distribution around the hole, but only the magnitude of the stresses compared with the $e/D = 1$ geometry. However, the change in the edge distance led to a decrease in the failure load of the lug, compared to the geometry with $e/D = 1$.

In the aerospace industry, various types of geometries are utilized. Some of them are very large and wide, which makes the modeling in numerical simulation software tedious. Specifically, due to the large geometry more elements are needed to mesh the model and hence more processing time. In order to optimize the process with regards to minimizing the processing time, a new numerical model was developed. This model utilizes the top part of the lug (which is the most crucial to fail in tensile pin loading) and spring elements. The results of this approach led to a 90% reduction of the mesh size with a maximum difference of 22% in the stress results. In cases where time is the driving design factor, this new approach can be used to get a first estimate of the stress distribution.

The results of the numerical simulations were utilized for validating the semi-analytical approach. However, in order to assess the validity of these results, tensile tests were conducted. Four specimens were manufactured with the autoclave consolidation process for every type of geometry (Design 1: $w/D = 2, e/D = 1$, Design 2: $w/D = 2, e/D = 0.8$). The specimens were tested in tension in a clevis-pin configuration with an extensometer and a high-speed camera. The force-displacement curves obtained by processing the data of the extensometer had the same slope with the curve of the FEM models. Regarding Design 2, the curves have a form of noise, which is attributed to poor attachment between the extensometer and the specimen.

In addition, the stress-strain curves were obtained for two regions on the specimen (net-section, gross-section). The results for the gross-section were in accordance for the two methods. However, for the net-section, a difference in the slope of the curve can be observed in the case of numerical simulation. This slight difference in the slope is attributed to the averaging of the stresses in the net-section region where the stresses have a steep curve due to the stress concentration. Moreover, the slope of the stress-strain curves for the gross-section region represents the stiffness of the laminate in the loading direction (E_x). The slopes for every specimen with the numerical simulation were compared and the results concluded a difference of 1.29% for Design 1 and 1.84% for Design 2.

Finally, the first-ply failure load was obtained for every specimen (obtained by noting down the load on the first cracking noise during the tensile tests and cross-checking it with an abrupt change

in the force-displacement curve) and then compared with the first-ply-failure load obtained in the numerical simulation. For Design 1 the difference between the estimated failure load between the two methods was 6.7%, whereas for Design 2 was 56.7%. The difference for Design 2 is attributed to the fact the specimens were damaged during the water-jet cutting and not on the modeling technique of the FEM models. Hence, the delaminations created during cutting resulted in a lower failure load than expected. Overall, the results of the in-plane numerical simulation models are validated and are considered trustworthy for comparing them with the semi-analytical approach.

Another objective of this thesis topic was to define the in-plane failure mode. As pointed out by the numerical simulation, the 90^o in the middle of the laminate fails first. By observing the path and location of failure while increasing the load, and based on the findings of Chang et al. [33], it was concluded that the failure mode is shear-out. This is concurrent with the failure mode observed on the tensile specimens. It is worth noting that delamination was evident in the specimens, however, since this phenomenon is not studied by this approach only assumptions can be made. Specifically, it can be assumed that matrix cracks created in the 90^o layer, initiated delaminations between the 90^o and adjacent layers. The combination of the two phenomena (shear-out and delamination) led to the final failure of the lug. Overall, the approach of the failure mode is satisfactory, however progressive damage failure techniques should be applied in order to validate the trustworthiness of this approach.

The outcome of this project is a semi-analytical approach that is validated with numerical simulations and experimental data. Given the results of this thesis, it can be concluded that all the objectives were met to a satisfactory degree. The findings of this research topic will have a great impact on the time efficiency in predicting the stress and failure modes from the initial design phase of a project. Although this research project produced acceptable results, there is still room for improvement. Recommendations for enhancing this approach in the future are presented in the next chapter.

CHAPTER 8

Recommendations

In order to improve the findings of this research project some recommendations can be applied to specific areas. In particular, the recommendations are going to be categorized into three main groups namely, the analytical, the numerical, and the experimental part of this thesis.

Analytical

In the analytical approach, an assumption of a curved composite beam was followed. Based on this approach the stress function Φ provided by Lekhnitskii was implemented in the stress equations. This assumption led to a discrepancy in the tangential stresses, and hence it might not be very accurate for the lug problem that is modeled. In order to solve this discrepancy a different approach can be followed. In particular, this problem can be modeled as a plate with finite width and conformal mapping techniques can be applied for predicting the stress distribution around the hole. The conformal mapping technique provides analytical equations for the stresses around openings of various geometries. This approach was not followed due to the mathematical complexity of the method, however, information for implementing this method can be found in the research conducted by Ukadgaonker [67].

The problem modeled in this thesis project is a composite lug loaded under tension. It is very common in the aerospace field that the joints are not only loaded in the axial directions. Following the same methodology, more loads could be implemented in arbitrary directions. However, much consideration should be given to the boundary condition. A methodology on how to calculate the strength of a joint in arbitrary directions is presented in the book of Kassapoglou et al. [45] in Chapter 11.

Based on the last remark, joints are also subjected to out-of-plane loads. For in-plane studies such as the one presented in this thesis, this can be accounted for by using a reduction factor to the material's strength. However, a more detailed approach is needed to calculate the strength of the lug. This approach should focus on studying the out-of-plane loading and its effects on the laminate strength. An analytical equation that can predict the interlaminar stresses could be developed, which can be used as a key element for studying phenomena such as the delamination onset.

The current method is valid for balanced and symmetric laminates. This can be altered by using universal equations for calculating the engineering constants of the laminate. Another improvement of the current method would be to include an optimization algorithm that can predict the optimal laminate for a specific applied load. The process of developing such an algorithm is described thoroughly in section 3.4.2.

Finally, although the cases used for validating the semi-analytical approach compare the stress in the circumference of the hole, the method offers the ability to estimate the stresses throughout the region of the upper part of the lug. A recommendation would be to calculate the exact stress distribution on the failure planes, instead of an average stress proposed in the literature [43]. Moreover, progressive damage failure techniques should be implemented in order to accurately predict the failure mode.

Numerical

As presented in Chapter 4, the numerical simulations are in good accordance with the experimental results. However, further improvements can be implemented in the approach of modeling. Specifically, a 3-D model could be created, which could be meshed with a continuum shell or solid elements. This would provide accuracy in the out-of-plane direction, and delaminations could be studied. This approach is not so simple given the fact that a mesh in the out-of-plane direction significantly affects the accuracy of the model.

In addition, the numerical simulations were used for determining the in-plane first-ply-failure. By implementing data for the fracture energy of the material, and its behavior after failure, post-first-ply-failure could be detected. With this application, the final failure of the laminate could be predicted and compared with the failure load of the experimental results.

From the micro-structural analysis of the manufactured specimens, it was noticed that there was an inconsistency regarding the fiber-volume fraction of the laminate. Specifically, the volume fraction calculated from the specimens was at 52% whereas the volume fraction provided by the material manufacturer was specified at 66%. Although this inconsistency is attributed to the fact that the material was outdated it could be used in the numerical simulations. In particular, the E_1 in the numerical model could be multiplied by the ratio of the volume fractions ($E_{1-new} = 0.52/0.66 \cdot E_{1-old}$). This modification has to be applied in the numerical simulations performed in this research topic, and observe if results are improved with respect to the experimental data.

Experimental

Finally, there are some procedures that can be improved regarding the manufacturing of the specimens and the test configuration. Specifically, as it was mentioned, the material used for manufacturing the specimens was outdated. It is advised for future experimental procedures to use a new (not outdated) material.

Moreover, the volume fraction was estimated based on image processing techniques from data obtained from a microscope. It would be a good approach to determine the volume fraction by burning the specimens, and weighting the fibers. In this way, the image processing approach can be validated, and the fiber volume fraction can be determined with higher accuracy.

Regarding the manufacturing process, it was noticed that opening the lug holes with water-jet cutting resulted in delamination. This phenomenon occurs due to the high speed at which the water impacts the laminate and causes out-of-plane interlaminar stresses to be developed at the point of impact. For future applications, a diamond drill should be used and a trade study should be conducted to find the optimal speed for drilling.

As a final remark, regarding the test set-up, a future recommendation would be to attach strain gauges on the specimens or perform a Digital Image Correlation analysis. In the current study,

only an extensometer was utilized due to the fact that the primary objective was to validate the numerical model.

APPENDIX A

Analytical derivations

A.1 Integration Constants

The integration constants are obtained after solving the system of 6 equations (3.2.30-3.2.36) with 6 unknowns (the integration constants B, C, D, E, F, H). The denominator of the first three constants (B, C, D) has the same value and therefore was named d_1. The same applies to the last three integration constants (E, F, H) with a value of d_2. Specifically, the first denominator is given by,

$$\begin{aligned} d_1 = 2(&a^{1+k}b^{1-k}a^2k^2 - a^{1+k}b^{1-k}b^2k^2 - a^{1-k}b^{1+k}a^2k^2 + a^{1-k}b^{1+k}b^2k^2 \\ &+4a^{1+k}a^{1-k}b^2k - 2a^{1+k}b^{1-k}a^2k - 2a^{1+k}b^{1-k}b^2k - 2a^{1-k}b^{1+k}a^2k - 2a^{1-k}b^{1+k}b^2k \\ &+4b^{1+k}b^{1-k}a^2k + a^{1+k}b^{1-k}a^2 - a^{1+k}b^{1-k}b^2 - a^{1-k}b^{1+k}a^2 + a^{1-k}b^{1+k}b^2)h \end{aligned} \tag{A.1.1}$$

The second denominator is,

$$\begin{aligned} d_2 = 2\cos(\theta)\, h(&\ln(b)\, a^{1+\beta}b^{1-\beta}ab\beta - \ln(b)\, a^{1-\beta}b^{1+\beta}ab\beta \\ &- \ln(a)\, a^{1+\beta}b^{1-\beta}ab\beta + \ln(a)\, a^{1-\beta}b^{1+\beta}ab\beta - 2a^{1+\beta}a^{1-\beta}b^2 \\ &+2a^{1+\beta}b^{1-\beta}ab + 2a^{1-\beta}b^{1+\beta}ab - 2b^{1+\beta}b^{1-\beta}a^2) \end{aligned} \tag{A.1.2}$$

The integration constants are given by the following equations,

$$B = \frac{\begin{aligned}(&-2a^{1+k}b^{1-k}a^2kq + 2a^{1+k}b^{1-k}abkq + 2a^{1-k}b^{1+k}a^2kq - 2a^{1-k}b^{1+k}abkq - 4a^{1+k}a^{1-k}abq \\ &- a^{1+k}b^{1-k}Pbk + 2a^{1+k}b^{1-k}a^2q + 2a^{1+k}b^{1-k}abq + a^{1-k}b^{1+k}Pbk + 2a^{1-k}b^{1+k}a^2q \\ &+ 2a^{1-k}b^{1+k}abq - 4b^{1+k}b^{1-k}a^2q + 2a^{1+k}a^{1-k}Pb - a^{1+k}b^{1-k}Pb - a^{1-k}b^{1+k}Pb)k\end{aligned}}{d_1} \tag{A.1.3}$$

$$C = -\frac{\begin{aligned}&-2a^{1-k}a^3bkq + 4a^{1-k}a^2b^2kq - 2a^{1-k}ab^3kq - 2b^{1-k}a^4kq \\ &+ 4b^{1-k}a^3bkq - 2b^{1-k}a^2b^2kq + a^{1-k}Pa^2bk + a^{1-k}Pb^3k - 2a^{1-k}a^3bq \\ &+ 2a^{1-k}ab^3q - 2b^{1-k}Pa^2bk + 2b^{1-k}a^4q - 2b^{1-k}a^2b^2q + a^{1-k}Pa^2b - a^{1-k}Pb^3\end{aligned}}{d_1} \tag{A.1.4}$$

$$D = -\frac{\begin{aligned}&-2qa^3a^{1+k}bk + 4qa^2a^{1+k}b^2k - 2a^{1+k}ab^3kq - 2qa^4b^{1+k}k + 4qa^3b^{1+k}bk \\ &- 2b^{1+k}a^2b^2kq + a^{1+k}Pa^2bk + a^{1+k}Pb^3k + 2qa^3a^{1+k}b - 2a^{1+k}ab^3q \\ &- 2b^{1+k}Pa^2bk - 2qa^4b^{1+k} + 2b^{1+k}a^2b^2q - a^{1+k}Pa^2b + a^{1+k}Pb^3\end{aligned}}{d_1} \tag{A.1.5}$$

$$E = \frac{(-2aq + P)\, ba\left(b\, a^{1-\beta}\beta\ln(b) - b\, a^{1-\beta}\beta\ln(a) - a^{1-\beta}b + b^{1-\beta}a\right)}{d_2} \tag{A.1.6}$$

$$F = \frac{\begin{array}{c} ab(-2\ln(b)\,a^{1+\beta}ab\beta q + 2\ln(a)\,a^{1+\beta}ab\beta q + \ln(b)\,a^{1+\beta}Pb\beta \\ -\ln(a)\,a^{1+\beta}Pb\beta - 2a^{1+\beta}abq + 2b^{1+\beta}a^2q + a^{1+\beta}Pb - b^{1+\beta}Pa) \end{array}}{d_2} \tag{A.1.7}$$

$$H = \frac{\begin{array}{c} b(-4a^{1+\beta}a^{1-\beta}abq + 2a^{1+\beta}b^{1-\beta}a^2q + 2a^{1-\beta}b^{1+\beta}a^2q \\ +2a^{1+\beta}a^{1-\beta}Pb - a^{1+\beta}b^{1-\beta}Pa - a^{1-\beta}b^{1+\beta}Pa) \end{array}}{d_2} \tag{A.1.8}$$

APPENDIX B

Classical Laminate Theory

B.1 ABD Matrix

In the Classical Laminate Theory, an orthotropic UD layer (lamina) is assumed under a plane-stress condition. The plane stresses in the principal material axis are connected with the strains with reduced stiffness matrix Q,

$$Q_{principal} = \begin{bmatrix} Q_{11} & Q_{12} & 0 \\ Q_{12} & Q_{22} & 0 \\ 0 & 0 & Q_{66} \end{bmatrix} \tag{B.1.1}$$

With,

$$\begin{aligned} Q_{11} &= \frac{E_1}{1 - \nu_{12}\nu_{21}} \\ Q_{22} &= \frac{E_2}{1 - \nu_{12}\nu_{21}} \\ Q_{12} = Q_{21} &= \frac{\nu_{21}E_1}{1 - \nu_{12}\nu_{21}} = \frac{\nu_{12}E_2}{1 - \nu_{12}\nu_{21}} \\ Q_{66} &= G_{12} \end{aligned} \tag{B.1.2}$$

E_1 is Young's Modulus in the fiber direction and E_2 in the transverse direction. G_{12} is the Shear Modulus and ν_{12}, ν_{21} the Poisson's ratio. The Poisson's ratios are related with the expression $\nu_{21} = (E_2/E_1)\nu_{12}$. In order to estimate the reduced stiffness matrix in the laminates (global) coordinate system a transformation is needed. The transformation matrix T is specified as,

$$[T] = \begin{bmatrix} m^2 & n^2 & 2mn \\ n^2 & m^2 & -2mn \\ -mn & mn & m^2 - n^2 \end{bmatrix} \tag{B.1.3}$$

Where,

$$\begin{aligned} m &= \cos\theta \\ n &= \sin\theta \end{aligned}$$

The reduced stiffness matrix in the global coordinate system is,

$$Q_{global} = \begin{bmatrix} Q_{xx} & Q_{xy} & Q_{xs} \\ Q_{yx} & Q_{yy} & Q_{ys} \\ Q_{sx} & Q_{sy} & Q_{ss} \end{bmatrix} = \left[T^{-1}\right] \begin{bmatrix} Q_{11} & Q_{12} & 0 \\ Q_{21} & Q_{22} & 0 \\ 0 & 0 & Q_{66} \end{bmatrix} [T] \tag{B.1.4}$$

After specifying the global reduced stiffness matrix Q, the ABD matrix that contains information for the stiffness of the laminate can be obtained. In particular,

$$\begin{Bmatrix} \mathrm{N_x} \\ \mathrm{N_y} \\ \mathrm{N_s} \\ \mathrm{M_x} \\ \mathrm{M_y} \\ \mathrm{M_s} \end{Bmatrix} = \begin{bmatrix} \mathrm{A_{xx}} & \mathrm{A_{xy}} & \mathrm{A_{xs}} & \mathrm{B_{xx}} & \mathrm{B_{xy}} & \mathrm{B_{xs}} \\ \mathrm{A_{xy}} & \mathrm{A_{yy}} & \mathrm{A_{ys}} & \mathrm{B_{xy}} & \mathrm{B_{yy}} & \mathrm{B_{ys}} \\ \mathrm{A_{xs}} & \mathrm{A_{ys}} & \mathrm{A_{ss}} & \mathrm{B_{xs}} & \mathrm{B_{ys}} & \mathrm{B_{ss}} \\ \mathrm{B_{xx}} & \mathrm{B_{xy}} & \mathrm{B_{xs}} & \mathrm{D_{xx}} & \mathrm{D_{xy}} & \mathrm{D_{xs}} \\ \mathrm{B_{xy}} & \mathrm{B_{yy}} & \mathrm{B_{ys}} & \mathrm{D_{xy}} & \mathrm{D_{yy}} & \mathrm{D_{ys}} \\ \mathrm{B_{xs}} & \mathrm{B_{ys}} & \mathrm{B_{ss}} & \mathrm{D_{xs}} & \mathrm{D_{ys}} & \mathrm{D_{ss}} \end{bmatrix} \begin{Bmatrix} \varepsilon_{xo} \\ \varepsilon_{yo} \\ \gamma_{so} \\ \kappa_x \\ \kappa_y \\ \kappa_s \end{Bmatrix} \rightarrow \begin{Bmatrix} N \\ M \end{Bmatrix} = \begin{bmatrix} A & B \\ B & D \end{bmatrix} \begin{Bmatrix} \varepsilon^o \\ \kappa \end{Bmatrix} \tag{B.1.5}$$

N and M refer to the loads and moments applied to the laminate. As can be observed, the ABD matrix is given in terms of three stiffness matrices, namely A, B, and D. Matrix A contains information about the extensional stiffness, B about the coupling stiffness, and finally D about the bending or flexural stiffness of the laminate. Specifically, these three matrices can be determined by the following expressions,

$$\begin{aligned} A_{ij} &= \sum_{k=1}^{n} Q_{ij}^{k} \left(z_k - z_{k-1}\right) \\ B_{ij} &= \frac{1}{2} \sum_{k=1}^{n} Q_{ij}^{k} \left(z_k^2 - z_{k-1}^2\right) \\ D_{ij} &= \frac{1}{3} \sum_{k=1}^{n} Q_{ij}^{k} \left(z_k^3 - z_{k-1}^3\right) \end{aligned} \tag{B.1.6}$$

z_k, z_{k-1} refer to the distance of the layer from the reference plane and $i, j = x, y, s$.

B.2 Stresses & Strains in the lamina level

From equation B.1.5 the strains in the middle plain of the laminate $(\varepsilon_{xo}, \varepsilon_{yo}, \gamma_{xyo})$ can be estimated. Specifically, the strains of the lamina in a global coordinate system $(\varepsilon_x, \varepsilon_y, \gamma_{xy})$ are related to the strains in the middle of the laminate and the curvatures $(\kappa_x, \kappa_y, \kappa_{xy})$ with the following equation,

$$\begin{aligned} \varepsilon_x &= \varepsilon_{xo} + z\kappa_x \\ \varepsilon_y &= \varepsilon_{yo} + z\kappa_y \\ \gamma_{xy} &= \gamma_{xyo} + z\kappa_{xy} \end{aligned} \tag{B.2.1}$$

In order to estimate the strains in the middle of the laminate, equation B.1.5 has to be solved with respect to the strains. In particular,

$$\begin{Bmatrix} \varepsilon_{xo} \\ \varepsilon_{yo} \\ \gamma_{xyo} \\ \kappa_x \\ \kappa_y \\ \kappa_{xy} \end{Bmatrix} = \begin{bmatrix} \alpha_{11} & \alpha_{12} & \alpha_{16} & \beta_{11} & \beta_{12} & \beta_{16} \\ \alpha_{12} & \alpha_{22} & \alpha_{26} & \beta_{21} & \beta_{22} & \beta_{26} \\ \alpha_{16} & \alpha_{26} & \alpha_{66} & \beta_{61} & \beta_{62} & \beta_{66} \\ \beta_{11} & \beta_{21} & \beta_{61} & \delta_{11} & \delta_{12} & \delta_{16} \\ \beta_{12} & \beta_{22} & \beta_{62} & \delta_{12} & \delta_{22} & \delta_{26} \\ \beta_{16} & \beta_{26} & \beta_{66} & \delta_{16} & \delta_{26} & \delta_{66} \end{bmatrix} \begin{Bmatrix} N_x \\ N_y \\ N_{xy} \\ M_x \\ M_y \\ M_{xy} \end{Bmatrix} \tag{B.2.2}$$

The inverse of the ABD, is later used for calculating the engineering constants of the laminate. By substituting the result of equation B.2.2 to B.2.1, the strains of the lamina in the global coordinate system are estimated. In addition, the stresses of the lamina in the global laminate system can be calculated with,

$$\begin{bmatrix} \sigma_x \\ \sigma_y \\ \tau_s \end{bmatrix} = \begin{bmatrix} Q_{xx} & Q_{xy} & Q_{xs} \\ Q_{yx} & Q_{yy} & Q_{ys} \\ Q_{sx} & Q_{sy} & Q_{ss} \end{bmatrix} \begin{bmatrix} \varepsilon_x \\ \varepsilon_y \\ \gamma_s \end{bmatrix} \tag{B.2.3}$$

Where Q is the global reduced stiffness matrix (B.1.4). Finally, the stresses and strains in the principal system of the layer can be estimated by performing a simple transformation,

$$\begin{bmatrix} \sigma_1 \\ \sigma_2 \\ \tau_{12} \end{bmatrix} = [T] \begin{bmatrix} \sigma_x \\ \sigma_y \\ \tau_s \end{bmatrix} \tag{B.2.4}$$

$$\begin{bmatrix} \epsilon_1 \\ \epsilon_2 \\ \frac{1}{2}\gamma_{12} \end{bmatrix} = [T] \begin{bmatrix} \epsilon_x \\ \epsilon_y \\ \frac{1}{2}\gamma_s \end{bmatrix} \tag{B.2.5}$$

Bibliography

[1] H. A. Whitworth, O. Aluko, and N. A. Tomlinson. “Application of the point stress criterion to the failure of composite pinned joints”. In: *Journal of Engineering Fracture Mechanics* 75 (7 May 2008), pp. 1829–1839. ISSN: 00137944. DOI: 10.1016/j.engfracmech.2006.12.003.

[2] J. Qiu et al. “Novel NDT methods for composite materials in aerospace structures”. In: vol. 52. IOS Press, 2016, pp. 25–33. DOI: 10.3233/JAE-162203.

[3] S. Timoshenko and J. N. Goodier. *Theory of Elasticity*. Second Edition. McGraw-Hill Book Company, Inc., 1951.

[4] F. P. Cozzone, M. A. Melcon, and F. M. Hoblit. “Analysis of Lugs And Shear Pins Made of Aluminum Or Steel Alloys”. In: *Journal of Product Engineering* 21 (5 1950), pp. 113–117.

[5] G. Maddux. *Lug Analysis - Chapter 9*. U.S. Air Force, 1969.

[6] E. F. Bruhn. *Analysis and Design of Flight Vehicle Structures*. Second Edition. Tri-State Offset Company, 1973.

[7] J. Waszczak and T. Cruse. “Failure Mode and Strength Predictions of Anisotropic Bolt Bearing Specimens”. In: *Journal of Composite Materials* 5 (3 Mar. 1971), pp. 421–425. ISSN: 0021-9983. DOI: 10.1177/002199837100500314.

[8] P. P. Camanho and F. L. Matthews. “A Progressive Damage Model for Mechanically Fastened Joints in Composite Laminates”. In: *Journal of Composite Materials* 33 (24 Dec. 1999), pp. 2248–2280. ISSN: 0021-9983. DOI: 10.1177/002199839903302402.

[9] F. K. Chang and K. Y. Chang. “Post-Failure Analysis of Bolted Composite Joints in Tension or Shear-Out Mode Failure”. In: *Journal of Composite Materials* 21 (9 Sept. 1987), pp. 809–833. ISSN: 0021-9983. DOI: 10.1177/002199838702100903.

[10] P. P. Camanho and F. L. Matthews. “Stress analysis and strength prediction of mechanically fastened joints in FRP: a review”. In: *Composites Part A: Applied Science and Manufacturing* 28 (6 Jan. 1997), pp. 529–547. ISSN: 1359835X. DOI: 10.1016/S1359-835X(97)00004-3.

[11] C. Kassapoglou and P. A. Lagace. “An Efficient Method for the Calculation of Interlaminar Stresses in Composite Materials”. In: *Journal of Applied Mechanics* 53 (4 Dec. 1986), pp. 744–750. ISSN: 0021-8936. DOI: 10.1115/1.3171853.

[12] R. B. Pipes and N. J. Pagano. “lnterlaminar Stresses in Composite Laminates Under Uniform Axial Extension”. In: *Mechanics of Composite Materials* (1970), pp. 234–244.

[13] A. K. Noor and W. S. Burton. “Assessment of Shear Deformation Theories for Multilayered Composite Plates”. In: *Applied Mechanics Reviews* 42 (1 Jan. 1989), pp. 1–13. ISSN: 0003-6900. DOI: 10.1115/1.3152418.

[14] W. M. Lucking, S. V. Hoa, and T. S. Sankar. “The Effect of Geometry on Interlaminar Stresses of [0/90]s Composite Laminates with Circular Holes”. In: *Journal of Composite Materials* 18 (2 Mar. 1984), pp. 188–198. ISSN: 0021-9983. DOI: 10.1177/002199838401800207.

[15] J. C. Brewer and P. A. Lagace. “Quadratic Stress Criterion for Initiation of Delamination”. In: *Journal of Composite Materials* 22 (12 Dec. 1988), pp. 1141–1155. ISSN: 0021-9983. DOI: 10.1177/002199838802201205.

[16] F. K. Chang and G. S. Springer. "The Strengths of Fiber Reinforced Composite Bends". In: *Journal of Composite Materials* 20 (1 Jan. 1986), pp. 30–45. ISSN: 0021-9983. DOI: 10.1177/002199838602000103.

[17] J. M. Whitney and R. J. Nuismer. "Stress Fracture Criteria for Laminated Composites Containing Stress Concentrations". In: *Journal of Composite Materials* 8 (3 July 1974), pp. 253–265. ISSN: 0021-9983. DOI: 10.1177/002199837400800303.

[18] J. M. Whitney and R. J. Nuismer. *Uniaxial Failure of Composite Laminates Containing Stress Concentrations*. 1975.

[19] S. G. Lekhnitskii, S. W. Tsai, and T. Cheron. *Anisotropic Plates*. Gordon and Breach Science Publishers, 1968. ISBN: 0677206704; 9780677206707.

[20] T. De Jong. "Stresses Around Pin-Loaded Holes in Elastically Orthotropic or Isotropic Plates". In: *Journal of Composite Materials* 11 (1977), pp. 313–331.

[21] T. De Jong. "On the Calculation of Stresses in Pin-loaded anisotropic plates". TU Delft, Nov. 1987.

[22] K. D. Zhang and C. E. S. Ueng. "Stresses Around a Pin-loaded Hole in Orthotropic Plates". In: *Journal of Composite Materials* 18 (5 Sept. 1984), pp. 432–446. ISSN: 0021-9983. DOI: 10.1177/002199838401800503.

[23] J. Waszczak and T. Cruse. "A synthesis procedure for mechanically fastened joints in advanced composite materials". In: American Institute of Aeronautics and Astronautics (AIAA), Mar. 1973. DOI: 10.2514/6.1973-348.

[24] T. A. Cruse. "Application of the boundary-integral equation method to three-dimensional stress analysis". In: *Computers & Structures* 3 (3 May 1973), pp. 509–527. ISSN: 00457949. DOI: 10.1016/0045-7949(73)90094-1.

[25] S. P. Garbo and J. M. Ogonowski. *Effect of Variances and Manufacturing Tolerances on the Design Strength and Life of Mechanically Fastened Composite Joints*. McDonnell Aircraft Company, Apr. 1981.

[26] V. D. Azzi and S. W. Tsai. "Anisotropic strength of composites". In: *Experimental Mechanics* 5 (9 Sept. 1965), pp. 283–288. ISSN: 0014-4851. DOI: 10.1007/BF02326292.

[27] S. W. Tsai and E. M. Wu. "A General Theory of Strength for Anisotropic Materials". In: *Journal of Composite Materials* 5 (1 Jan. 1971), pp. 58–80. ISSN: 0021-9983. DOI: 10.1177/002199837100500106.

[28] O. Hoffman. "The Brittle Strength of Orthotropic Materials". In: *Journal of Composite Materials* 1 (2 Apr. 1967), pp. 200–206. ISSN: 0021-9983. DOI: 10.1177/002199836700100210.

[29] L. Shuguang. "The Maximum Stress Failure Criterion and the Maximum Strain Failure Criterion: Their Unification and Rationalization". In: *Journal of Composites Science* 4 (4 Oct. 2020), p. 157. ISSN: 2504-477X. DOI: 10.3390/jcs4040157.

[30] C. Echavarría, P. Haller, and A. Salenikovich. "Analytical study of a pin–loaded hole in elastic orthotropic plates". In: *Composite Structures* 79 (1 June 2007), pp. 107–112. ISSN: 02638223. DOI: 10.1016/j.compstruct.2005.11.038.

[31] J. H. Crews, C. S. Hong, and I. S. Raju. *Stress-concentration factors for finite orthotropic laminates with a pin-loaded hole*. NASA Tech. Paper 1862, May 1981, pp. 1–40.

[32] J. L. York, D. W. Wilson, and R. B. Pipes. "Analysis of the Net Tension Failure Mode in Composite Bolted Joints". In: *Journal of Reinforced Plastics and Composites* 1 (2 Apr. 1982), pp. 141–152. ISSN: 0731-6844. DOI: 10.1177/073168448200100205.

[33] F. K. Chang, R. A. Scott, and G. S. Springer. "Strength of Mechanically Fastened Composite Joints". In: *Journal of Composite Materials* 16 (6 Nov. 1982), pp. 470–494. ISSN: 0021-9983. DOI: 10.1177/002199838201600603.

[34] T. S. Ramamurthy. "New studies on the effect of bearing loads in lugs with clearance fit pins". In: *Composite Structures* 11 (2 Jan. 1989), pp. 135–150. ISSN: 02638223. DOI: 10.1016/0263-8223(89)90065-2.

[35] F. L. Matthews, C. M. Wong, and S. Chryssafitis. "Stress distribution around a single bolt in fibre-reinforced plastic". In: *Composites* 13 (3 July 1982), pp. 316–322. ISSN: 00104361. DOI: 10.1016/0010-4361(82)90016-7.

[36] E. Iarve. "Three-dimensional stress analysis in laminated composites with fasteners based on the B-spline approximation". In: *Composites Part A: Applied Science and Manufacturing* 28 (6 Jan. 1997), pp. 559–571. ISSN: 1359835X. DOI: 10.1016/S1359-835X(97)00006-7.

[37] J. Koord et al. "Investigation of exact analytical solutions for composite laminates under pin-bearing loading". In: *Composite Structures* 292 (July 2022), p. 115605. ISSN: 02638223. DOI: 10.1016/j.compstruct.2022.115605.

[38] D. J. Peery and J. J. Azar. *Aircraft Structures*. Second Edition. McGraw-Hill Book Company, 1982. ISBN: 0070491968.

[39] K. Shridhar, B. S. Suresh, and M. M. Kumar. "Fatigue Analysis of Wing-Fuselage Lug section of a Transport Aircraft". In: *Procedia Structural Integrity* 14 (2019), pp. 375–383. ISSN: 24523216. DOI: 10.1016/j.prostr.2019.05.046.

[40] K. Kathiresan, T. M. Hsu, and J. L. Rudd. "Stress and Fracture Analysis of Tapered Attachment Lugs". In: *Fracture Mechanics: Fifteenth Symposium* (1984), pp. 72-72–21. DOI: 10.1520/STP32550S.

[41] T. R. Brussat, K. Kathiresan, and J. L. Rudd. "Damage tolerance assessment of aircraft attachment lugs". In: *Engineering Fracture Mechanics* 23 (6 Jan. 1986), pp. 1067–1084. ISSN: 00137944. DOI: 10.1016/0013-7944(86)90148-7.

[42] M. H. Sumanth and T. Ayyappa. "Comparative analysis of aircraft wing fuselage lug attachment bracket". In: *International Journal For Technological Research In Engineering* 5 (11 July 2018), pp. 2347–4718.

[43] C. Kassapoglou and W. A. Townsend. "Failure prediction of composite lugs under axial loads". In: *AIAA Journal* 41 (11 2003), pp. 2239–2243. ISSN: 00011452. DOI: 10.2514/2.6816.

[44] S. C. Tan. "Laminated Composites Containing an Elliptical Opening. II. Experiment and Model Modification". In: *Journal of Composite Materials* 21 (10 Oct. 1987), pp. 949–968. ISSN: 0021-9983. DOI: 10.1177/002199838702101005.

[45] C. Kassapoglou et al. *Design and Analysis of Composite Structures*. Second Edition. John Wiley & Sons Ltd, 2013. ISBN: 9781118401606.

[46] L. J. Hart-Smith. *Mechanically-Fastened Joints for Advanced Composites — Phenomenological Considerations and Simple Analyses*. Springer US, 1980, pp. 543–574. DOI: 10.1007/978-1-4684-1033-4_32.

[47] W. G. Bickley. "The Distribution of Stress Round a Circular Hole in a Plate". In: *Philosophical Transactions of the Royal Society of London. Series A, Containing Papers of a Mathematical or Physical Character* 227 (1928), pp. 383–415. ISSN: 02643952.

[48] J. M. G. Cantero. "Study of the Unfolding Failure of Curved Composite Laminates". Universidad de Sevilla, 2017.

[49] I. M. Daniel and O. Ishai. *Engineering Mechanics of Composite Materials*. Second Edition. Oxford University Press, 2006. ISBN: 9780195150971.

[50] K. L. Reifsnider et al. "Survey of Failure and Post-Failure Theories of Laminated Fiber-Renforced Composites". In: *Journal of Composites Technology and Research* 8 (4 1986), p. 138. ISSN: 08846804. DOI: 10.1520/CTR10335J.

[51] C. T. Sun, B. J. Quinn, and J. Tao. *Comparative Evaluation of Failure Analysis Methods for Composite Laminates*. School of Aeronautics and Astronautics - Purdue University, May 1996.

[52] D. Zarouchas. *Design & Analysis of Composite Structures I*. TU Delft Lecture Notes. 2021.

[53] S. Pinho et al. *Failure Models and Criteria for FRP Under In-Plane or Three-Dimensional Stress States Including Shear Non-Linearity*. NASA, 2005.

[54] C. Schuecker and H. E. Pettermann. "Fiber Reinforced Laminates: Progressive Damage Modeling Based on Failure Mechanisms". In: *Archives of Computational Methods in Engineering* 15 (2 June 2008), pp. 163–184. ISSN: 1134-3060. DOI: 10.1007/s11831-008-9016-z.

[55] Ü. Esendemir. "An experimental study of mechanically fastened composite joints with clearance". In: *International Journal of Damage Mechanics* 20 (3 Apr. 2011), pp. 464–480. ISSN: 10567895. DOI: 10.1177/1056789510397068.

[56] M. Pakdemirli. "A New Perturbation Approach to Optimal Polynomial Regression". In: *Mathematical and Computational Applications* 21 (1 Mar. 2016), p. 1. ISSN: 2297-8747. DOI: 10.3390/mca21010001.

[57] *ABAQUS/Standard User's Manual, Version 6.14*. Dassault Systèmes Simulia Corp, 2014.

[58] *Hexcel 8552 As4 Unidirectional Prepreg at 190 gsm & 35% RC Qualification Material Property Data Report*. CAM-RP-2010-002. Rev. A. National Insitute for Aviation Research. May 2011.

[59] S. G. Advani. "2.2 Role of Process Models in Composites Manufacturing". In: *Comprehensive Composite Materials II* (Jan. 2018), pp. 24–41. DOI: 10.1016/B978-0-12-803581-8.09898-2.

[60] G. Eckold. "Manufacture". In: *Design and Manufacture of Composite Structures* (1994), pp. 251–304. DOI: 10.1533/9781845698560.251.

[61] F. J. Guild and J. Summerscales. "Microstructural image analysis applied to fibre composite materials: a review". In: *Composites* 24 (5 July 1993), pp. 383–393. ISSN: 00104361. DOI: 10.1016/0010-4361(93)90246-5.

[62] R. C. Gonzalez and R. E. Woods. *Digital Image Processing*. Third Edition. Prentice-Hall, Inc., 2006. ISBN: 013168728X.

[63] M. Bodaghi et al. "Experimental characterization of voids in high fibre volume fraction composites processed by high injection pressure RTM". In: *Composites Part A: Applied Science and Manufacturing* 82 (Mar. 2016), pp. 88–99. ISSN: 1359835X. DOI: 10.1016/j.compositesa.2015.11.042.

[64] MATLAB version R2022a. *Circle detection function*. Natick, Massachusetts: The MathWorks Inc., 2022. URL: https://nl.mathworks.com/help/images/ref/imfindcircles.html.

[65] E. Sevkat, M. Brahimi, and S. Berri. "Bearing Strength of Pin Loaded Woven Composites Manufactured by VARTM and Hand Lay-up Techniques". In: *Journal of Polymers & Polymer Composites* 20 (3 2012).

[66] M. R. Wisnom and S. R. Hallett. "The role of delamination in strength, failure mechanism and hole size effect in open hole tensile tests on quasi-isotropic laminates". In: *Composites Part A: Applied Science and Manufacturing* 40 (4 Apr. 2009), pp. 335–342. ISSN: 1359835X. DOI: 10.1016/j.compositesa.2008.12.013.

[67] V. G. Ukadgaonker and V. Kakhandki. "Stress analysis for an orthotropic plate with an irregular shaped hole for different in-plane loading conditions - Part 1". In: *Composite Structures* 70 (3 Sept. 2005), pp. 255–274. ISSN: 02638223. DOI: 10.1016/j.compstruct.2004.08.032.